Lawrence Berkeley National Laboratory
Recent Work

Title
ANOMALOUS ELECTRON HEATING AND ENERGY BALANCE IN AN ION BEAM GENERATED PLASMA

Permalink
https://escholarship.org/uc/item/7hj651sc

Author
Guethlein, G.

Publication Date
1987-04-01

eScholarship.org Powered by the California Digital Library
University of California

LBL-23239

Lawrence Berkeley Laboratory
UNIVERSITY OF CALIFORNIA

Accelerator & Fusion
Research Division

JUNE 1987

ANOMALOUS ELECTRON HEATING AND ENERGY BALANCE IN AN ION BEAM GENERATED PLASMA

G. Guethlein
(Ph.D. Thesis)

April 1987

TWO-WEEK LOAN COPY

This is a Library Circulating Copy
which may be borrowed for two weeks.

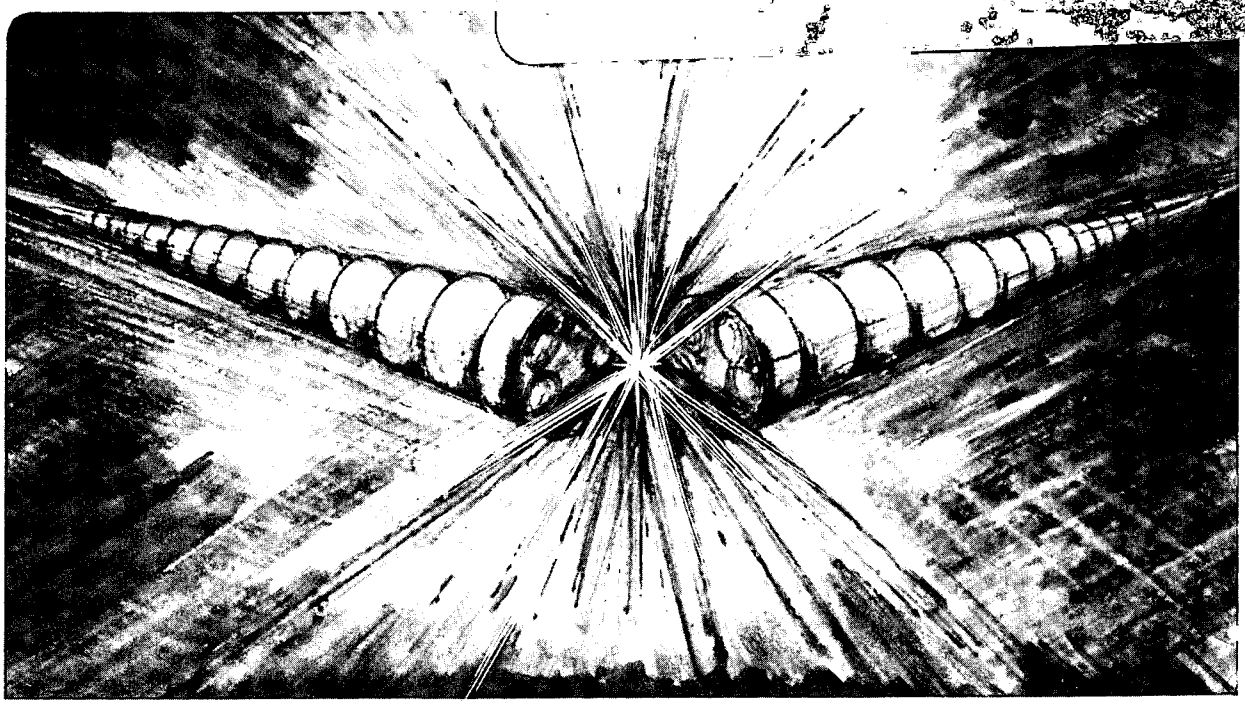

Prepared for the U.S. Department of Energy under Contract DE-AC03-76SF00098

LBL-23239

DISCLAIMER

This document was prepared as an account of work sponsored by the United States Government. While this document is believed to contain correct information, neither the United States Government nor any agency thereof, nor the Regents of the University of California, nor any of their employees, makes any warranty, express or implied, or assumes any legal responsibility for the accuracy, completeness, or usefulness of any information, apparatus, product, or process disclosed, or represents that its use would not infringe privately owned rights. Reference herein to any specific commercial product, process, or service by its trade name, trademark, manufacturer, or otherwise, does not necessarily constitute or imply its endorsement, recommendation, or favoring by the United States Government or any agency thereof, or the Regents of the University of California. The views and opinions of authors expressed herein do not necessarily state or reflect those of the United States Government or any agency thereof or the Regents of the University of California.

LBL-23239

Anomalous Electron Heating and Energy Balance in an Ion Beam Generated Plasma*

Gary Guethlein

Ph.D. Thesis

Lawrence Berkeley Laboratory
University of California
Berkeley, CA 94720

April 1987

* This work was supported by the Director, Office of Energy Research, Office of Fusion Energy, Development & Technology Division of the U.S. Department of Energy under Contract No. DE-AC03-76SF00098.

Anomalous Electron Heating and Energy Balance in an Ion Beam Generated Plasma

Gary Guethlein

Lawrence Berkeley Laboratory
University of California
Berkeley, CA 94720

ABSTRACT

The plasma we describe here is generated by a 15-34 kV ion beam, consisting primarily of protons, passing through an H_2 gas cell neutralizer. Plasma ions (or ion-electron pairs) are produced by electron capture from (or ionization of) gas molecules by beam ions (or ions and atoms). We seek an explanation for the observed anomalous behavior of the electron temperature (T_e): a step-like, nearly two-fold jump in T_e as the beam current approaches that which minimizes beam angular divergence ($\Delta\theta$); insensitivity of T_e to gas pressure; and the linear relation of T_e to beam energy (E_b). This behavior is labeled as anomalous because it is not consistent with the collisional model, which considers only; energy transfer by binary collisions, energy required to expel electrons that are born trapped by the confining plasma potential, and kinetic energy transported to the wall as electrons escape. T_e data agree with the collisional model only so long as the beam is operated in a low current regime where $\Delta\theta$ exceeds ~8-10 deg. For low(er) $\Delta\theta$, our theory predicts electron heating by beam-driven electron plasma oscillations at phase velocity (v_ϕ) ~ 2% below the beam speed (v_b). Wave energy is coupled to the electrons via Landau damping. Strong correlation is observed between the fluctuation signal on a planar probe, violation

of the collisional model, and $\Delta\theta$. The observed fluctuation spectrum agrees with the range of plasma frequencies (as determined from Langmuir probe measurements of the electron density). The empirical dependence $T_e=0.00007E_b$ is ~ 30% below that predicted by equating the linear resonant growth rate with Landau damping. This dependence should hold unless the power balance requires an energy loss per beam ion in excess of $(R/2)^{1/3}$ E_b, where $R=(\omega_b/\omega_e)^2$. We show the possibility of significant gas heating and, hence, increased gas flow. When $\Delta\theta$ exceeds 11 deg., the spread in parallel beam velocities exceeds $v_{slip} = v_b - v_\phi$; all beam ions are no longer resonant; the growth rate is degraded; thus we are able to suppress the instability and observe T_e's that satisfy the collisional power balance. The jump behavior of T_e is then interpreted as a transition between the two regimes of $\Delta\theta$.

Dedication

To my parents, Robert and June Guethlein, for providing a good home and stimulating environment for a young experimentalist, despite the hardships that they encountered.

Table of Contents

Acknowledgments

Almost everyone in the MFE group at LBL has lent invaluable assistance to me, at one point or another. I would like to acknowledge and thank several of them here. Wulf Kunkel patiently advised me and provided a good sounding board for the physics within this work. Bill Cooper was always willing to dig through old files looking for data (outdated to anyone but me) to compare with my theories. I have enjoyed (and learned from) many hours of physics discussions with Al Lietzke. Rick Steele often helped me win an argument with the Modcomp computer that I otherwise would have lost. Norm Abt and Kurt Schoenberg initiated me into the group and to operation of the test stand, and provided a challanging environment for my mind. I have profitted from the intellectual contact with fellow graduate students John Trow, Steve Walther (who participated in the plasma species measurements), Prabhat Ranjan, and Geoffrey Stutzin. Likewise, Steve Savas was always happy to discuss physics with me. Ka-Ngo Leung made the small magnetic ion-mass spectrometer available to me. Operating the experiment was made easier for me by the assistance of Don Williams, Dean Kippenhan, Terry Jackson, Charlie Garret, Alex Gould and Vince Honey. Mark West spent many hours patiently aligning the accelerator electrodes. Steve Wilde, Harlan Hughes, Dennis Calais, and Dave Moussa have helped with fabrication of diagnostic equipment. Lou Biagi and Hans Krapf gave clever suggestions that simplified construction of some diagnostics. My sister Ellen graciously edited this report (some grammatical errors

were added after she was done). C.K.(Ned) Birdsall offered many suggestions that enhanced the clarity of this report. Martha Duenas entered this whole report into the word processor and complained nary a bit at each revision. To all of you, and to any I have ommitted for the sake of brevity, many thanks.

Glossary

a_b	nominal beam radius
a_w	neutralizer radius
A_b	cross sectional area of beam
A_p	cross sectional area of plasma
A_{probe}	probe collection area
β	$m_e m_b/(m_e + m_b)^2$
c_s	ion acoustic wave speed
$\Delta\theta$	angular beam divergence
$\in$	dielectric function
ε	kinetic energy of electron at "birth"
E_n	Characteristic kinetic energy of electron at birth (from ionizaion)
E_b	beam kinetic energy
ΔE_b	change in E_b
F	fraction of H_2^+ ions that have not been converted to H_3^+
ϕ_p	plasma potential with respect to the wall
$\delta\phi_b$	change of ϕ_p across the beam radius
Γ	Energy Loss Rate of electrons on H_2 $\equiv \sum_j \langle\sigma v\rangle E_j$
$\lambda_{ee'}$	mean free path of electrons (e') in a background of thermal electrons (e)
L	system length (100 cm)
$\ell n\lambda$	Coulomb logarithm

μ	reduced mass
m_e	electron mass
m_i	ion mass
m_p	proton mass
η	fraction of electron power lost to ionization $\equiv \langle\sigma v\rangle_{ion} \Phi_{ion} / \Gamma(Te)$
n_b	beam density
n_e	electron density
n_g	gas density
n_i	ion denisty
Π	gas target thickness
ψ	scattering angle
P_{Coul}	Coulomb power input
P_{inel}	inelastic collional power loss by electrons
P_{KE}	power carried to the wall by escaping electrons (as excess kinetic energy)
P_{req}	power required to complete the energy balance
P_{tr}	power consumed by trapped electrons to be expelled from the confining potential well
R	$(\omega_b/\omega_e)^2$
r_i	ion gyroradius
SHAPE	radial average of n_e
SHAPE	radial average of $n_e \cdot n_b$
S_b	perimeter of the beam
S_p	perimeter of the plasma
T_b	$1/2\ m_b(\Delta v_b)^2$

T_e	electron temperature
v_b	nominal beam speed (mass = m_p)
Δv_b	change or spread in v_b
v_e	electron thermal speed
v_i	ion speed
v_ϕ	wave phase velocity
v_s	speed of beam species s
v_{slip}	$v_b - v_\phi$
Vol_p	plasma volume
ω_b	beam plasma frequency
ω_e	electron plasma frequency
ω_o	resonant wave frequency
$X(x,y)$	normalized perpendicular profile of n_e
ξ	$(v_b \cos \theta / v_e)^2$, θ is the angle between $\underset{\sim}{v}_\phi$ and $\underset{\sim}{v}_b$
ζ	ratio of plasma production by thermal electrons to that by the beam

Chapter 1

Introduction

The plasma described in this thesis is produced by passage through a gas-cell-neutralizer of a 15-34 kV, 1-10 Amp, positive ion beam of area 50 cm^2 formed by the Berkeley 10 Amp source and accelerator, see Fig. 1-1. The primary goal of this study is to experimentally explore the processes that determine the electron temperature (T_e) in this plasma. This thesis consists of a body of experimental data (electron temperature and density, neutral gas pressure, beam divergence, and electrostatic fluctuation spectrum) and two theoretical models to describe the data. The first theoretical model is the collisional power balance, which the electron temperature must satisfy when binary interactions dominate the energy exchange. This turns out to be the case when the beam divergence ($\Delta\theta$) is greater than 11 deg. The second theoretical model involves electron heating by beam-driven electron plasma waves, and is applicable whenever $\Delta\theta < 11$ deg. The secondary goal of this thesis is to extend the predictions of this latter model to beam energies ($E_b > 34$ kV) not accessible to us experimentally in this study.

The neutral beam generated by electron capture (charge exchange) and the plasma created are of interest to the magnetic fusion community; the beam because its divergence determines the ultimate ability to deliver power through limited access to a fusion device, and the plasma because of its effects upon the beam, upon beam neutralization efficiency and upon gas transport (gas loading of a

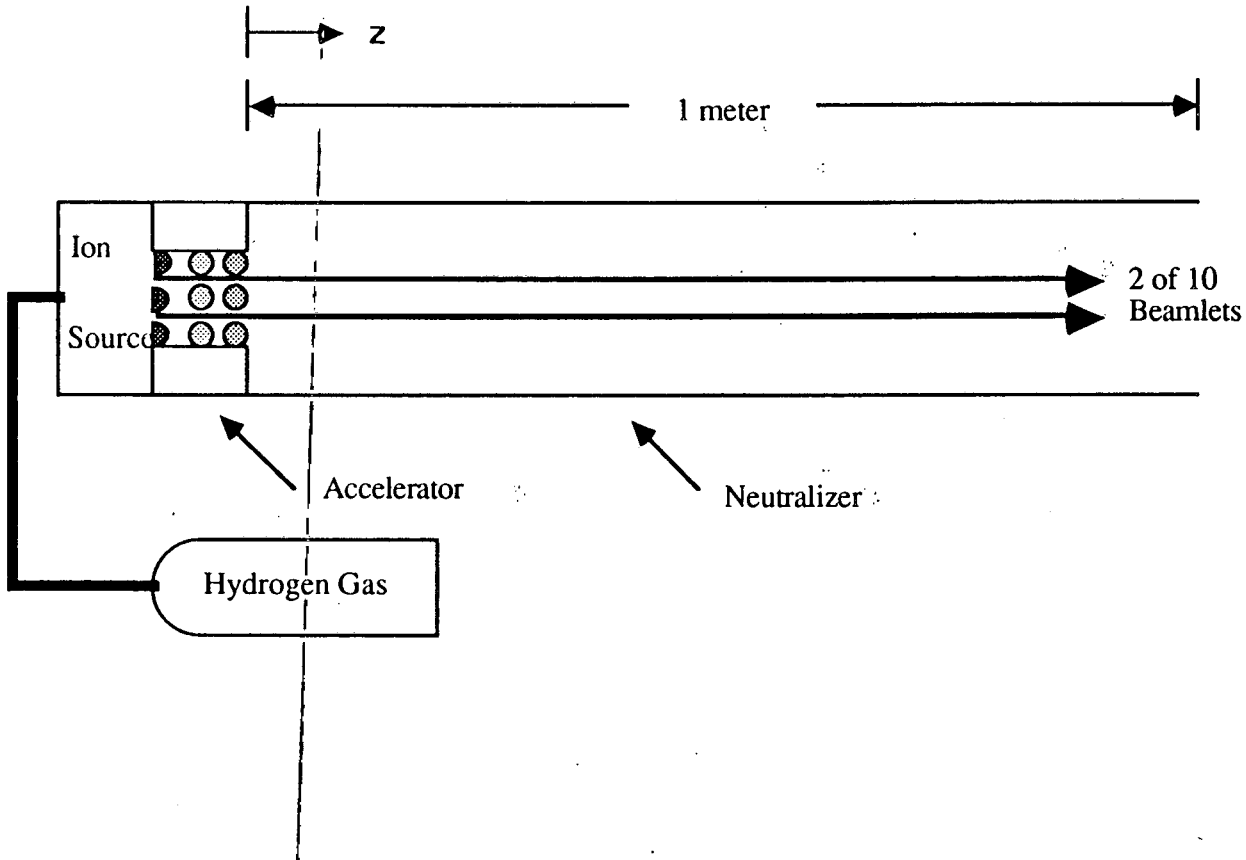

Fig. 1-1 Neutral Beamline Schematic. Accelerator electrode size and spacing not to scale

fusion device). As neutral beams are used to heat and fuel plasma devices requiring greater power, it is likely that the beam power density will need to increase, since designers are not free to provide large access areas through the labyrinth of magnet windings and other hardware associated with magnetic confinement devices. A number of questions come to mind that have not yet been properly addressed. For example: What will be the effect of the neutralizer plasma upon the beam and upon neutralization efficiency at high power densities ? Can we predict this in the general case? What would the best neutralizer dimensions be? Is there any gain to be found in using a longer or shorter neutralizer? Should one employ a neutralizer of cross section significantly larger than the beam?

In the face of these questions concerning the neutralizer is a deceivingly simple neutralizer plasma. The plasma results from beam charge-exchange with, and ionization of, the gas in the neutralizer cell. Positive space charge accumulates as the electrons initially exit the cell more quickly than the ions, owing to their greater mobility. The steady-state solution to the particle balance was the subject of previous work at this facility.[1] However, a completely self-consistent solution was not possible, the electron temperature had to be measured and applied as an empirical variable, just as gas pressure or system dimensions. Not affecting that work, but unexplained, was the observation that the electron temperature would abruptly increase by approximately a factor of two whenever the beam current passed a certain value, independent of gas pressure. This beam current, not coincidentally, is the current (I_{opt}) at which the

accelerator performance (beam divergence) is optimized. This "jump" behavior is displayed in Fig. 1-2, a plot of electron temperature measured as a function of beam current. We also show in Ch. 5 that the final temperature (after the jump) is higher than one would expect given only classical collisions of the beam and electrons. Thus we label this behavior as anomalous. An almost self-consistent model has been offered by Gabovich,[2] which guides us in the collisional power balance of Ch. 2, but that model assumes a particular plasma potential profile (not self-consistent) and neglects inelastic collisions and electron energy lost to the walls. A solution to the Fokker-Planck equation for the electrons has been proposed by Holmes[3] which we disagree with - the electron temperatures derived are considerably higher than those we feel supportable by physical means.

In Ch. 2 we therefore describe the neutralizer plasma and analyze the collisional power balance in some detail. The resulting formidable terms are numerically evaluated in Appendix C, and discussed in Ch. 5, sec. A. We conclude that insufficient power is available collisionally to explain the observed temperature. Also in Ch. 2, we derive scaling relationships for the electron temperature with beam current, beam energy, gas pressure and gas species. The data in Ch. 5, sec. A suggest that these scalings are only valid for a limited range of beam current, failing as the beam current approaches I_{opt}.

We find evidence that the electrons are heated by the presence of a beam-plasma electrostatic instability. Therefore, Ch. 3 pursues theoretically the heating of electrons by a beam-driven instability at

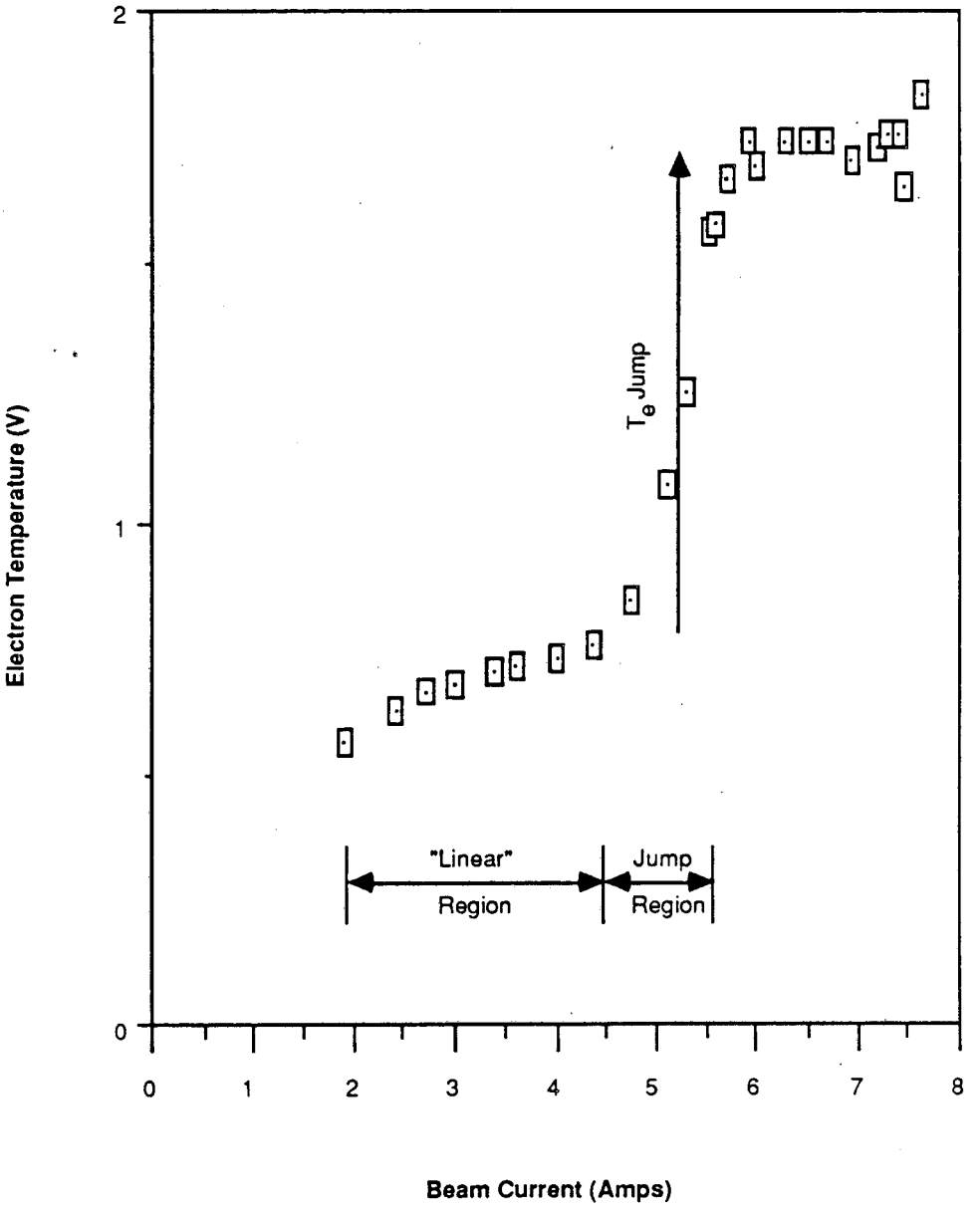

Fig. 1-2 Jump Behavior of Electron Temperature. Beam energy is 25 kV. Gas Pressure is 1.7 mTorr. The electron temperature is measured with a Langmuir probe. The beam current dependence is very nearly linear below 4.5 Amps and then makes a two-fold jump. This behavior is very reproducible. The optimum beam current (minimum beam divergence) is 6.5 Amps.

the electron plasma frequency. We find sufficient coupling of beam energy to the plasma electrons for our system to sustain the electron temperatures observed. A linear relationship between electron temperature and beam energy is a consequence of stabilization by thermal electrons. The power balance is then considered with this anomalous channel of energy extraction from the beam. An approximate self-consistent model is presented, with an attempt at a generalized (though restricted to optimum neutralizer thickness) prediction of the effect of this anomalous power on the neutral gas. Ch. 3 concludes with an algorithm for determining plasma quantities in a general neutralizer.

Ch. 4 is a presentation of the equipment used - the plasma source, accelerator, beam line, and diagnostics from which data are reported in this thesis.

Data - beam properties, plasma density, temperature, and electrostatic fluctuation level and spectrum - are presented and discussed in Ch. 5. Overall, we find good agreement with the combined theories of Ch. 2 and Ch. 3, respectful of the limitations inherent to each. For beam current belows I_{opt}, we find that the measured electron temperatures follow the behavior of the collisional power balance model described in Chapter 2. As the beam current approaches I_{opt}, the plasma fluctation level is observed to increase rapidly, simultaneous with a jump in the electron temperature. The value of the electron temperature after this jump (empirically, $T_e = 0.07\ E_b$ V/kV) is 30% less than one would expect by assuming that electrons resonant with the wave remove wave energy at the same rate

that the wave extracts energy from the beam. Thus we conclude that our experimental data for low divergence ion beams ($\Delta\theta < 10$ deg.) is adequately described by the model based upon beam-driven electron plasma oscillations presented in Chapter 3. The jump behavior observed in the electron temperature as the beam current approaches I_{opt} is the transition between the low and the high beam divergence regimes. A fairly complete understanding exists for the electron temperatures observed in our positive-ion beam neutralizer.

Chapter 2

Collisional Power Balance

A. Particles in the Neutralizer Plasma

The neutralizer for our ion beam is a gas filled pipe of radius 10 cm and length 1 m. It is filled with room temperature hydrogen gas at a pressure of 1-3 mTorr. Dissociation by energetic electrons in the neutralizer as well as those in the ion source produces atomic hydrogen. We presume the atomic hydrogen recombines on the room temperature walls and thus that the gas is predominantly molecular hydrogen (H_2). This is confirmed experimentally by the ratio (1:6) of plasma protons (H^+) to plasma molecular ions (H_2^+, H_3^+) (see Appendix E).

When the beam of cross section 7 x 7 cm enters the neutralizer it consists of three singly ionized components: H^+, H_2^+, and H_3^+, typically in the fractions 60-70%, 15-25%, and 10-15%, respectively. As the beam travels the length of the neutralizer, these components charge exchange with the background gas. The molecular beam ions (as well as neutrals) dissociate. The beam atoms and molecules resulting from charge exchange can also be stripped of an electron in a collision with a gas molecule, and the beam atoms may capture an electron as well, or beam protons may capture two electrons to become H^-. We shall attempt to be complete and include all 14 beam components (see Appendix B) whenever possible, but, for simplicity, shall at times consider the beam to consist solely of protons. In the spatial evolution of the beam, we shall ignore collisions of beam particles

with the neutralizer plasma, due to the low plasma density in gas-filled neutralizers ($n_e/n_g < 0.1\%$; n_e, n_g are the electron and gas densities, respectively). We shall, however, consider beam ion Coulomb collisions with plasma electrons as an energy source for the electrons.

In this gas-filled neutralizer there is also a plasma. The plasma ions and electrons are created by: 1) charge exchange of beam ions; 2) ionization of gas molecules by beam ions, atoms, and molecules; and 3) electron stripping from beam atoms and molecules by gas molecules. These processes (possible events) are depicted in Fig. 2-1. Events 1 and 5 (charge exchange) produce a plasma ion, Event 2 (ionization of an H_2 gas molecule) produces a plasma ion and electron pair, and Event 3 (electron stripping from a beam atom) produces a plasma electron. Event 4 (ionization by a beam proton) produces an ion-electron pair. Events 5 and 6 (the latter is electron capture by a beam neutral) produce plasma ions, while Event 7 (electron stripping from a beam H^-) gives an electron to the plasma. Of course the sequence of events can change, but stripping can only happen to a beam neutral.

In general, ionization by electrons contributes to plasma production. We include this in the next chapter. For our system, though, electronic ionization is negligible, as we shall now demonstrate. The plasma that results is usually of 10-50 times higher density than that of the beam, and with an electron temperature (T_e) < 3 Volts (for our operating range of beam energy - E_b = 15-34 kV). Note that we shall be using a convention where energies are expressed as potentials, with the electronic charge implicit, unless the units

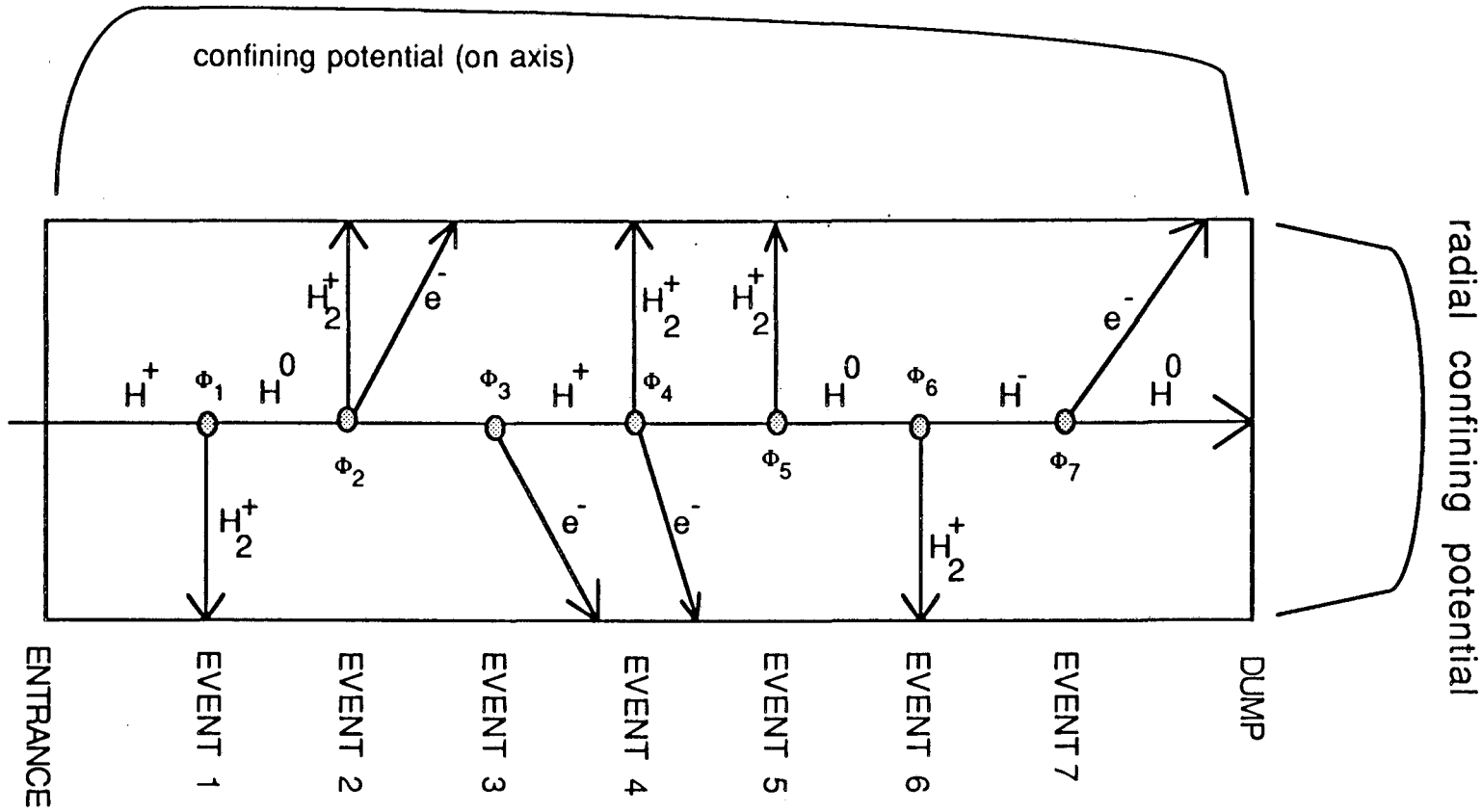

Fig. 2-1 Possible Reactions (Events) Between Beam Particles and Gas Molecules. Φ is the plasma potential where the reaction (ionization is of particular interest) occurs. The axial and radial confining (plasma) potential profiles are sketched at the edge of the drawing.

are explicitly stated otherwise. Additionally, Boltzmann's constant is implicit within T_e so that both thermal energy and temperature are expressed in volts. The ratio of ionization by plasma electrons to that by beam particles is

$$\frac{n_e}{n_b} \cdot \frac{\langle\sigma v\rangle_{ion}}{\sigma_{ion} v_b} < \frac{1}{10\text{-}50} \frac{10^{-10}\,cm^3/sec}{2\cdot 10^{-16}\,cm^2\; 10^6\sqrt{2E_b}\ cm/sec} = (4\text{-}20)\cdot 10^{-4}$$

where $n_e(n_b)$ is the electron (beam) density, v_b is the beam speed, σ_{ion} is the cross section for ionization of H_2 by protons at E_b=25 kV, cm/sec and $\langle\sigma v\rangle_{ion}$ is taken as the average of v times the cross section for ionization of H_2 by the electrons (average over electron speed). We find values for this reaction rate in C. F. Chan's paper.[4] Throughout this thesis we shall use E_b=25 kV as a standard reference, and v_b as the speed of a proton at that energy. The inequality reflects the generous evaluation of $\langle\sigma v\rangle_{ion}$ at T_e=3V. Therefore the production of plasma particles results only from beam interactions with gas molecules. We shall discuss ionization by electrons in the next chapter, when we explore systems where enough power is coupled to the electrons to support ionization.

To maintain quasineutrality, there is a potential that confines the electrons in the absence of a magnetic field, thus slowing them to the same loss rate as the ions. The size of this potential (commonly referred to as the ambipolar potential) is usually $T_e\ \ell n(\sqrt{\frac{m_i}{m_e}})$, where $m_i(m_e)$ is the plasma ion (electron) mass. In our case this will be modified somewhat by a low density, high temperature tail in the elctron distribution function and the presence of a gas density

gradient in the axial direction. This axial nonuniformity allows some axial electron flux and thus the local ion and electron radial fluxes need not be exactly equal. We commonly observe a confining plasma potential of

$$\phi_p = (1\text{-}2) \cdot T_e \ln \left(\sqrt{\frac{m_i}{m_e}}\right) ,$$

which usually lies in the range of 3-20 volts.

In evaluating the last equation we have used T_e = 0.5 - 2.5 V and $m_i = 2m_p$, m_p being the proton mass. The latter is because most of the ions produced are H_2^+ (σ for H_2^+/ σ for $H^+ \simeq 6$).[5] The molecular ion can collide with H_2 molecules and gain an atom to become H_3^+. This is discussed in Appendix E, but will not be considered further here.

Rudd and co-workers[6] have experimentally determined the energy distribution of electrons resulting from proton impact with H_2 gas and fit their data to a semi-empirical model. The resulting distribution function of kinetic energy is

$$f(\varepsilon) = \frac{e^{-\varepsilon/E_n}}{E_n} \qquad (2.1)$$

$$\text{where } E_n = \frac{1}{1.28} \sqrt{\frac{\phi_i E_b}{m_b/m_e}} , \qquad (2.1a)$$

with ϕ_i being the ionization energy of H_2 and m_b/m_e being the beam particle to electron mass ratio (1836). We refer to E_n as the characteristic nascent energy. For our standard E_b = 25 kV and ϕ_i = 15.6 V, E_n = 11.4 V (remember the electron charge is implicit). These electrons begin their free life (no longer bound to a molecule) traveling largely in the beam direction. We refer to these electrons

that have just been freed by a beam-induced ionization event as "nascent electrons". Elastic encounters with H_2 molecules tend to isotropize these nascent electrons with a mean free path of

$$\lambda_{mfp} = \frac{1}{n_g \sigma_{e\ell}(11.4\ V)} \approx \frac{cm^3}{10^{14}\ 10^{-15} cm^2} = 10\ cm\ ,$$

where we have taken $\sigma_{e\ell} \sim 10^{-15} cm^2$.[7] As $\lambda_{mfp} << L$, the neutralizer length (100 cm), we conclude that the nascent electrons are scattered away from their initial forward direction before they escape. This of course allows them to be lost on a wall nearer their point of origin.

The coolest of these electrons (those with energy $< \phi_p$) will be trapped to preserve quasineutrality. These cool down further by inelastic collisions with H_2 molecules and thermalize by electron-electron collisions to a temperature of 0.5-2.5 volts, depending on beam current, beam energy, and, to some extent, gas pressure. The mean free path for electron-electron Coulomb collisions is[8]

$$\lambda_{ee} = \frac{4.5 \cdot 10^{13}\ T_e^2\ cm}{n_e\ \ell n\ \lambda}\ ,$$

where $\ell n\ \lambda$ is the Coulomb logarithm. For our plasma $T_e \sim 2V$, $n_e \sim 5 \cdot 10^{10}/cm^3$, and $\ell n\ \lambda = 10$, so $\lambda_{ee} \simeq 360$ cm. Though this is longer than any of our neutralizer dimensions, these cool electrons are reflected by the potential near the walls, bouncing around until they acquire enough energy to escape the potential well. Noting that the frequency of Coulomb collisions varies as the inverse cube of the relative particle velocities, we conclude that the trapped electrons

make many more thermalizing collisions among themselves than collisions with faster moving particles (those that might give them enough energy to escape). Therefore, we believe the trapped electrons to be thermalized.

Can the fast, nascent electrons give up their energy to the cooler, trapped electrons? For a test particle (electron) with energy E_{test} = 10 volts in a field of 2 volt electrons, the mean free path is[9]

$$\lambda_{ee'} = \frac{10^8 \sqrt{2T_e}\,(E_{test})^{3/2}}{8\cdot 10^{-6}\, n_e \ell n\, \lambda} \qquad (2.2a)$$

$$= \frac{10^4}{8}\,\frac{\sqrt{4}}{5\cdot 10^{10}}\,\frac{(10)^{3/2}}{10} = 1600 \text{ cm}\,, \qquad (2.2b)$$

where we have used $n_e = 5\cdot 10^{10}/\text{cm}^3$, T_e = 2 volts, and $\ell n\, \lambda$ = 10. As this is very much longer than any neutralizer dimension and these electrons are not reflected by the potential, we conclude that the faster nascent electrons (those with kinetic energy, ε, greater than ϕ_p) escape after a few isotropizing elastic collisions with H_2 molecules, but not imparting any energy to the trapped electrons. Thus we see two components of electrons; cold, trapped thermalized electrons and the "hot" nascent electrons, just passing through the plasma on their way to the nearest wall. The latter typically have a density that is a few percent of the density of the former.

B. Collisional Power Balance

In this section we shall derive a formalism for the balance of power in the neutralizer. The collisional distinction is intended to

indicate a neglect of collective effects in the plasma - those will be considered in the next chapter. We shall make no attempt here to formulate a self-consistent model. Such a model would be difficult (not impossible), but, as we shall see in Discussion and Results I, not very useful. Instead, assuming measured quantities for n_e, T_e, and n_g, we shall evaluate (numerically evaluated in Chapter 5, section A) the power consumed by the plasma and compare that to the power available through Coulomb collisions of beam ions with the plasma electrons. If our data does not show these two powers to be equal, then the collisional power balance has been violated. We begin by evaluating the three terms of power consumption - the power expended by moving particles through the potential well, inelastic electron collisions with H_2 molecules, and kinetic energy that particles take with them to the wall (the latter bears no relation to the first term).

1. Energy Exchange with the Potential Well

The exchange of energy with the potential well was first properly accounted for by Gabovich.[2] In comparison with that work, we take advantage of a more recent experimental determination of $f(\varepsilon)$, Eq. 2.1, and also add the effect of electrons stripped from neutral beam atoms (or molecules). In this collisional model, the plasma is presumed to be static.

Consider Fig. 2-1. A beam ion entering the neutralizer plasma from the left "climbs" the static plasma sheath at the neutralizer entrance. By Event 1 (charge exchange), the beam ion has done an

amount of work ϕ_1 (ϕ_1 is measured relative to the wall) on the potential well. Departing from Event 1 are two particles. The neutral beam particle does no work on the well, but the ion resulting from this charge exchange is pushed out of the well and returned to the wall (where $\phi = 0$). The well does an amount of work ϕ_1 on this ion, thereby returning the energy already expended by the initial beam ion.

Two oppositely charged particles leave Event 2 (ionization) and eventually find their way to ϕ=0 at the wall. Since one of each sign charge originates at ϕ_2, no net work is done on/by the potential. However, not all electrons are born with equal kinetic energy. Some are born with too little kinetic energy (ε) to overcome the confining potential. These trapped electrons require an energy acquisition of $\phi_p - \varepsilon$ before they can escape to the wall. We are describing a steady state - so electrons must leave at their creation rate. Those electrons born with $\varepsilon > \phi_p$ escape freely. From Eq. 2.2b we concluded that these free electrons were incapable of helping the trapped electrons escape. The power required to remove the trapped electrons from the well represents a power drain to the system,

$$P_{tr} = \sum_s \int_0^L \int_0^{A_b} \int_0^{\phi_{p(x,y,z)}} f_s(\varepsilon)(\phi_p(x,y,z)-\varepsilon)d\varepsilon \; n_s \sigma_s^e \; v_s n_g dA \; dz \; , \qquad (2.3)$$

which must be provided by an outside source (the beam). Here f_s is the distribution of nascent energies of electrons produced by collision of beam species s, of density n_s with H_2 gas of density n_g; v_s is the speed of these beam particles; and σ_s^e is the cross section for electron production. Both n_s and n_g are functions of position.

The upper limit of integration for $\int dA$ ($dA = dxdy$) is a reminder that $n_s = o$ outside the beam (of area A_b). Particular attention should be paid to the evolution of n_s during the z integration. This issue is addressed numerically in Appendix C.

Two charged particles leave Event 3 (stripping of an electron from a beam atom). The same arguments regarding work done for Event 2 apply here, with the modification that the positive charge exits the well in one of two ways; as a beam ion or as the charge exchange ion produced at Event 5. In either case a positive charge returns to $\phi=0$, having originated at ϕ_3. The work of this (these) event(s) done on/by the potential well is already included in Eq. 2.3 when s represents a neutral beam species and σ_s^e includes the stripping cross section.

Three charged particles leave Event 4 (ionization by a beam proton). The beam ion has already been accounted for. The plasma ion-electron pair created contributes to Eq. 2.3 in exactly the same manner as the pair resulting from Event 2.

The pair of events 6 (electron capture) and 7 (stripping an electron from beam H^-) contribute to Eq. 2.3 in exactly the same way, with the exception that the negative charge can be carried out of the well by either a beam H^- (no Event 7 before the end of the neutralizer) or by an electron (Event 7).

2. Inelastic Collisions

Hydrogen gas provides an effective cooling mechanism for electrons of temperature > 1 volt. This is an additional power drain to the system. We include vibrational excitation of the molecule (energy

level is 0.5 volt), molecular dissociation, electronic excitation, and ionization. We define an energy loss rate per molecule as

$$\Gamma(T_e) \equiv \sum_{\ell} \langle \sigma_\ell v \rangle E_\ell \quad , \tag{2.4}$$

where the summation over ℓ includes the modes just discussed, and E_ℓ is the energy the electron loses in the interaction that proceeds at a rate $n_g \cdot \langle \sigma_\ell v \rangle$ (the brackets indicate an average over the electron distribution). $\Gamma(T_e)$, calculated from C. F. Chan's tables,[4] is shown in Fig. 2-2 and tabulated in Table 2-1. The total power lost by electrons to inelastic collisions is

$$P_{inel} = \Gamma(T_e) \int_{Vol_p} n_e(x,y,z)\, n_g(z)\, dxdydz, \tag{2.5}$$

where the integral is taken over the plasma volume, Vol_p. We are assuming all the gas is H_2, as discussed previously, and so have not included any atomic excitation in Eq. 2.4.

3. Kinetic Energy Carried Out of the Potential Well

The kinetic energy each ion carries out of the well has already been accounted for in Eq. 2.3. Here we concern ourselves only with the electrons. It has been shown that an electron "boiled" out of a potential well has some small fraction of T_e energy associated with its motion perpendicular to the edge of the well.[10] In addition, it will carry 1/2 T_e energy in either of the two directions parallel to the wall. For simplicity, we shall take T_e as the kinetic energy of each electron as it exits the well.

The power carried to the wall by the electrons is then

$P_{KE} = T_e \cdot$ total electron production rate of trapped electrons

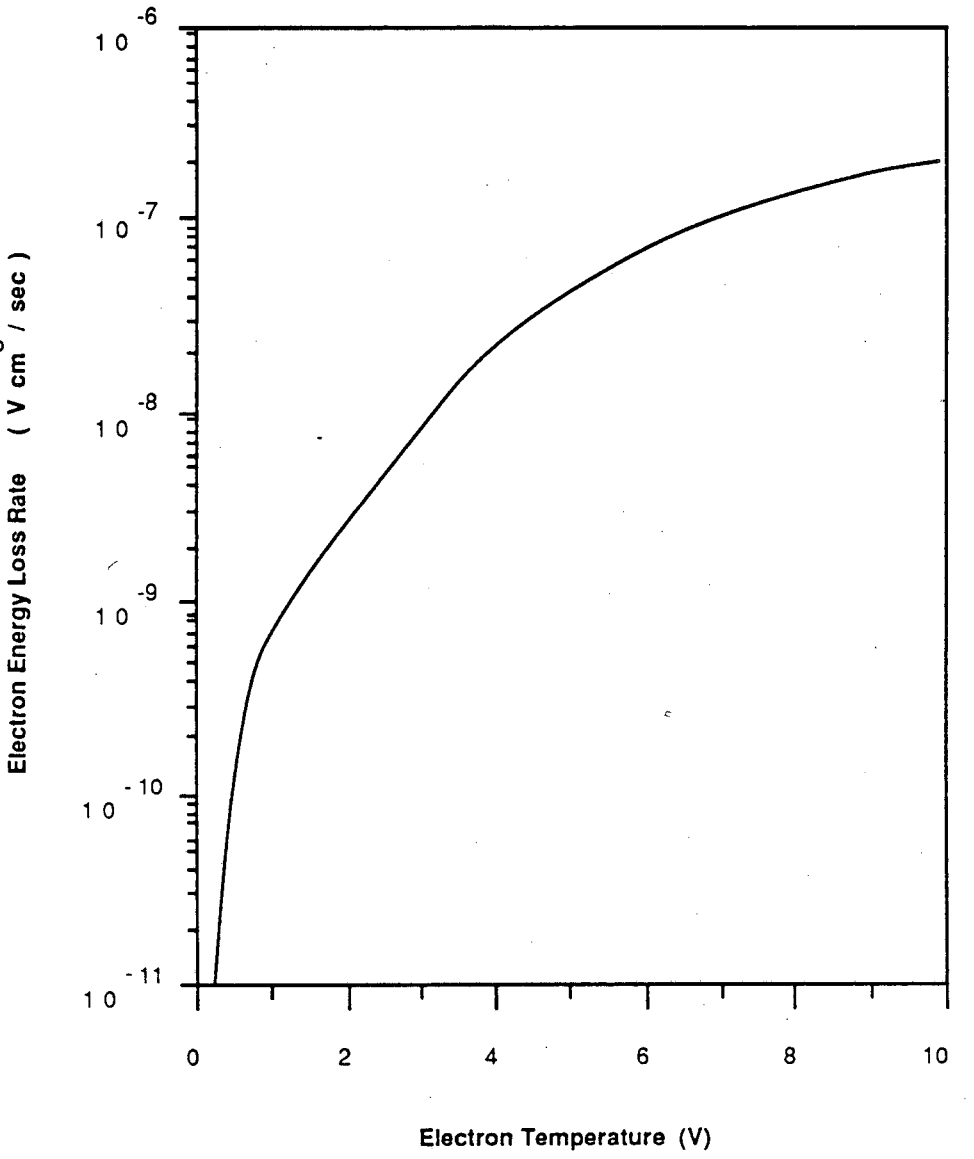

Fig. 2-2 Electron Energy Loss Rate Per Molecule. Calculated from Eq. 2.4 using the rate coefficients tabulated in Ref. 4 and smoothed.

Table 2-1

T_e (V)	Electron Energy Loss Rate (10^{-9} Vcm^3/sec)
0	0.01
0.25	0.01
0.5	0.18
0.75	0.47
1	0.75
1.25	1.06
1.5	1.37
1.75	1.83
2	2.46
2.25	3.5
2.5	4.7
2.75	6.8
3	8.5
3.25	12.5
3.5	15.8
3.75	19.8
4	24.5
4.25	29.6
4.5	34.9
4.75	40.9
5	47
5.25	53.5
5.5	60.4
5.75	68.8
6	78
6.25	85.2
6.5	93.7
6.75	103
7	111
7.25	120
7.5	128
7.75	138
8	148
8.25	157
8.5	167
8.75	176
9	185
9.25	194
9.5	205
9.75	212
10	223

$$= T_e \int_0^L \int_{A_b} \sum_s \int_0^{\Phi_p} f_s(\epsilon)d\epsilon \; n_s \sigma_s^e v_s n_g \; dxdydz \qquad (2.6)$$

where again dxdy is to be taken over the beam area, and σ_s^e is the cross section for electron production by beam species s.

4. Coulomb Heating

The energy source of all the above energy drains from the electrons is presumed to be beam-ion Coulomb collisions with the electrons. The spatial rate of energy transfor from beam species s to the electrons is related to the temporal rate by

$$\frac{dE_s}{dz} = \frac{1}{v_s} \frac{dE_s}{dt} ,$$

where v_s is the speed of beam species s. With

$$x^{s/e} = \frac{m_e}{m_s} \frac{E_s}{T_e} \quad \text{and}$$

$$\Psi(u) = \frac{2}{\sqrt{\pi}} \int_0^u \sqrt{t}\, e^{-t} dt ,$$

$$\frac{dE_s}{dz} = \frac{4\pi q_s^2 e^4 n_e \ell n\lambda}{m_e v_s^2} \left[\Psi(x^{s/e}) - \frac{m_e}{m_s} \Psi'(x^{s/e})\right] , \qquad (2.7)$$

where q_s is the charge state ($\pm$ 1, or 0).[9] For even the slowest of our beam particles (those that begin as H_3^+), $x^{s/e} > 2$ (for our standard parameters of E_b = 25 kV and T_e = 1.8 V), so that the term in parentheses is very nearly unity. Then

$$\frac{dE_s}{dz} \simeq \frac{4\pi n_e q_s^2 e^4 \ell n\lambda}{m_e v_s^2} . \qquad (2.8)$$

Since the only species dependence is through $v_s^2 = 2E_s/m_s$ and q_s^2, all charged beam particles that originate from, say, H_2^+ have the same dE_s/dz. This is because when H_2^+(or H_2^o) dissociates, each of the two products receives half of the original energy; thus E_s/m_s is "conserved" for our example, when $m = 2m_p$ becomes 2 masses of $m = m_p$.

We define Coulomb power to be the volume integrated power transferred to the electrons by Coulomb collisions with beam ions. The Coulomb power heating the electrons is thus the flux of beam particles ($n_s v_s$) times dE_s/dz, integrated over volume and summed over s,

$$P_{Coul} = \frac{4\pi e^4 \ell n\lambda}{m_e} \sum_s q_s^2 \int_{A_b} \int_0^L \frac{n_e(x,y,z) n_s(x,y,z) v_s}{v_s^2} \, dxdydz \qquad (2.9)$$

We leave v_s in the numerator, since the particle flux $n_s v_s$ is a convenient variable ($n_s v_s = \frac{I_s}{A_b}$: I_s is the particle current of beam species s, with units of number/sec).

5. Balance

The balance of power then would be expressed as

$$P_{Coul} = P_{Tr} + P_{inel} + P_{KE} \, . \qquad (2.10)$$

We shall find in Chapter 5, Section A that P_{Coul} is too small to account for all the power drains. We define the anomalous power required as

$$P_{anom} = P_{Tr} + P_{inel} + P_{KE} - P_{Coul} \, . \qquad (2.11)$$

We shall find that this is supplied by I_1, the proton beam particle current. So each proton loses

$$\Delta E_{anom} = P_{anom}/I_1 \ . \qquad (2.12)$$

C. Parametric Dependence of the Collisional Power Balance

Let us examine the dependence of the four power terms upon beam current, gas density, and accelerating potential (I_b, n_g, E_b).

1. Energy Exchange with the Potential Well

Consider Eq. 2.3. It is linear in n_g and linear in I_b through $\Sigma n_s v_s$. The variation of P_{tr} with E_b is somewhat obscure. Examine the integral over nascent energy,

$$I_\varepsilon \equiv \int_0^{\phi_p} f_s(\varepsilon)(\phi_p - \varepsilon)d\varepsilon \ . \qquad (2.13)$$

If $E_n \leq \phi_p$, as is generally the case (for our standard parameters, we have E_n = 11.4 V [see discussion below Eq. 2.1a] and measure $\phi_p \simeq$ 15V),

$$I_\varepsilon \simeq \phi_p - E_n \qquad (2.13a)$$

Recall that $E_n \propto \sqrt{E_b \phi_i}$ and assume $\phi_p \propto T_e$; then

$$P_{Tr} = g_1(T_e - g_2 \sqrt{E_b\ \phi_i})\ I_b n_g \sigma^e(E_b), \qquad (2.14)$$

where g_1 and g_2 are constants of proportionality and σ^e is the cross section for production of electrons by the beam.

2. Inelastic Collisional Losses

The only dependence of Eq. 2.5 upon E_b is indirectly through n_e by way of T_e (affects ion loss rate) and σ for ion production. We then conclude P_{inel} varies linearly with I_b (through production

$n_e \alpha I_b n_g / \sqrt{T_e}$) and quadratically with n_g (one n_g is already in the integrand - a second n_g comes from $n_e \alpha I_b n_g / \sqrt{T_e}$). Then

$$P_{inel} = g_3 \frac{I_b n_g^2}{\sqrt{T_e}} \Gamma(T_e) \sigma^{ion}(E_b) \quad , \tag{2.15}$$

where g_3 is a constant of proportionality, and $\sigma^{ion}(E_b)$ is the cross section for production of ions by the beam.

3. Kinetic Energy Transported Out of the Potential Well

Eq. 2.6 varies linearly with I_b through $n_s v_s$, slightly with E_b by way of σ_s^e, and linearly with n_g. Thus, if $E_n < \phi_p$,

$$P_{KE} = g_4 n_g I_b T_e \sigma^e(E_b) \quad , \tag{2.16}$$

where g_4 is a constant of proportionality.

4. Coulomb Heating

Eq. 2.9 varies as $n_e I_b / v_s^2$. We note $n_e \alpha I_b n_g \sigma^{ion} / T_e$, and find

$$P_{Coul} = g_5 \frac{I_b^2 n_g \sigma^{ion}(E_b)}{\sqrt{T_e} E_b} \quad , \tag{2.17}$$

where g_5 is a constant of proportionality.

5. Resultant Parametric Dependence of T_e

Combining eq.'s 2.14-2.17 into Eq. 2.10 gives

$$\frac{g_5 I_b^2 n_g \sigma^{ion}(E_b)}{E_b \sqrt{T_e}} = g_1 (T_e - g_2 \sqrt{E_b \phi_i}) I_b n_g \sigma^e(E_b) + g_3 \frac{I_b n_g^2 \sigma^{ion}(E_b)}{\sqrt{T_e}} \Gamma(T_e)$$

$$+ g_4 n_g \sigma^e(E_b) I_b T_e \quad .$$

Dividing by $(g_1 + g_4)I_b n_g \sigma^e$, rearranging, and defining new proportionality constants yields

$$T_e = \frac{g_6 I_b}{E_b \sqrt{T_e}} \frac{\sigma^{ion}(E_b)}{\sigma^e(E_b)} + g_7 \sqrt{E_b \Phi_i} - \frac{g_8 n_g}{\sqrt{T_e}} \frac{\sigma^{ion}(E_b)}{\sigma^e(E_b)} \Gamma(T_e) \qquad (2.18)$$

Consider first the variation with I_b while holding E_b and n_g fixed. In the limit where the last term in Eg. 2.18 is small (valid for $T_e < 1$ eV [see Fig. 2-2]), we have

$$T_e^{3/2} - g_9 \sqrt{T_e} = g_{10} I_b .$$

We have set $g_9 = g_7 \sqrt{E_b}$ and $g_{10} = g_6/E_b$. Restricting ourselves to small changes in T_e, we treat the $\sqrt{T_e}$ term as a constant, and find

$$T_e = g_{11}(I_b + g_{12})^{2/3} , \qquad (2.19)$$

where

$$g_{11} = (g_{10})^{2/3} \qquad (2.19a)$$

Consider now the variation of Eq. 2.18 with E_b, while holding I_b and n_g fixed. In Fig. 2-3 we plot $\sigma^{ion}(E_b)/\sigma^e(E_b)$ for H^+ on an H_2 target. While the beam is not entirely H^+, we take Fig. 2-3 to be representative of the ratio of ion to electron production which, as Fig. 2-3 shows, decreases with energy. The first term on the RHS (the Coulomb term) is decreasing with E_b. Then an upper bound for the variation of T_e with E_b would be that found by taking the Coulomb term as a constant,

$$T_e + \frac{g_{13}}{\sqrt{T_e}} \frac{\sigma^{ion}(E_b)}{\sigma^e(E_b)} \Gamma(T_e) = g_7 \sqrt{E_b} + g_{14} , \qquad (2.20)$$

where we have defined new proportionality constants g_{13} and g_{14}.

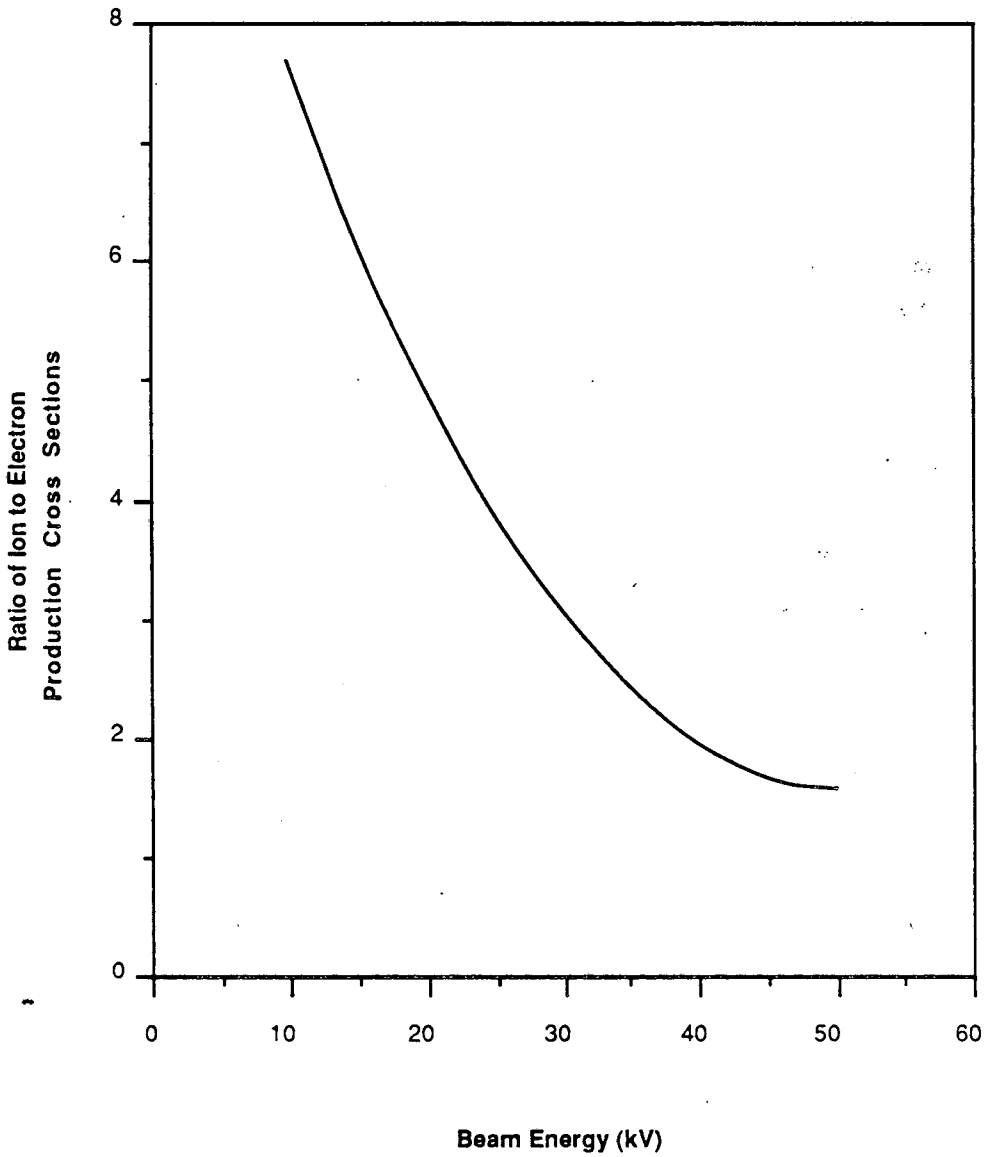

Fig. 2-3 Beam Energy Dependence of the Ratio of Cross Sections for the Production of Ions to that for Electrons. The ratio is greater than unity due to ion production by beam charge exchange (electron capture).

Instead of holding I_b constant, we could require I_b to follow the Child-Langmuir law while keeping the accelerating gap fixed, or $I_b \propto E_b^{3/2}$. Then the Coulomb term in Eq. 2.18 is $g_{6a} \sqrt{E_b/T_e}\, \sigma^{ion}(E_b)/\sigma^{e}(E_b)$. This would not provide a stronger variation of T_e with E_b than that of Eq. 2.20. Note that $\Gamma(T_e)$ is a rapidly increasing function of T_e. The fastest increasing of T_e with E_b will occur while $T_e < 1$ V, where $\Gamma(T_e)$ is small. Then

$$T_e = g_7 \sqrt{E_b} + g_{14} \quad . \tag{2.21}$$

Bear in mind that this is a very liberal upper bound on the variation of T_e with E_b. Realistically, the gas cooling term is non-negligible and one would expect T_e to vary more slowly with E_b than the upper bound given by Eq. 2.21.

Consider finally Eq. 2.18 while varying only n_g:

$$T_e^{3/2} = g_{15} + g_{16} \sqrt{T_e} - g_{17}\, \Gamma(T_e) n_g \tag{2.22}$$

This is a rather complicated expression, but clearly T_e is a decreasing function of n_g. How quickly T_e responds to n_g depends on the relative size of the terms in Eq. 2.22. In our plasma, the terms in Eq. 2.18, and hence Eq. 2.22, are all of similar size. T_e should respond most quickly to changes in n_g when $T_e > 1$ volt, since the fractional increase of $\Gamma(T_e)$ is greatest for $T_e > 1$ volt.

Chapter 3

Electron Heating by Beam Driven Plasma Oscillations

A. Introduction

We shall see in Experimental Results and Discussion, Section A that the classical power balance just detailed is not always adequate to explain the electron temperature we observe. In fact we find under some conditions that each beam ion must lose 36 V in addition to that lost by Coulomb collisions with the plasma electrons. In this chapter we explore the coupling of beam energy to plasma electrons by collective effects.

The velocity distribution of the plasma (shown in Fig. 3-1, neglecting plasma ions) is unstable. The neutralizer plasma is essentially magnetic field free ($B < 10g$ or $r_i/a_w > 2$, where r_i and a_w are the ion gyroradius and the neutralizer radius, respectively). The only collective oscillations with phase velocities (v_ϕ) slow enough to interact with the beam are the electrostatic modes - electron plasma and ion acoustic oscillations. Both of these modes are unstable in the presence of the proton beam. The electron and beam velocity distributions are shown in Fig. 3-1. The phase velocity of the ion acoustic (I-A) mode ($C_s = \sqrt{T_e/m_i}$) is very much less than the beam velocity ($C_s << v_b$). Thus the only unstable I-A wavevectors are those at nearly right angles to the beam. This limits the spatial growth of these I-A waves to a few e-foldings as they cross the transverse dimension of the beam. The potential for increasing the

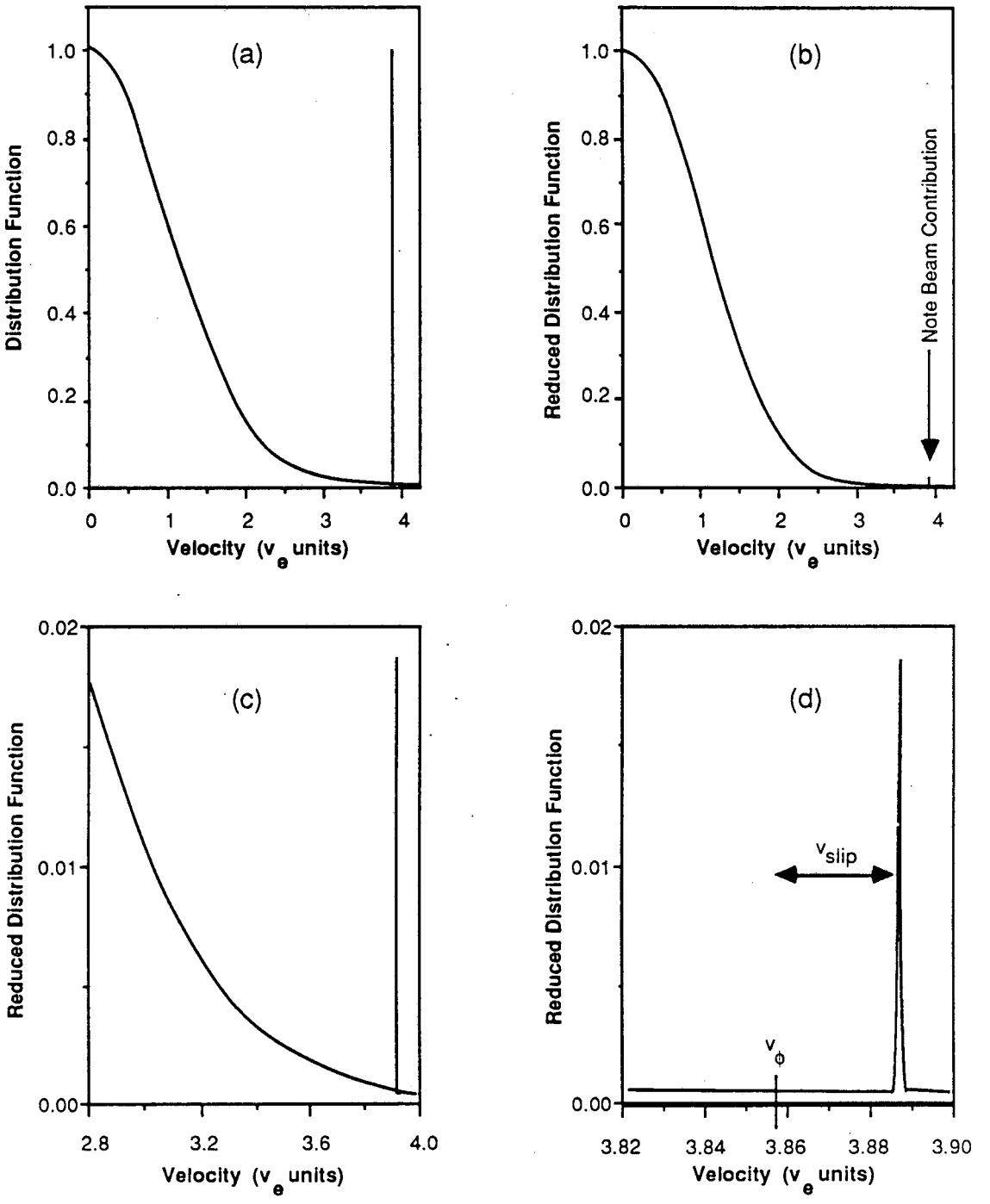

Fig. 3-1 Velocity Distribution Functions. a) Both the electron and beam distribution functions are normalized to a peak of unity. b and c) The reduced distribution function is normalized to a peak of unity. In the reduced distribution function, the beam contribution is reduced by a factor of R to represent its contribution to the dielectric function. d) Same. The wave phase velocitiy and the beam-wave slip velocity (calculated from Eq. 3.22) are indicated. For all: beam energy = 25 kV; electron temperature = 1.8 V; R = 0.00001.

transverse beam temperature is slight in our case. In systems of larger transverse dimension, this mode might bear consideration. We shall not discuss the I-A modes any further though, as (the electron thermal speed) $v_e >> C_s$, leaving no mechanism for coupling I-A wave energy back into the electrons.

The electron plasma mode (e-p), however, is a perfect vehicle for coupling beam energy into the plasma electrons. The largest amplitude waves will have wavevectors nearly parallel to the beam direction, due to the strong Landau damping experienced by waves propagating down the strong (relative to the axial gradient) radial density gradient. The phase velocity will be v_b, which is a few times v_e. Thus these oscillations are slightly Landau damped - a mechanism that transfers the energy of oscillation to kinetic energy of the bulk electrons, even for linear oscillations.

In the subsequent sections of this chapter we shall find the linear spatial growth rate for e-p oscillations in the uniform cold beam approximation. We shall find that for our plasma sufficient coupling exists to support the observed electron temperature. We shall then address corrections for spatial gradients and beam "temperature" and show in Experimental Results and Discussion, Section B.1 that the latter of these corrections give rise to a "threshold" for the instability. For the regime in which we have taken data, a dependence of $T_e \propto E_b$ appears. We shall also explore other regimes (E_b > 50 kV) where there is reason to suspect that this dependence will break down.

B. Linear Spatial Growth Rate

We consider the case of a cold uniform beam in a uniform plasma of warm electrons and cold ions. The dielectric function in this case is

$$\epsilon = 1 - \frac{\omega_i^2}{\omega^2} - \frac{\omega_e^2}{\omega^2 - 3k^2 v_e^2} - \frac{\omega_b^2}{(\omega - \underset{\sim}{k} \cdot \underset{\sim}{v}_b)^2} \tag{3.1}$$

where ω_i, ω_e, and ω_b are the ion, electron, and beam plasma frequencies respectively ($\omega_s = \sqrt{\frac{4\pi n_s e^2}{m_s}}$); $v_e = \sqrt{\frac{T_e}{m_e}}$ is the electron thermal speed (note we are implicity including Boltzmann's constant within T_e to avoid confusion with the wavevector); and v_b is the beam speed. As discussed in the introduction, the I-A mode is of little concern here, so we take $\omega^2 >> \omega_i^2$. For our plasma (and typical of neutralizers for positive ion beams)

$$R \equiv \omega_b^2/\omega_e^2 << 1 \tag{3.2}$$

Thus the last term in Eq. 3.1

$$\epsilon_b \equiv \frac{\omega_b^2}{(\omega - \underset{\sim}{k} \cdot \underset{\sim}{v}_b)^2} << 1 \tag{3.3}$$

unless

$$\omega = k \cdot v_b, \tag{3.4}$$

(the resonance condition). This is the case of beam particles moving along at the same speed as a point of constant phase travels in the beam direction; i.e., the beam is stationary in the wave frame. In view of Eq. 3.3, we expand the solution of $\epsilon = 0$ around

$$\epsilon_p \equiv 1 - \frac{\omega_e^2}{\omega^2 - 3k^2 v_e^2} = 0$$

The solution to this unperturbed plasma dielectric equation is

$$\omega^2 = \omega_e^2 + 3k^2v_e^2 \ , \tag{3.5}$$

the usual dispersion relation for warm electron plasma oscillations. We now apply the resonance condition, Eq. 3.4, to Eq. 3.5:

$$(\underset{\sim}{k}\cdot\underset{\sim}{v}_b)^2 = \omega_e^2 + 3k^2v_e^2$$

to find the resonant wavevector,

$$k_o^2 \equiv \frac{\omega_e^2}{v_b^2\cos^2\theta - 3v_e^2} \tag{3.6}$$

where θ is the angle between the wavevector $\underset{\sim}{k}_o$ and the beam: k_o will be the resonant wavelength. We now solve $\epsilon(\omega,k) = \epsilon_p + \epsilon_b = 0$, expanding around k_o,

$$\epsilon(\omega=\underset{\sim}{k}_o\cdot\underset{\sim}{v}_b,\ k_o + \delta k) = 0$$

$$\epsilon_p\ (\omega_o,k_o) + \delta k \cdot \frac{\partial\epsilon_p}{\partial k}\bigg|_{\omega_o,k_o} + \epsilon_b(\omega_o,k + \delta k) = 0$$

But $\epsilon_p(\omega_o,k_o) = 0$, so

$$\delta k = -\frac{\epsilon_b(\omega_o,k+\delta k)}{\dfrac{\partial\epsilon_p}{\partial k}\bigg|_{\omega_o,k_o}}$$

Now $\epsilon_b(\omega_o,k_o) = -\dfrac{\omega_b^2}{(\delta k\ v_b\cos\theta)^2}$

and $\dfrac{\partial\epsilon_p}{\partial k}\bigg|_{\omega_o,k_o} = -\dfrac{6\ k_o v_e^2}{\omega_e^2}$

Thus, we find, after arranging factors conveniently,

$$\delta k^3 = -\left(\frac{\omega_e}{v_e}\right)^3 \left(\frac{\omega_b}{\omega_e}\right)^2 \quad \frac{1}{\xi} \quad \frac{\sqrt{\xi - 3}}{6} \tag{3.7}$$

where $\xi \equiv v_b^o \cos^2\theta / v_e^2$. For E_b = 25 kV, m_b as the proton mass, and with T_e expressed in volts, we can numerically express

$$\xi \equiv 28 \cos^2\theta / T_e \tag{3.8}$$

The three solutions to eq. 3.7 are

$$\delta k = e^{i(\pi/3, \pi, 5\pi/3)} \left(\frac{R}{\xi} \quad \frac{\sqrt{\xi-3}}{6}\right)^{1/3} \quad \frac{\omega_e}{v_e}$$

The middle root is real and of no interest to us. The first root is evanescent. The third root is a spatially growing mode.

$$\mathrm{Im}(\delta k) = -\frac{3}{2} \left(\frac{R}{\xi} \quad \frac{\sqrt{\xi-3}}{6}\right)^{1/3} \quad \frac{\omega_e}{v_e} \tag{3.9}$$

$$R_e(\delta k) = .5 \left(\frac{R}{\xi} \quad \frac{\sqrt{\xi-3}}{6}\right)^{1/3} \quad \frac{\omega_e}{v_e} \tag{3.10}$$

In the wave frame, the beam velocity is

$$v_b' \equiv v_b \cos\theta - v_\phi = v_b \cos\theta - \frac{\omega_o}{k_o + R_e(\delta k)} \simeq \frac{v_b \cos\theta}{k_o} \quad R_e(\delta k) \tag{3.11}$$

Thus the beam is traveling slightly faster than the wave. Beam ions are then bunched and slowed down by the wave potential.

We use Eq. 3.8 in Eq. 3.6 to find

$$k_o \lambda_D = \sqrt{\frac{1}{\xi - 3}} \quad . \tag{3.12}$$

This helps us to calculate the resonant wavelength and spatial growth rate in Table 3-1. The plasma parameters of the second line are those requiring the largest anomalous power input; therefore that Im (δk) will be used when calculating the anomalous power input.

TABLE 3-1

E_b = 25 kV, $n_e = 10^{11}/cm^3$, $n_b = 1.7 \cdot 10^9/cm^3$, $\theta = 0$

T_e	λ_D	$k_o\lambda_D$	λ_o	$I_m(\delta k)$
1 eV	23μm	0.2	0.7mm	2.5/cm
1.8 eV	31μm	0.28	0.7mm	2.0/cm

These are the fastest growing roots. One can also solve the Quartic equation that results from Eq. 3.1 (neglecting the plasma ion term). One finds the same growing and evanescent modes as well as two stable modes. See Fig. 3-2 (these curves represent complex ω rather than complex k).

C. Field Energy Required

We find in Experimental Results and Discussion, Section A.5, that each beam proton must anomalously lose ΔE_{anom} = 36 V during its lifetime. This energy is that required for the power balance in our standard case: E_b = 25 kV, $n_e = 10^{11}/cm^3$, P_{gas} = 2.8 mT - and thus represents an upper bound for beam energy loss. This energy must first be transferred to the fluctuating field. The field energy density required to support the power balance is then

$$W_{req} = n_b \, \Delta E_{anom} \tag{3.13}$$

For our standard case, $W_{req} = 6 \cdot 10^{10} V/cm^3$.

To find an upper bound on the distance through which this oscillation must grow, we assume the noise level at Z=0 is thermal

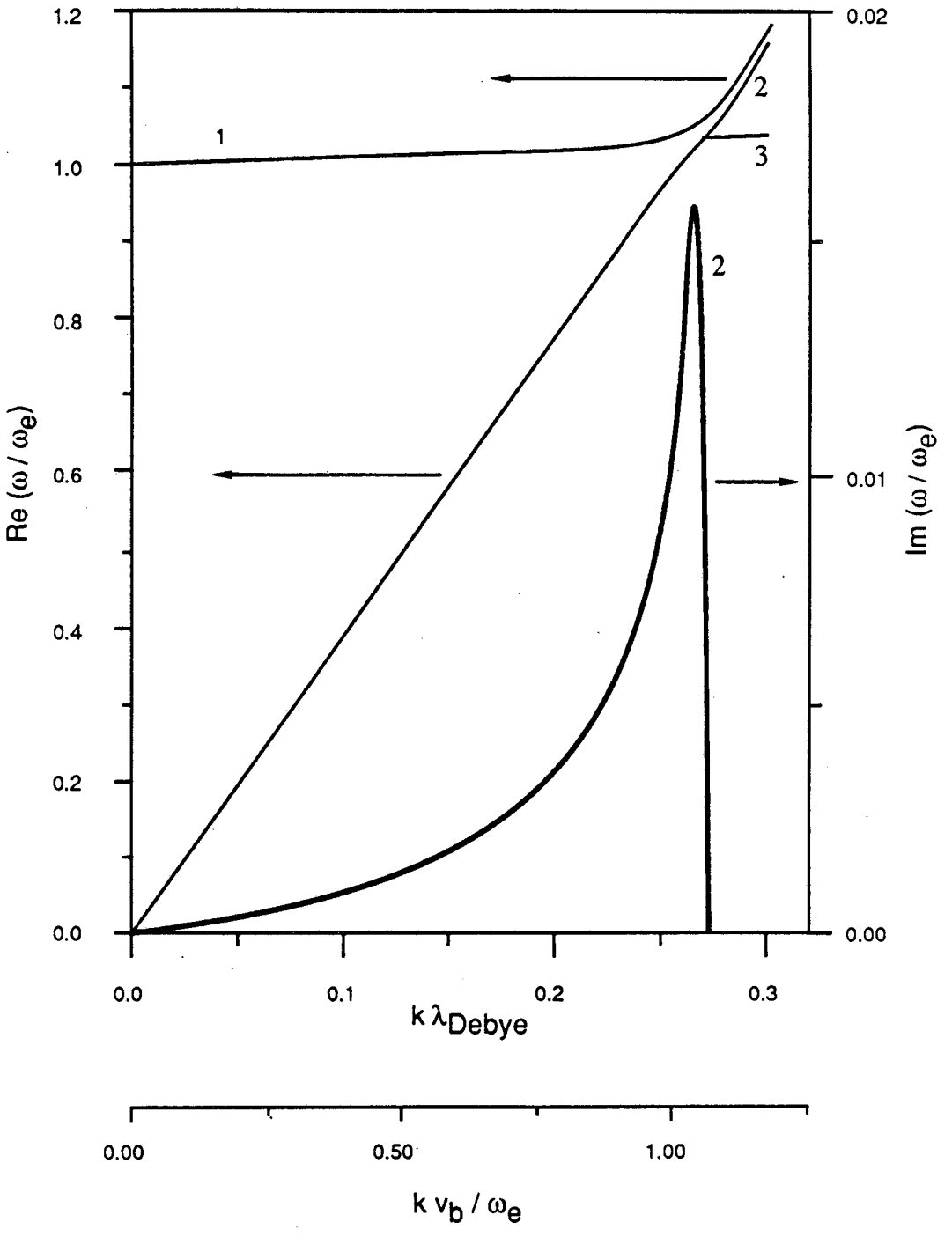

Fig. 3-2 Real and Imaginary Parts of the Wave Frequency. The real parts of the complex roots are shown as light lines. The imaginary part of the one growing root (labeled as 2) is shown as a thick line, and corresponds of the middle branch of the real parts. Roots 1 and 3 are real. Beam energy = 25 kV; electron temperature = 1.8 V ; R= 0.00001.

$$W_o = \frac{E_o^2}{4\pi} = \frac{k^2\phi^2}{4\pi} = \frac{T_e}{Vol_p}$$

where Vol_p is the volume of the plasma. Then the field energy density

$$W(z) = \frac{T_e}{Vol_p} e^{2Im(\delta k)z} . \tag{3.14}$$

For z_{req} such that $W(z_{req}) = W_{req}$, we find

$$Z_{req} = \frac{1}{2Im(\delta k)} \ln\left(\frac{W_{req}}{T_e} Vol_p\right) \tag{3.15}$$

$$= 8 \text{ cm for our standard case.}$$

Thus if no process limits wave growth to a distance less than z_{req} (8 cm), enough power can be taken from the beam to support the T_e's (1.8 eV @ E_b = 25 kV) we observe (or equivalently, the T_e scaling law we derive later in Sec. E.1).

There are two constraints regarding W_{req};

i. If waves are to behave linearly,

$$W_{req} < n_e T_e \tag{3.16}$$

ii. To avoid beam trapping by the oscillating potential,[11]

$$W_{req} < \left(\frac{R}{2}\right)^{1/3} n_b E_b \tag{3.17}$$

D. Axial Density Gradient

As the wave propagates down the neutralizer, the local plasma density drops. This axial decrease in n_e results from the neutral gas pressure gradient associated with the gas flow, and from the decrease in the effective cross section for ion production as the beam becomes neutralized through charge exchange (see Fig. C-1a). The latter effect will certainly dominate for Z < 10 cm, but two effects will

mediate this. Close to the accelerator, where the gas feeds from and expands to fill the neutralizer, the gas density is flatter than $1-\frac{z}{L}$. Secondly, the proximity of a wall at z=0 with ϕ_w=0 causes axial ion loss that supplements the radial ion loss (radial loss dominates for z>20 cm). For these reasons, and seeking a simple quantitative expression, we take n_e to have the same axial scaling as the gas density,

$$n_e(z) = n_e(z=0) \cdot (1 - \frac{z}{L}) \ . \qquad (3.18)$$

As a final argument in favor of Eq. 3.18, we note that z_{req} = 8 cm. A wave beginning at thermal level at z = 30 would have extracted enough energy by z = 40 to support the power balance. So even if there is a steeper n_e gradient for z < 10 cm, limiting wave growth there, there is a flatter n_e profile for z > 30 cm that can support the wave growth.

We see that ω_e is a decreasing function of z. As the wave propagates downstream, the local resonant frequency decreases. The wave frequency is then higher than the local resonant frequency. Eventually wave growth stops. We show in Appendix F that growth stops after a 5% decrease in ω_e, corresponding to a 10% decrease in n_e. Eq. 3.18 suggests that this change will take approximately 10 cm (L = 100 cm). This is slightly larger than z_{req} found in Section C, so we conclude that the wave can grow to sufficient amplitude to support the electron temperature we observe.

E. Steady-State Amplitude (Saturation)

We have been discussing a spatially growing mode. As there is a ("soft") boundary where the beam enters the plasma (z=0), it seems

appropriate to consider this as a boundary value problem. (The solutions to which are real w, complex k). However, there is no true constraint on the wave amplitude at z=0, only that the beam is unmodulated. The wave amplitude will be of thermal level or higher. Beam modulation may proceed at a larger spatial rate than that given by Eq. 3.9 if $W(z=0) > T_e/Vol$. Then z_{req} becomes an upper bound for distance over which the beam modulation grows.

The steady-state picture is then one in which W(z) begins at some value (of at least the thermal level), increases with z, and eventually damps back to the thermal level. This latter spatial damping is inevitable as the waves (resonant with the beam in one region) propagate into regions of lower n_e - where the value of $k\lambda_D$ eventually increases beyond 0.3 or so and Landau damping dominates. This puts the oscillating energy directly into the bulk electron distribution even if the wave remains linear.

There are two very different mechanisms for achieving this steady state, and they have very different consequences.

1. Quenching by thermal electrons

In the absence, or insignificance, of inelastic electron energy losses the electrons have very little inertia (or effective heat capacity) relative to the beam. Thus the beam is not significantly perturbed by the power removed by the wave and ultimately delivered to the electrons. In this steady-state scenario, the electrons have been heated enough by the unstable waves that the Landau damping by the bulk electrons balances the beam-plasma growth rate. W(z) remains constant in time, but the beam continues to lose energy as it passes

through the oscillating field. One can think of this as an initial value problem [W(z,t=0) is specified] and set γ_L (temporal Landau damping rate) equal to $\mathrm{Im}(\delta\omega_b)$ (temporal beam-plasma growth rate), since steady-state potentials are the same as their initial value.

The Landau damping rate is[12]

$$\gamma_L = \sqrt{\frac{\pi}{8}}\ \omega_e\ e^{-3/2}\ \left(\frac{1}{k\lambda_D}\right)^3\ \exp - \frac{1}{2}\left(\frac{1}{k\lambda_D}\right)^2 \tag{3.19}$$

For the initial value problem one can follow a derivation similar to that of section B, solving for real k, complex ω. The result is

$$\mathrm{Im}(\delta\omega_b) = \frac{3}{2}\left(\frac{R}{2}\ \frac{1}{\sqrt{1 + 3k^2\lambda_D^2}}\right)^{1/3}\ \omega_e \tag{3.20}$$

These are rates tabulated in Table 3-2 and plotted in Fig. 3-3. Take note that $\mathrm{Im}\left(\frac{\delta\omega_b}{\omega_e}\right)$ in Table 3-2 assumes that the wave is resonant, $k_o v_b = \omega_e \sqrt{1 + 3\ k_o^2\ \lambda_D^2}$. So, reading down Table 3-2, think of varying $k_o\lambda_D$ by changing T_e, as calculated from Eq. 3.12 in the second column. We see that $\mathrm{Im}(\delta\omega_b) = \gamma_L$ when T_e is such that $k_o\lambda_d \simeq 0.3$. In Table 3-1 we calculated $k_o\lambda_D = 0.28$ for our standard case, in excellent agreement.

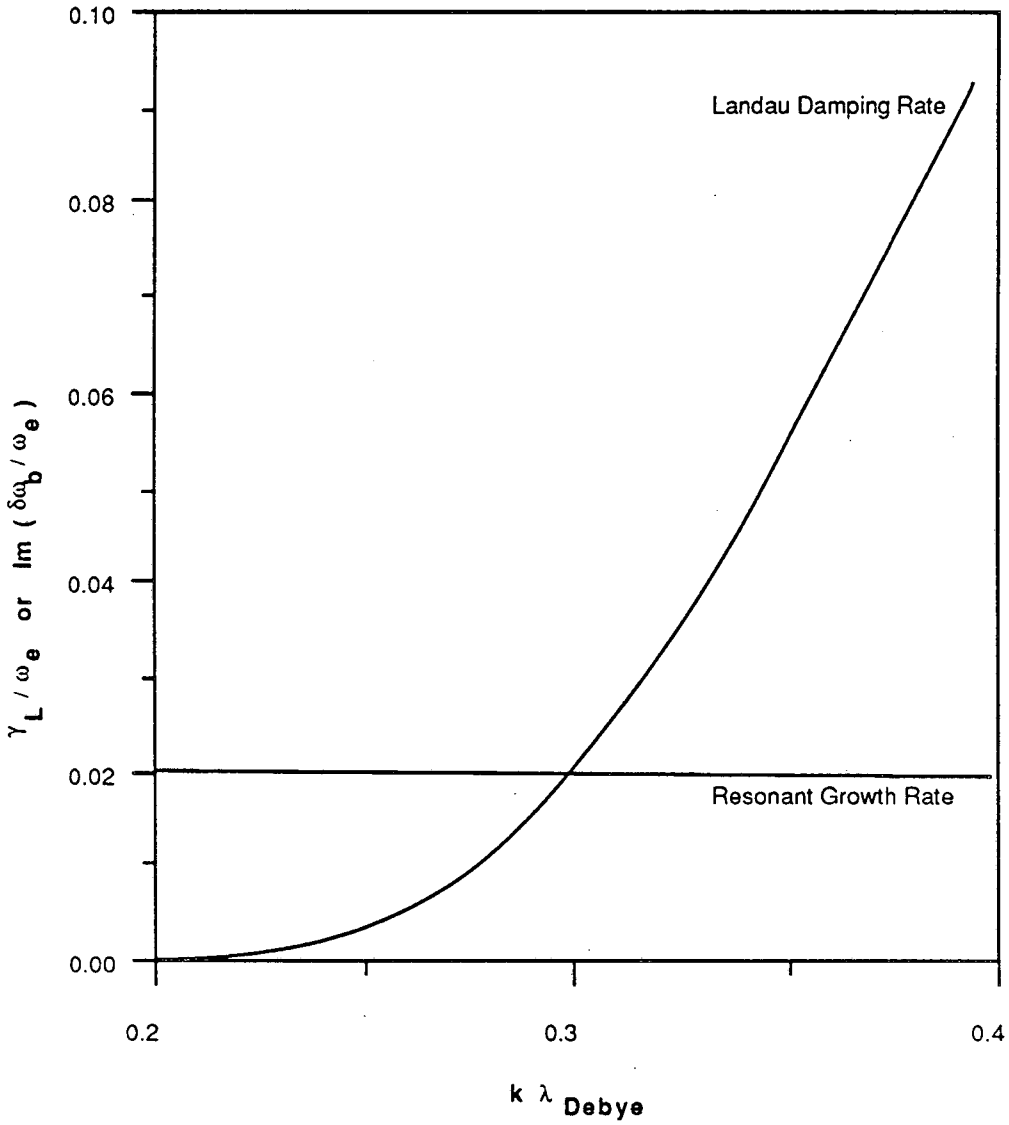

Fig. 3-3 Landau Damping Rate and Resonant Growth Rate as a Function of k lambda Debye.

Table 3-2

$R = 3 \cdot 10^{-5}$

$k_o\lambda_D$	T_e	γ_L/ω_e	$Im(\frac{\delta\omega_b}{\omega_e})$
0.1	0.28 V	$2.7 \cdot 10^{-20}$	$2.1 \cdot 10^{-2}$
0.15	0.60	$9.3 \cdot 10^{-9}$	"
0.2	1.02	$6.5 \cdot 10^{-5}$	"
0.25	1.50	$3.0 \cdot 10^{-3}$	"
0.3	2.02	$2.0 \cdot 10^{-2}$	"
0.35	2.56	$5.5 \cdot 10^{-2}$	"
0.4	3.09	$9.6 \cdot 10^{-2}$	"

The above arguments were made for fixed R. If we were to increase I_b and hence possibly R (assuming that n_e was unchanged), $Im(\delta\omega_b)$ only varies as $R^{1/3}$. In contrast, γ_L shows rapid variation with $k_o\lambda_D$. A significant change in R (say 100%) makes a slight (< 30%) change in $\delta\omega_b$. Because of the exponential nature of γ_L, the 30% change in γ_L required to maintain the steady state is accommodated by a temperature change $\Delta T_e < .1$ V. This suggests that for a wide variety of operating conditions, T_e will adjust itself so that $k_o\lambda_D \simeq 0.3$.

Since $k_o \simeq \frac{\omega_e}{v_b}$, a linear dependence of T_e upon E_b results from

$$0.3 = k_o\lambda_D \simeq \frac{\omega_e}{v_b} \quad \lambda_D = \frac{v_e}{v_b} \quad \text{or} \quad v_e = .3\, v_b \ .$$

Then

$$T_e = .18 \frac{m_e}{m_b} E_b \ . \tag{3.21}$$

Note that this expression is independent of n_e and therefore also independent of the neutral gas pressure, as well as independent of I_b.

In order to observe this scaling, the constraints laid out in Section C must be met - the anomalous power cannot exceed the power available from the wave; W is subject to the restraints of Eq. 3.16 and Eq. 3.17.

One can think of Eq. 3.21 as T_e clamping by negative feedback. If T_e is too low, temporal wave growth is unrestrained and more power is taken from the beam, raising T_e. Conversely, if T_e is too high, the wave is damped and less power is taken from the beam, lowering T_e.

2. Quenching By Beam Velocity Spreading

If the electron collisional power loss is too great to allow T_e to build up to a level so that $\gamma_L = \mathrm{Im}(\delta\omega)$, wave growth may be limited by an increase in the beam temperature, T_b. In this scenario both the electrons and beam ions are heated by the beam-plasma instability, but the spread in ion energy stabalizes the system while the electrons are still too cold to have a stabilizing effect.

For wave growth given by Eq. 3.20, the slip between the wave phase velocity and v_b is

$$v_{slip} = R_e\left(\frac{\delta\omega_b}{\omega_e}\right) v_b \approx \frac{1}{2}\left\{\frac{R}{2}\right\}^{1/3} v_b \qquad (3.22)$$

If v_{slip} exceeds the spread in beam velocties, Δv_b, all of the beam ions contribute to wave growth. On the other hand, if Δv_b exceeds v_{slip}, some beam ions are moving slower than the wave and can actually damp it. The growth rate is then smaller than that given by Eq. 3.20, as all the beam ions no longer act in concert. For $\Delta v_b > v_{slip}$, the cold-beam susceptibility in Eq. 3.1 is replaced by its warm-beam counterpart. The resonant instability is replaced by the kinetic instability, with greatly reduced growth rates.[13]

Although these kinetic growth rates do not vanish immediately for $\Delta v_b > v_{slip}$, for our purposes here, we shall assume the growth rate to be small enough so as to effectively stop further energy loss from the beam. Power transfer from the beam to the plasma electrons via this electrostatic instability then stops when

$$\Delta v_b > \left\{\frac{R}{2}\right\}^{1/3} v_b \ . \qquad (3.23)$$

The maximum kinetic energy loss of a beam ion is then

$$\Delta E_{max} = \left\{\frac{R}{2}\right\}^{1/3} E_b \ , \qquad (3.24)$$

which is typically a few % of E_b. Experimental data consistent with beam energy losses of a few percent have been observed by others.[14]

The beam temperature is increased to

$$T_b \equiv \frac{1}{2} m_b (\Delta v_b)^2 = \frac{1}{4}\left\{\frac{R}{2}\right\}^{2/3} E_b \ . \qquad (3.25)$$

The power available to heat the electrons is then

$$P_{max} = I_b \Delta E_{max}$$

$$= I_b\left\{\frac{R}{2}\right\}^{1/3} E_b \ . \qquad (3.26)$$

This corresponds to a wave energy density of

$$W_{max} = n_b \left\{\frac{R}{2}\right\}^{1/3} E_b \ , \tag{3.27}$$

which is observed at a distance

$$z_{max} = \frac{1}{2\ Im\ (\delta k)}\ \ell n\ \left(\frac{W_{max}}{T_e}\ Vol_p\right)$$

$$= \frac{1}{2\ Im\ (\delta k)}\ \ell n\ \left(\frac{n_b E_b Vol_p}{T_e}\ \left(\frac{R}{2}\right)^{1/3}\right) \tag{3.28}$$

$\simeq$ 9 cm for our standard case.

It should come as no surprise that W_{max} is the same as Eq. 3.17, the energy density at which the wave saturates by trapping the beam ions. In that case, the trapping potential in the wave frame is just that which overcomes the beam kinetic energy in the wave frame $(\frac{1}{2} m_b v_{slip}^2)$.

The discussion of saturation by beam thermal spreading is therefore simplified. It makes no difference whether the plasma is axially uniform, where the wave is monochromatic and saturates by trapping, or the plasma has an axial density gradient and a spectrum of wave frequencies is excited. In the latter case, stabilization occurs when the beam velocity distribution has been spread beyond v_{slip}, all parts of the excited spectrum contributing to the beam's energy loss and spread. Both saturation mechanisms lead to Eq. 3.26 for P_{max}.

It should be noted that while Eq. 3.26 assumes there is no continued growth beyond the point where $\Delta v > v_{slip}$, this is only an approximation. An order of magnitude expression for the kinetic

(warm-beam) growth rate is[13]

$$\gamma_{kin} \simeq R\left(\frac{v_b}{\Delta v_b}\right)^2 \omega_e$$

$$\propto \left(\frac{E_b}{\Delta E_b}\right)^2 \quad \propto \left(\frac{P_{max}}{P_{kin}}\right)^2 ,$$

where P_{kin} is some assumed power > P_{max}, the subscript indicating that this power is only available by wave growth proceeding at γ_{kin}. Thus, while the kinetic and cold-beam growth rates are roughly equal when $\Delta v_b \simeq v_{slip}$, at twice this spread in v_b, γ_{kin} is reduced by a factor of four. So we see that increasing the power into the plasma beyond P_{max} of Eq. 3.26 requires quadratically longer lengths through the plasma. To properly account for this, one would have to follow the wave growth and beam modulation numerically. Our goal here is to make some quick estimates as to what happens when the electron collisional drain negates the scaling derived in Section 1 above. Hence we take Eq. 3.26 as an upper bound.

3. Unquenched Systems

There is a third class of neutralizers that has yet to be mentioned. These would be neutralizers so short that the beam modulation is still undergoing rapid spatial growth as the beam exits the neutralizer. In this case the wave energy density near the exit of the neutralizer is

$$W(L) = \frac{T_e}{Vol} \; e^{2 \; Im \; (\delta k) L} \; .$$

The power delivered to the plasma is

$$P_L = A_b v_g \frac{T_e}{Vol} e^{2 \text{ Im } (\delta k) L} , \qquad (3.29)$$

where v_g is the wave group velocity.

This power would be balanced against the electron collisional losses. We have assumed that there is some region of falling density near the exit where the phase velocity drops toward the electron thermal speed and that all of the energy flux is delivered to the electrons. Also implicit in Eq. 3.29 is the assumption that the volume of the plasma that is participating in the oscillation is limited to that occupied by the beam. This is reasonable in view of the typical drop in electron density at the edge of the beam ($\sim e^{-1}$).

It seems unlikely that any such neutralizers exist, however. For example, in Eq. 3.28 we calculate that by z_{max} = 9cm, wave growth in our system will be limited by thermal spreading of the beam. Since $z_{max} < L/10$, we certainly don't expect significant spatial growth near the exit of the neutralizer. Due to the insensitivity of Im(δk) and hence of z_{max} to R, we anticipate $L >> z_{max}$ for all positive ion beam neutralizers. Therefore we would expect to see the instability quenched: quenched by electrons, where we observe the dependence $T_e \propto E_b$; or quenched by beam thermal spreading, where one finds T_e by completing the power balance using $P_{anom} = P_{max}$, given by Eq. 3.26. The latter topic will be the subject of the next section.

F. Power Balance in the High Temperature Regime

The electron temperature given by Eq. 3.21, $T_e = .18\ m_e/m_b\ E_b$, is only valid if the power required of the beam does not exceed that

available from the beam-plasma instability (Eq. 3.26). This expression is therefore limited to low temperature (T_e < 4 V) or low gas pressure (P_{gas} < 1 mTorr) cases. Otherwise the power available to the plasma will be limited by Eq. 3.26. We refer to this as the high temperature regime. We make the distinction of temperature rather than beam energy because the crossover between regimes will depend on parameters other than beam energy, such as gas pressure, system size, etc. Our aim is to provide the reader with a useful tool for estimating plasma conditions in a neutralizer. To arrive at a workable algorithm, some simplifying assumptions are inevitable.

We take an aside here to remind the reader that our system operates in the low temperature regime. We have shown in Section D that sufficient wave-coupling of beam power to the electrons exists so that the instability is saturated by resonant electrons, rather than by beam velocity spreading. At the beam energies available on our system (E_b < 34 kV), and the correspondingly low T_e's (T_e < 3 V), the low inertia (or alternately, low heat capacity) of the electrons allows them to be easily warmed until there are enough resonant electrons to saturate the instability. The steady-state description of the plasma in this case is simple - T_e is determined by E_b, independent of the other system variables and the plasma density is found by requiring that the radial ion flow at the beam edge equal the ion production rate within the beam. The plasma density is therefore a function of T_e, E_b, gas pressure, and system dimensions: but since T_e is determined by Eq. 3.21, $T_e = .18\ m_e/m_b\ E_b$, all of these variables are known and the plasma density can be calculated in a

straightforward manner. The self-consistent description of the beam is made trivial by the insensitivity of T_e to all variables except E_b.

In the high temperature regime, described in this and the following section, no such simplification occurs. Instead, T_e is depressed by inelastic collisions with gas molecules - the electrons can no longer be warmed until there are enough resonant electrons to saturate the beam-plasma instability. One might envision the inelastic collisions as effectively increasing the heat capacity of the electrons beyond that of the beam - thus the instability saturates, instead, by spreading the beam velocity distribution, the distribution with the lower effective heat capacity. As a result, we must analyze self-consistently the steady-state condition of the plasma.

As we have no experimental data in the high temperature regime, this section and the following section are untested descriptions of the steady-state plasma, in which we self-consistently solve both the particle balance and power balance. We begin by evaluating the particle balance to find the plasma density.

1. Plasma Production and Electron Density

We first seek an approximation for the electron density, allowing for ion production by plasma electrons, as well as by beam particles. The number of ions produced in a volume of $A_b \cdot dz$ inside the beam is

$$S^{ion} A_b \, dz = n_g\{I_b^+ \sigma_{cx} + I_b \sigma_{ion} + n_e \langle\sigma v\rangle_{ion} A_b\} \, dz, \qquad (3.30)$$

where S^{ion} is the ion production (source) rate and I_b^+ is the part of the beam current that has not yet charge- exchanged. The first of the

simplifying measures appears in Eq. 3.30 - we have dropped the 14 beam species in favor of a two species model.

These ions accelerate towards the wall under the influence of the ambipolar potential. This problem has been solved in slab geometry[15,16] and in cylindrical geometry.[1,16] From these solutions we see there is typically a potential drop of order T_e across the production region.

When the electron production term in Eq. 3.30 is small compared to the beam term, we can assume there is a variation of potential across the beam of T_e; $\delta\phi_b \simeq T_e$. In general, though, the electron contribution should be included, and may even dominate. As an estimate of the potential change across the beam in the general case, we take

$$\frac{\delta\phi_b}{T_e} = \frac{\text{\# ions produced inside beam}}{\text{\# ions produced inside whole plasma}} < 1$$

$$= \frac{I_b^+ \sigma_{cx} + I_b \sigma_{ion} + n_e \langle\sigma v\rangle_{ion} A_b}{I_b^+ \sigma_{cx} + I_b \sigma_{ion} + n_e \langle\sigma v\rangle_{ion} A_p}, \qquad (3.31)$$

Unfortunately, this expression is a function of n_e and T_e, and, through I_b^+, also a function of n_g and z.

The ion radial velocity at the beam edge (a_b) is

$$v_i \approx \sqrt{\frac{2\delta\phi_b}{m_i}}$$

where m_i is the mass of the plasma ions. Balancing the plasma production inside $A_b \cdot dz$ with the radial ion flux out of the bounding surface $S_b \cdot dz$, where S_b is the perimeter of the beam, gives the

electron density at the beam edge,

$$n_e(a_b) = \frac{\{I_b^+ \sigma_{cx} + I_b \sigma_{ion} + n_e \langle\sigma v\rangle_{ion} A_b\} n_g}{\sqrt{\frac{2\delta\phi_b}{m_i}} S_b}, \qquad (3.32)$$

where we assume quasineutrality and require the use Eq. 3.31 for $\delta\phi_b$. In general, the first two terms in the numerator should be replaced by the sum over all beam constituents, as has been done in Appendix C. Then Eq. 3.32 would hold at any axial position, provided the production terms are evaluated at that position. For the sake of simplicity, we shall restrict ourselves to $E_b > 50$ kV where $I_b^+/I_b^o > 50\%$.[17] Thus we shall simplify Eq. 3.32 to

$$n_e(a_b) \simeq \frac{\{I_b(\sigma_{cx} + \sigma_{ion}) + n_e \langle\sigma v\rangle_{ion} A_b\} n_g}{\sqrt{\frac{2\delta\phi_b}{m_i}} S_b} . \qquad (3.33)$$

Note that plasma production by electrons increases $n_e(a_b)$ in two ways: 1) by increasing the total production rate and 2) by decreasing $\delta\phi_b/T_e$ (see Eq. 3.31), and hence the ion loss speed.

For $r > a_b$, we find n(r) in the steady-state by continuity,

$$\underset{\sim}{\nabla} \cdot (n \underset{\sim}{v}) = S^{ion} . \qquad (3.34)$$

$$\text{or} \quad \int_S n \underset{\sim}{v} \cdot d\underset{\sim}{S} = \int_{Vol} \frac{dn_i}{dt} S^{ion} dV , \qquad (3.35)$$

where Vol is inside the bounding surface S. When S^{ion} is dominated by beam production, we take $S^{ion} = 0$ outside the beam. For cylindrical

geometry, the flux through any cylindrical surface of $r > a_b$ is constant. The outward flowing ions are already traveling at the ion acoustic speed ($\delta\phi_b \simeq T_e$), so we assume v_i is approximately constant. Then

$$n_e(r) = n_e(a_b)\,\frac{a_b}{r} \qquad (r > a_b) \tag{3.36}$$

When plasma production is beam-dominated, the density profile is as sketched in Fig. 3-4a. The density falls to $n_e(o)/e$ at $r = a_b$, then falls as $1/r$ to a_w.

When plasma production is mostly by electrons, $\delta\phi_b \ll T_e$, and the T_e potential drop is across the whole plasma. Fig. 3-4c is a sketch of $n_e(r)$ in this case. We approximate n_e as uniform.

When plasma production by beam and plasma are roughly equal, $\delta\phi_b < T_e$, as suggested by Eq. 3.31. Then $n_e(a_b) > n_e(o)/e$. Also, because of the local plasma production for $r > a_b$, the density no longer falls as $1/r$. One might imagine the density would be a superposition of the previous two cases, with $n_e(o)$ of each scaled to the respective fraction of total plasma production. Fig. 3-4b is a sketch of $n_e(r)$ for this case.

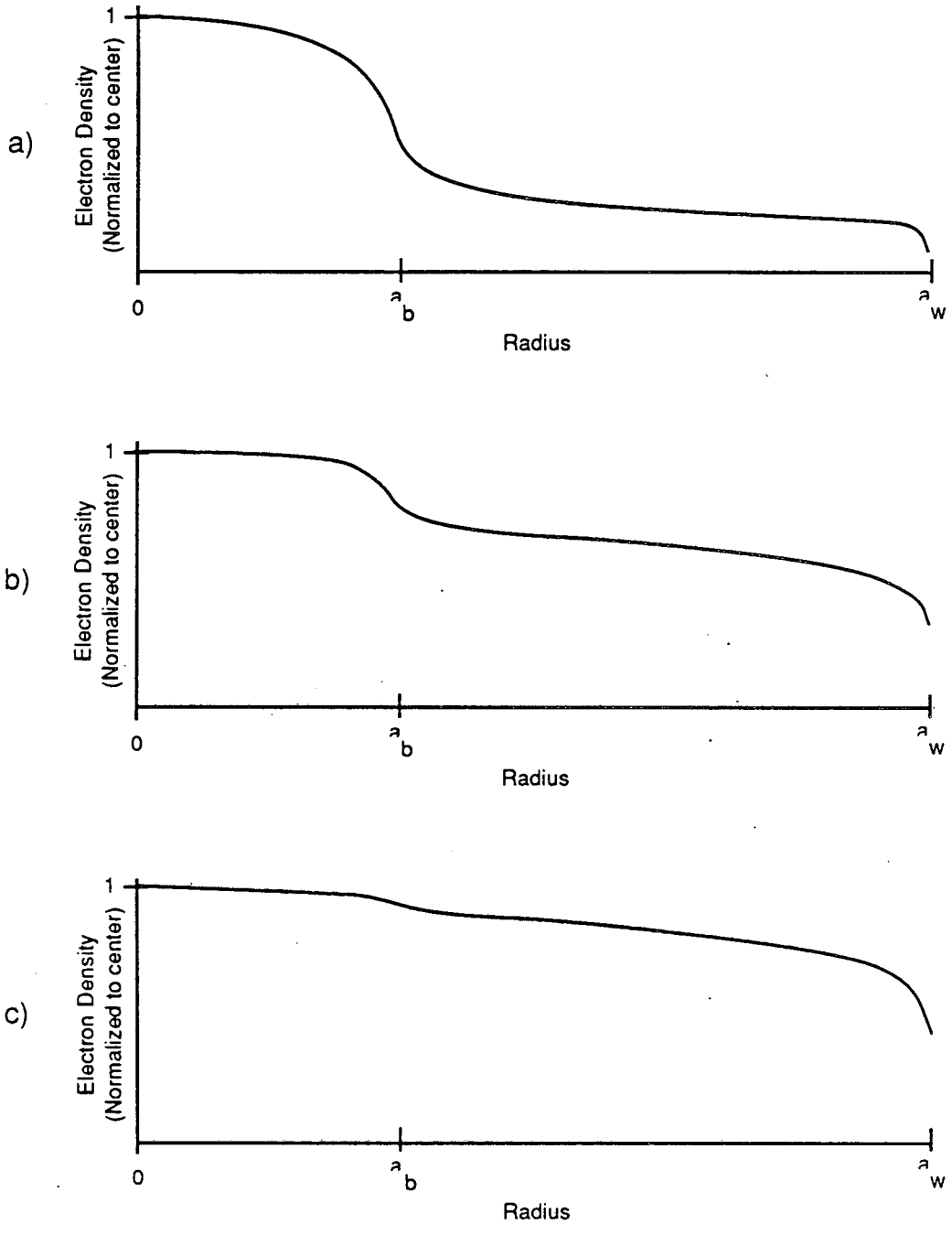

Fig. 3-4 Plasma (or electron) Density Sketched as a Function of Radius. a) Plasma production is beam-dominated. b) Plasma production is approximately shared by plasma electrons and beam particles. c) Plasma production is dominated by electrons.

2. Power Balance

The power lost by electron-gas collisions is

$$P_{inel}(T_e,n_g) = \int_0^L \int_{A_p} n_g(z)\, n_e(x,y,z)\, \Gamma(T_e)\ dx\, dx\, dz \qquad (3.37)$$

Recognizing this as the biggest power loss for $T_e > 3$-4 eV, we ignore the T_e of kinetic energy that each electron carries out of the wall (in two velocity components parallel to the wall), the trapped energy ($\phi - E_N$), and the power transfer of Coulomb collisions. Consider the integration over the plasma area in Eq. 3.37,

$$I_1 \equiv \int_{A_p} n_e(x,y,z)\, dxdy\ .$$

For beam-dominated plasma production in cylindrical geometry, we can approximate $n_e(r < a_b) \simeq n_e(o)$ and use Eq. 3.36 for $n_e(r > a_b)$:

$$I_{1,b} \simeq n_e(0,z)\, A_b + 2\pi\, n_e(a_b,z)(a_b a_w - a_b^2)$$

$$\simeq n_e(a_b,z)[A_b + 2A_p\, a_b/a_w]\ . \qquad (3.38)$$

We have used $\delta\phi_b \simeq T_e \rightarrow n_e(r = 0) = n_e(a_b)e^{\delta\phi_b/T_e} \simeq 3\, n_e(a_b)$. The subscript b on $I_{1,b}$ is a reminder that this calculation is valid for beam production only.

Now consider the axial integration of Eq. 3.37,

$$I_2 \equiv \int_0^L n_g(z)\, I_1(z)\, dz$$

Recalling our restriction to $E_b > 50$ kV, we have been and shall continue to neglect the axial evolution of the beam. With this in mind, using Eq. 3.33 and 3.38, we see that the remaining axial

dependence to be integrated in I_2 is

$$I_3 \equiv \int_0^L n_g^2(z)\, dz$$

$$= n_g^2(o) \int_0^L (1 - \frac{z}{L})^2\, dz$$

$$\frac{L\, n_g^2\,(o)}{3}$$

Then with the above in Eq. 3.37,

$$P_{inel} = I_2\, \Gamma(T_e)$$

$$\simeq \frac{1}{3}\, \frac{I_b}{S_b} \sqrt{\frac{m_i}{2\delta\phi_b}}\, (\sigma_{cx} + \sigma_{ion})(A_b + \frac{2a_b}{a_w}\, A_p)(1+\zeta) n_g^2(o) L \cdot \Gamma(T_e) \quad (3.39)$$

where we have included the electronic plasma-production term with

$$\zeta \equiv \frac{n_e \langle\sigma v\rangle_{ion}\, A_b}{I_b(\sigma_{cx} + \sigma_{ion})} \quad (3.40)$$

We see that ζ is the ratio of electronic plasma-production to beam plasma-production. Taking care to evaluate $\delta\phi_b$ from Eq. 3.31 for $\zeta > 0$, Eq. 3.39 might come close to predicting P_{inel} up to $\zeta = 1$. For $\zeta > 1$, Eq. 3.39 would certainly underestimate P_{inel}, falling short in I_1 for $r > a_b$.

Finally, the power balance in this high temperature, beam-dominated plasma production case is found by equating P_{inel} of Eq. 3.39 with P_{anom} of Eq. 3.26. T_e is then found to be that which satisfies

$$\Gamma(T_e) \sqrt{\frac{m_i}{2\delta\phi}} = \frac{3S_b\{\frac{R}{2}\}^{1/3}\, E_b}{(A_b + \frac{2a_b}{a_w}\, A_p)(\sigma_{cx} + \sigma_{ion})(1 + \zeta)\, n_g^2(o)} \quad (3.41)$$

Eq. 3.26 is an upper bound for the power available. If we find T_e from Eq. 3.41 to be greater than that of Eq. 3.21, T_e will be given by the lower of the two upper bounds, Eq. 3.21.

There are some noteworthy points to Eq. 3.41: 1) As long as $\zeta \ll 1$ (then R is independent of I_b) T_e is independent of I_b, just as before. This is because both the beam power available and the plasma power consumption ($\propto$ density, and hence, $\propto$ plasma production) are proportional to I_b. 2) No longer is T_e independent of n_g. Strong dependence upon n_g as well as upon system dimensions is apparent. 3) Unless $\zeta \ll 1$, Eq. 3.41 is more complicated than it might seem, as ζ is a function of T_e and n_e. In this case an iterative solution is necessary.

G. Power Balance When Production Is Dominated by Thermal Electrons

This discussion is really an extension of the previous section, but it will point out sufficient differences to merit separation. We shall eventually show that for some neutralizers, plasma production dominated by electrons is feasible. For neutralizers consisting of metal vapor targets (Cs, Mg, ...) this section may very well be appropriate.

In the last section, we defined ζ as the ratio of electronic-to-beam plasma production, and we are concerned here with $\zeta > 1$. This also corresponds to the onset of neutralizer "burn-out". In a typical neutralizer the total flow of gas molecules is a few times I_b [in our neutralizer, for example, the gas flow is
6 Torr Liter/sec = $2.2 \cdot 10^{20}$ particles/sec and we have beam currents up

to 10 Amp or I_b (@ 10 Amp) = $6 \cdot 10^{19}$ particles/sec], say $I_g \sim 3I_b$. Then if each beam proton charge exchanges once, one third of the gas flow is being pumped radially to the walls as charge exchange ions. There are also ions resulting from ionization carrying a gas flux to the wall. On the wall these ions recombine, but as neutrals they return from the wall with some small fraction of their ~ 10 V incident energy. This results in heating of the gas, which reduces the gas density and hence the neutralization efficiency of the neutralizer. If we compound this by having $\zeta > 1$, a large fraction of I_g will be ionically pumped to the wall and thusly heated, thereby reducing n_g. So we see that $\zeta > 1$ is an indicator of impending neutralizer burn-out.

The plasma electrons do not heat the gas directly, because of their low mass. By ionization, the electrons can heat the gas indirectly, as discussed above. Also, plasma ions can heat the gas directly, as they have mass similar to that of the neutral gas. This collisional gas heating by the plasma ions is of a magnitude similar to the heating by ionic wall recombination discussed above, as we shall now show. The gas molecular cross sections are of order $10^{-15} cm^2$ for plasma ions with energy of a few volts. Our gas density is of order 10^{14} cm^{-3}. Ions tranverse approximately 10 cm of neutral gas before reaching the wall, and thus make on the order of one collision with a gas molecule. To the extent that the kinetic energy transferred in such collisions is similar to the kinetic energy of neutrals returning from a wall recombination event, gas heating by these two processes will be similar.

In a functional neutralizer, each beam ion makes approximately one charge exchanging collision,

$$n_g \sigma_{cx} L \simeq 1 \tag{3.42}$$

For simplicity we assume an axially uniform system. Equating the integrated ion flux at the beam edge to the number of ions generated/sec,

$$n_i v_i 2\pi a_b L = (\sigma_{cx} + \sigma_i) I_b n_g L (1 + \zeta)$$

we find

$$n_i = \frac{(\sigma_{cx} + \sigma_i) I_b n_g (1 + \zeta)}{2\pi a_b v_i} \tag{3.43}$$

For beams of non-circular cross section, replace $2\pi a_b$ with S_b. With $I_b = n_b v_b \pi a_b^2$ and Eq. 3.42,

$$\frac{n_i}{n_b} = \frac{(\sigma_{cx} + \sigma_i)}{\sigma_{cx}} \frac{v_b}{v_i} \frac{a_b}{2L} (1 + \zeta) . \tag{3.44}$$

Using this in Eq. 3.40, we find

$$\frac{\zeta}{1 + \zeta} = \frac{\langle \sigma v \rangle_{ion}}{\sigma_{cx} v_i} \frac{a_b}{2L} . \tag{3.45}$$

Then $\zeta >> 1$ when T_e is such that (using $v_i = 10^6 \sqrt{2T_e/m_i}$, if T_e units are V and m_i units are A.U.)

$$\frac{\langle \sigma v \rangle_{ion}}{\sqrt{2T_e/m_i (\text{in A. U.})}} = \frac{2 \cdot 10^6 L}{a_b} \sigma_{cx} . \tag{3.46}$$

It may at first seem odd to find $\zeta >> 1$ from an expression where by appearance it seems to have been treated as a small parameter. In fact the only violation here is the assumption of $\delta\phi_b \sim T_e$, when that potential drop should appear across the whole plasma. This is

remedied in Eq. 3.47. Typical neutralizers have $L/a_b \gtrsim 10$. Let us evaluate Eq. 3.46 for our neutralizer at $E_b = 25$ kV. We have $L = 100$ cm, $\sigma_{cx} = 5 \cdot 10^{-16}$ cm^2, $a_b = 3.5$ cm, and $m_i = 2$ A.U.:

$$\frac{\langle \sigma v \rangle_{ion}}{\sqrt{T_e(V)}} = \frac{2 \cdot 10^8 \quad 5 \cdot 10^{-16}}{3.5} = 3 \cdot 10^{-8} \text{cm}^3/\text{sec}$$

Note that the units of T_e disappeared in the numerical expression of Eq. 3.46. This ionization rate is greater than that at $T_e = 10$ V. The upper bound for T_e given by Eq. 3.21 in this case is 2.5 V. So at $E_b = 25$ kV, it is not possible to have $\zeta \gg 1$.

Consider the criterion of Eq. 3.46 for our system operating at 100 kV. Now $\sigma_{cx} \sim 3 \cdot 10^{-17}$ cm^2, so plasma production is dominated by electronic ionization when

$$\frac{\langle \sigma v \rangle_{ion}}{\sqrt{T_e}} = \frac{2 \cdot 10^8}{3.5} \quad 3 \cdot 10^{-17} = 1.7 \cdot 10^{-9} \text{cm}^3/\text{sec},$$

which is satisfied for $T_e > 9$ V. This T_e is below the upper bound of Eq. 3.21 for $E_b = 100$ kV, so we must assume electron-dominated plasma production is a possibility, although we need to determine if P_{anom} is large enough to support this.

Bear in mind that a number of assumptions have been made along the way to this concern over burn-out. We have assumed optimum line density of n_g (Eq. 3.42). We have taken Eq. 3.21 as an upper bound for T_e; now let us see if the power balance will allow T_e to be that high. We begin by assuming $\zeta \gg 1$, then shall need to verify whether that is indeed the case.

When $\zeta \gg 1$, the particle balance no longer determines n_e. Let us equate the flux of ions at the wall with the number of ions

generated inside (per unit length and per unit time):

$$n_i(a_w)\ v_i\ S_p = \bar{n}_e \langle\sigma v\rangle_{ion}\ n_g\ A_p\ , \tag{3.47}$$

where $\bar{n}_e$ is the average of n_e over the neutralizer area, and S_p and A_p are the perimeter and area of the plasma cross section, respectively. Both sides are proportional to n_e. Using the usual T_e potential drop across the production region, $n_i\ (a_w) \simeq n_i(o)/e$. Then

$\bar{n}_e \simeq (2\text{-}3) \cdot n_i(a_w)$. We will take $\bar{n}_e/n_i(a_w) \simeq 2$.

This equation actually determines T_e. We rearrange to find,

$$\frac{\langle\sigma v\rangle_{ion}}{\sqrt{\frac{2T_e}{m_i}}} \simeq \frac{S_p}{2n_g A_p} \tag{3.48a}$$

$$\simeq \frac{1}{n_g a_w}\ , \tag{3.48b}$$

where the latter applies for cylindrical geometry. Kino and Shaw[16] have solved the particle balance in cylindrical geometry numerically using the fluid description. Their solution shows the same result, but with the numerator (1) from the RHS of Eq. 3.48b replaced by 0.8. It does at first appear odd that T_e is determined by the gas density and system size. This is a consequence of particle production as well as loss being proportional to the plasma density. The electron temperature is the sole variable responsible for maintaining equal production and loss rates.

Eq. 3.48 therefore also defines an upper limit to T_e. When we include the beam production term in the RHS of Eq. 3.47, the only way

to contain the production rate to a level that is not greater than the loss rate (LHS of Eq. 3.47) is for T_e to be less than that defined by Eq. 3.47 (the $\simeq$ of Eq. 3.48 is replaced by <). Though this might appear to reduce the loss rate by limiting v_i, this is not the case. The ion density increases to compensate. For our neutralizer, with $n_g = 10^{14}/cm^3$, $a_w = 10$ cm, and $m_i = 2\ m_p$, the ionization-limited temperature set by Eq. 3.48b is $T_e^{IL} = 7$ V.

If we assume optimum gas density (Eq. 3.42) then Eq. 3.48 becomes

$$\frac{\langle\sigma v\rangle_{ion}(T_e^{IL})}{\sqrt{\frac{2T_e^{IL}}{m_i}}} = \frac{L\ \sigma_{cx}\ S_p}{2\ A_p} \quad , \tag{3.49a}$$

$$= \frac{L\ \sigma_{cx}}{a_w} \quad , \tag{3.49b}$$

which is a decreasing function of E_b. Because σ_{cx} decreases beyond $E_b \sim 30$ kV, T_e^{IL} is a decreasing function of E_b. For example with $E_b = 150$ kV (where $\sigma_{cx} = 7 \cdot 10^{-18} cm^2$) Eq. 3.49 requires $T_e^{IL} = 3.25$ V for $a_w = 10$ cm.

With Eq. 3.48 or Eq. 3.49 determining T_e, we are now in a position to complete the power balance. We balance the inelastic losses of Eq. 2.5 with P_{anom} from Eq. 3.26:

$$n_e n_g\ r(T_e^{IL})\ Vol_p = \{\frac{R}{2}\}^{1/3}\ I_b E_b \quad . \tag{3.50}$$

or

$$n_e^{4/3} = \left(\frac{n_b m_e}{2\ m_b}\right)^{1/3} \frac{I_b\ E_b}{n_g r(T_e^{IL}) Vol_p} \tag{3.51}$$

Note that with plasma production dominated by thermal electrons, T_e is determined by the particle balance and n_e is set by the power balance. In complete contrast, for beam-dominated production, n_e is determined by the particle balance and T_e satisfies the power balance. Of course in the beam-dominated case n_e and T_e are self-consistent, but n_e plays only a weak role in the power balance.

We now ask if the power balance of Eq. 3.50 is consistent with the original assumption of $\zeta \gg 1$. Solving Eq. 3.50 for n_e and inserting into Eq. 3.40, we find

$$\zeta = \left(\frac{R}{2}\right)^{1/3} \frac{1}{n_g \mathrm{vol}_p} \frac{\langle\sigma v\rangle_{ion} E_b}{\Gamma(T_e^{IL})} \frac{A_b}{\sigma_{cx} + \sigma_i} . \qquad (3.52a)$$

If we assume operation at optimum gas density, i.e. using Eq. 3.42,

$$\zeta = \left(\frac{R}{2}\right)^{1/3} \frac{A_b}{A_p} \frac{\langle\sigma v\rangle_{ion} \phi_i}{\Gamma(T_e^{IL})} \frac{E_b}{\phi_i} \frac{\sigma_{cx}}{\sigma_{cx} + \sigma_i} \qquad (3.52b)$$

We can calculate R by use of Eq. 3.44, thusly:

$$R \equiv \frac{m_e}{m_b} \frac{n_b}{n_e}$$

$$= \frac{m_e}{m_b} \frac{2L}{a_b} \frac{\sigma_{cx}}{\sigma_{cx} + \sigma_i} \sqrt{\frac{T_e}{2E_b}} \frac{1}{1 + \zeta} \qquad (3.53)$$

Using this in Eq. 3.52 and placing the $1 + \zeta$ factor on the LHS,

$$\zeta(1 + \zeta)^{1/3} = \left(\frac{m_e}{m_b} \frac{2L}{a_b} \frac{\sigma_{cx}}{\sigma_{cx} + \sigma_i} \sqrt{\frac{T_e^{IL}}{2E_b}} \right)^{1/3} \cdot$$

$$\frac{A_b}{A_p} \cdot \frac{\langle\sigma v\rangle_{ion}\phi_i}{\Gamma(T_e^{IL})} \cdot \frac{E_b}{\phi_i} \cdot \frac{\sigma_{cx}}{\sigma_{cx} + \sigma_i} \qquad (3.54)$$

To generalize Eq. 3.54 to beams of non-circular cross section, replace a_b by $2A_b/S_b$.

We see from Fig. 3-5 that the third factor (fractional ionization power),

$$\eta \equiv \langle\sigma v\rangle_{ion}\, \phi_i/\Gamma(T_e) \ ,$$

lies in the range 0.1 to 0.4 for most of the electron temperatures of interest, and for estimation purposes, we take it here as 1/4. At E_b = 150 kV, $\sigma_i \sim 10^{-16}\text{cm}^2$ and $\sigma_{cx} \sim 7\cdot10^{-18}\text{cm}^2$, so $\zeta \simeq 0.4$. Recall that Eq. 3.54 was derived for optimum gas density and $\zeta >> 1$. Finding $\zeta < 1$ does not really invalidate our work. The real constraint to Eq. 3.54 is that some mechanism limits T_e to below the value given by Eq. 3.21, so that P_{anom} is correctly given by Eq. 3.26. We found that T_e^{IL} in Eq. 3.49 was an upper bound. This is also an upper bound for ζ even when $\zeta < 1$. Recall that following Eq. 3.46 we found $\zeta >> 1$. That was only a possibility, ignoring the power requirements; having now done the power balance, we find that there is insufficient power available from the beam to support $\zeta >> 1$ at E_b = 150 kV. What does ζ = 0.4 mean anyway? Since ζ is defined as the ratio of ions produced inside the beam by electrons to those produced by the beam, the impact on gas pumping by the beam is $\frac{A_p}{A_b} \cdot \zeta$. We have assumed $n_g\, \sigma_{cx}\, L = 1$ (i.e., the neutralizer still works), so ζ = 0.4 only means that the gas pumping by the beam is at least $\frac{A_p}{A_b} \cdot 40\%$ larger than might have been expected. To retain $n_g\sigma_{cx}L = 1$ could require $\frac{A_p}{A_b} \cdot \frac{I_p}{I_g} \cdot 40\%$ more gas flow than expected from the cold fill, but not a complete neutralizer burn-out.

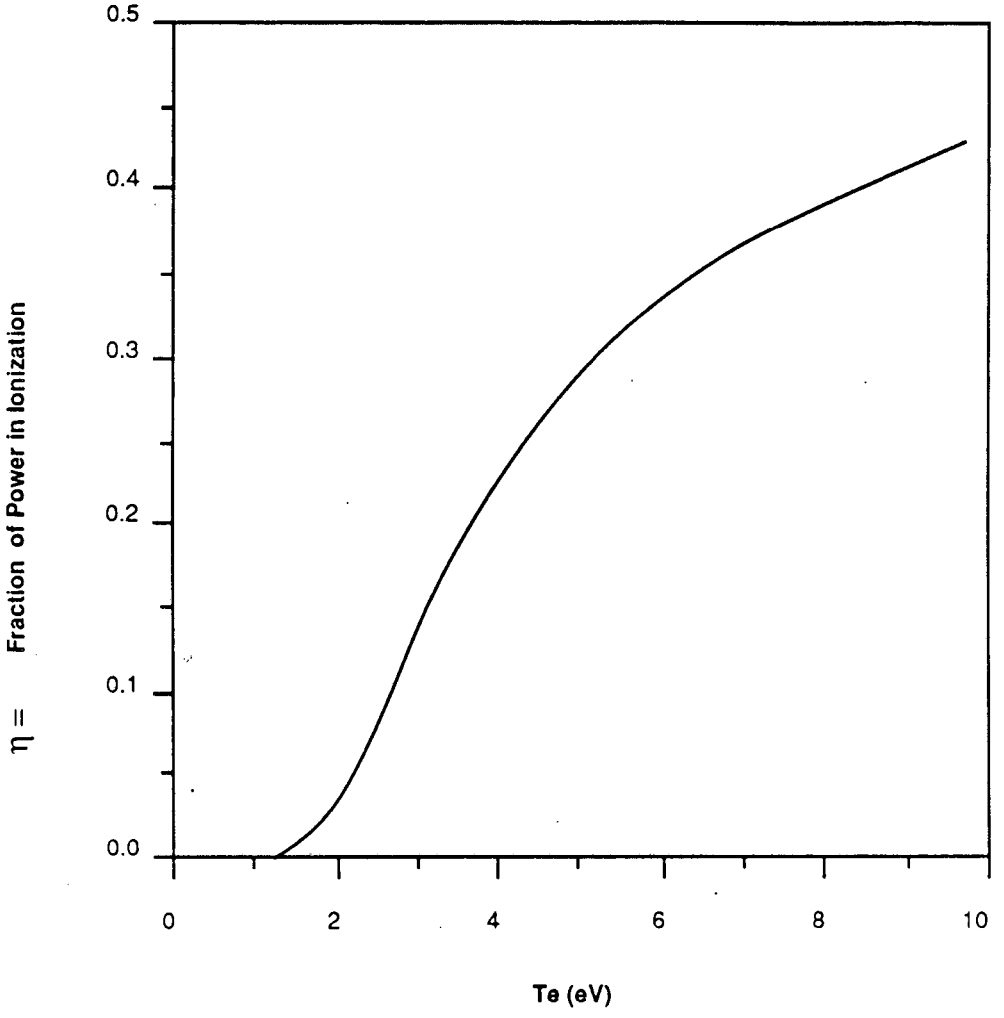

Fig. 3-5 Fraction of Electron Inelastic Collisional Losses Due to Ionization. Data has been taken from Reference #4 and smoothed.

Eq. 3.54 is plotted versus E_b in Fig. 3-6. Since the anomalous power available (see Eq. 3.26) increases linearly with E_b, it seems counter-intuitive that ζ could be a decreasing function of E_b. But let us look back again at Eq. 3.52 a and b. By using Eq. 3.50, the anomalous power balance, we have tied the electronic ionization rate in Eq. 3.52a to the fraction, η, of P_{anom} available for ionization. The electronic ionization rate is therefore independent of n_g, being fixed only by the power available. The beam ionization rate is, however, proportional to n_g. Because of our assumption of optimum gas density, n_g is an increasing function of energy. Quite simply, this latter energy dependence (seen as $\sigma_{cx}/(\sigma_{cx} + \sigma_{ion})$ in Eq. 3.52b and Eq. 3.54) dominates over the very weak T_e (and hence, E_b) dependence of η. The ratio A_b/A_p appears because ζ is defined as the ratio of ions produced by electrons inside the beam to those produced by the beam itself.

Note, however, that the volume-integrated rate of plasma production by electrons is an increasing function of beam energy;

$$\int_{vol_p} \frac{dn_i}{dt}\, dxdydz = I_b\left(\frac{R}{2}\right)^{1/3} \eta \frac{E_b}{\Phi_i}$$

Because of the rapid fall of σ_{cx} with energy, though, the neutralizer gas pressure increases with beam energy, so that beam production of plasma eventually outsteps electronic ionization.

If one were to consider a metal vapor neutralizer (Cs or Mg), one might expect $\zeta >> 1$, since Φ_i is less than that for H_2 and the ratio of rates taken as 1/4 when evaluating Eq. 3.54 will likely be more

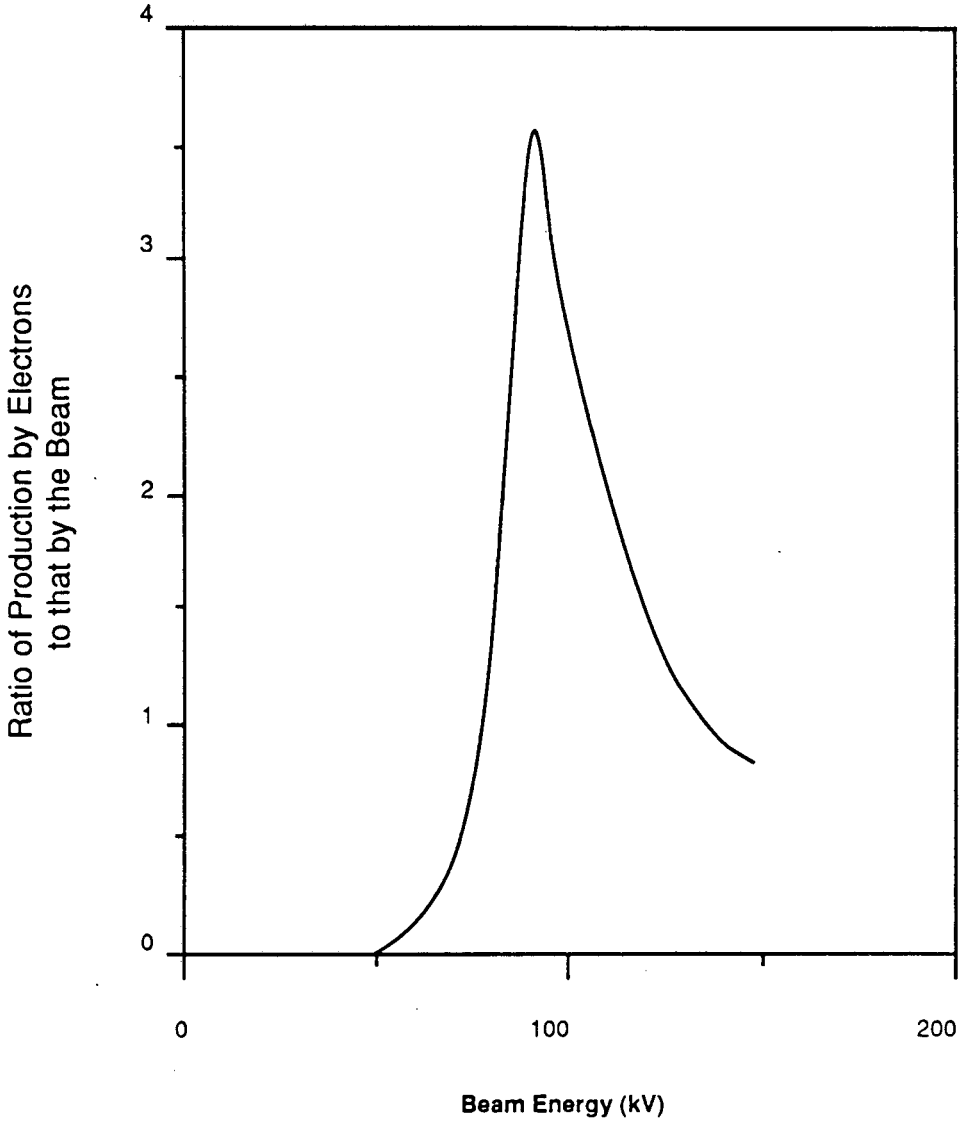

Fig. 3-6 Ratio of Production by the Plasma Electrons to Producion by the Beam. For Beam Energies below 90 kV, the curve has been calculated from Eq. 3.45. For energies 90 kV and above, Eq. 3.54 has been plotted.

near 1/2. Burn-out of Mg vapor targets has been observed,[18] although the authors believed that the beam-to-electron Coulomb power transfer was sufficient to drive the ionization.

H. Summary and Algorithm

In Section B we calculated the linear growth rate. In Section C we determined the wave energy density required to support the T_e we observe and found that this wave energy density is reached after the beam travels only 8 cm, a reasonable distance. We demonstrated in Section D that dn_e/dz will stop wave growth after 10 cm and thus concluded that in our neutralizer T_e could be supported at its anomalously high level by these beam-driven plasma oscillations.

The first of three upper bounds upon T_e (Eq. 3.21) was found in Section E.1 when wave growth is stopped by electron heating. We shall call this T_e^{sat}. The second and possibly more stringent upper bound is a result of beam velocity spreading, reached when P_{max} (Eq. 3.26) $< P_{anom}$, which in the high T_e limit we approximate as P_{inel} (Eq. 3.37). The formal expression of this is found in Section F, Eq. 3.41. The unwelcome possibility of overwhelming ionization by thermal electrons was explored in Section G. We find T_e fixed by Eq. 3.48 or 3.49, but this also turns out to be a third upper bound on T_e even when $\zeta < 1$. With P_{max} as the driving power, we find a formal expression for ζ in Eq. 3.54, which when evaluated suggests $\zeta < 4$ (see Fig. 3-6). We conclude then that some observable gas heating will occur, but that neutralizer burn-out is unlikely.

We now propose an algorithm for finding T_e, n_e, and ζ in any positive-ion neutralizer.

1. Find T_e^{Sat} from Eq. 3.21; call this $T_{e,1}$.
2. Evaluate Eq. 3.48 or 3.49 for T_e^{IL}. If $T_e^{IL} < T_e^{Sat}$, $T_{e,1} = T_e^{IL}$.
3. Calculate n_i from Eq. 3.43; assume $\zeta = 0$ the first time through.
4. Calculate ζ from Eq. 3.40.
5. Find the next guess for T_e from Eq. 3.41; call this $T_{e,Next\ i}$.
6. If $T_{e,2} > T_{e,1}$, $P_{anom} < P_{max}$ and the instability is quenched by thermal electrons; $T_e = T_e^{Sat}$, go to #9.
7. If T_e has not converged, go to #3.
8. If $T_{e,i} > T_e^{IL}$, $T_e = T_e^{IL}$. Go to #3; don't change T_e.
9. Calculate $n_i(=n_e)$ from Eq. 3.43.
10. Calculate ζ from Eq. 3.40.

Chapter 4

Experimental Apparatus

Figure 4-1 is a sketch of the apparatus. Indicated schematically are the plasma source, accelerator, and neutralizer. All the diagnostics are inserted at the z=30 cm location, unless stated otherwise.

A. Plasma Source

The source of ions for the accelerator has been characterized in detail elsewhere.[19] We shall provide only a brief description. The plasma source is shown in Fig. 4-2. The 28 tungsten filaments forming the cathode are arranged around the perimeter of the 20-cm diameter by 10-cm deep chamber. After the filaments are heated to emission temperature, the 12 ms duration arc voltage (50-120 V, repetition rate 0.5 - 2 / min.) is applied between the ring anode and the cathode (filaments). The discharge produces a plasma of density a few times 10^{12} /cm^3 in the source gas (usually hydrogen) of pressure approximately 10 mTorr. The cylindrical source wall and extraction plate holding the beam-forming electrodes are floating.

B. Accelerator

The two gap accelerator (one accel and one decel, the latter to prevent backwards acceleration of electrons produced in the neutralizer) is of a type that has been described elsewhere[20] and is sketched in Fig. 1-1 and Fig. 5-6. There are 10 ribbon beamlets

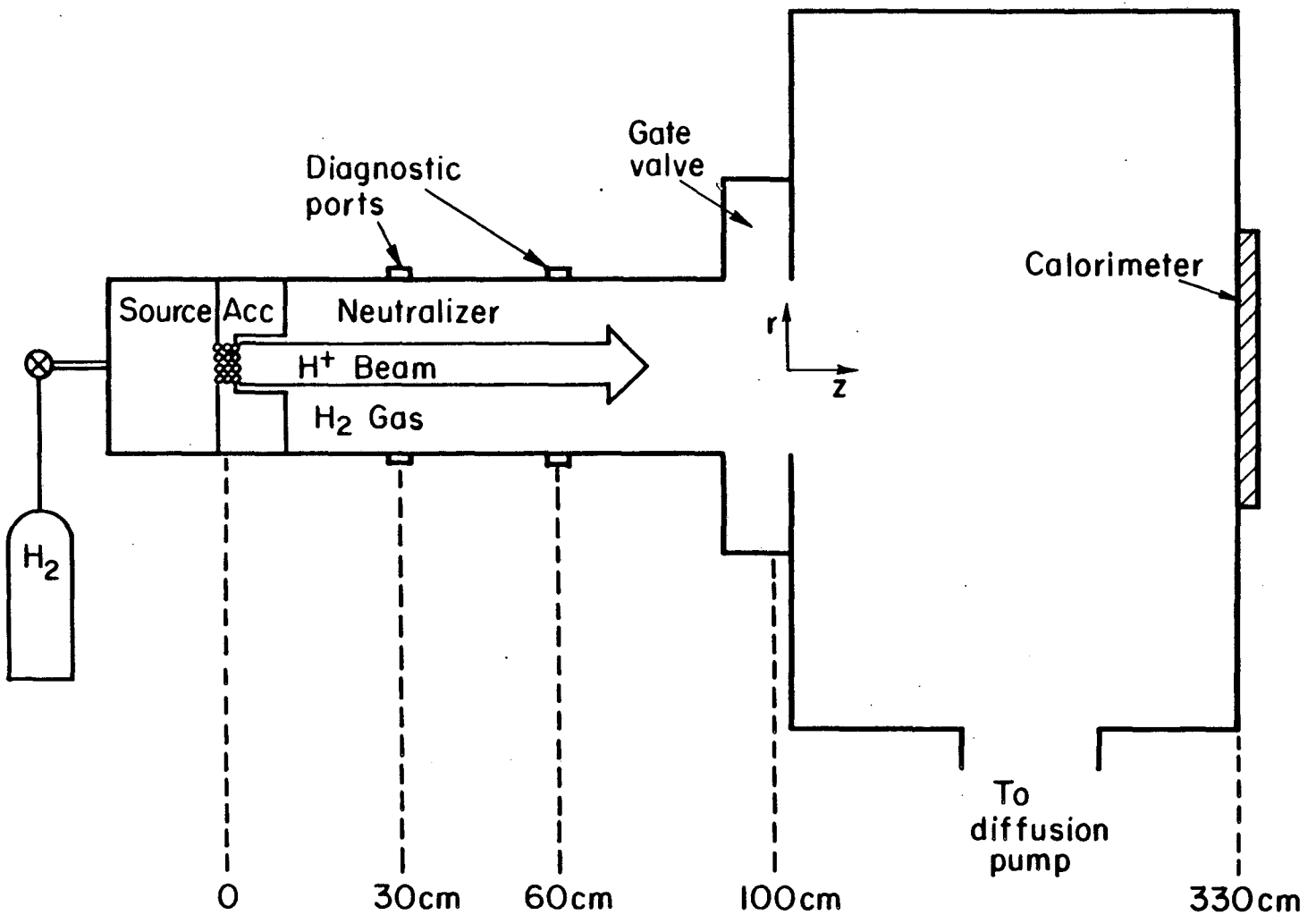

Fig. 4-1 Neutral-Beam-Line Schematic.

XBL824-3758

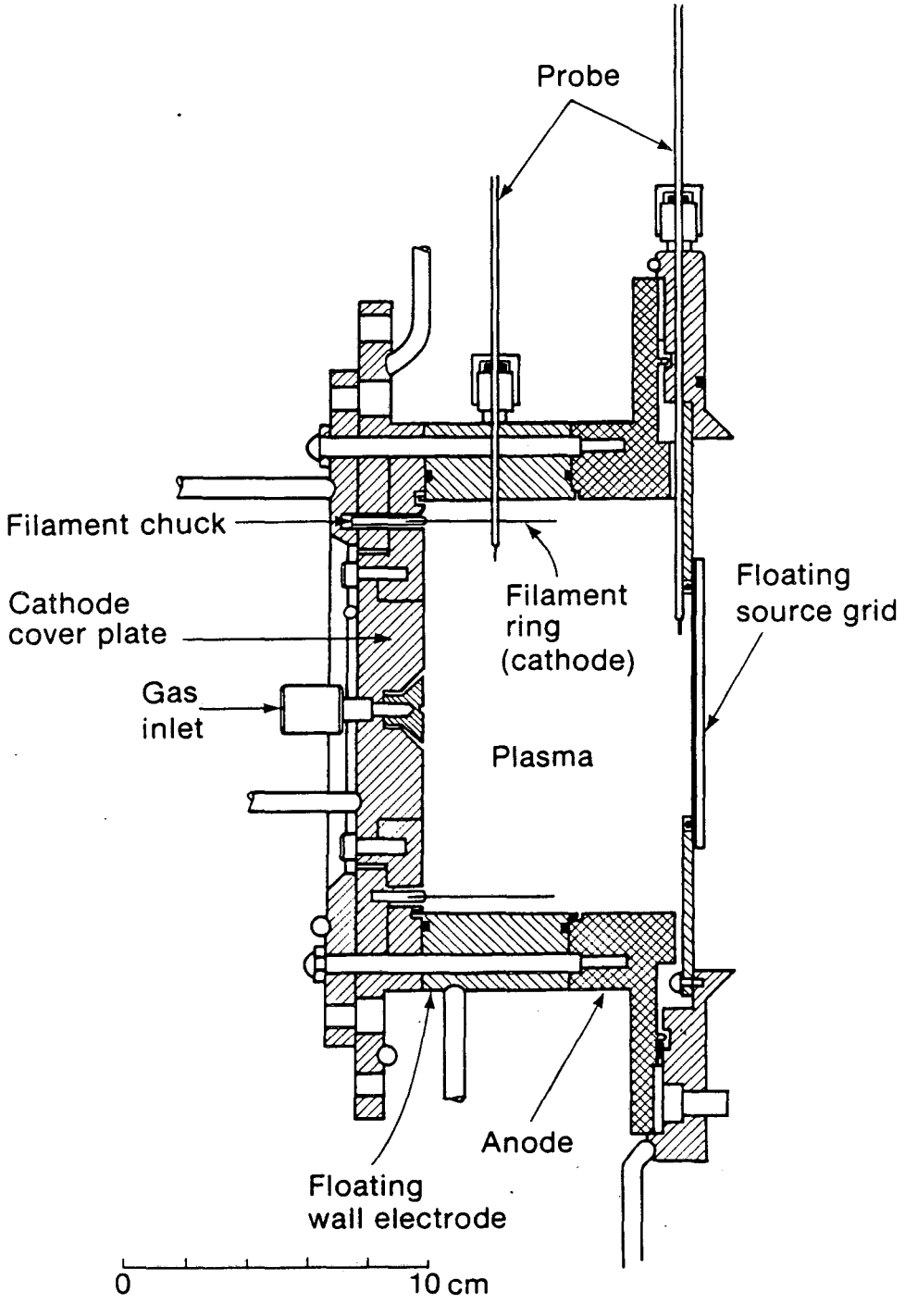

Fig. 4-2 Cross Sectional Schematic of the Ion Source.

forming a 7-cm x 7-cm beam. The source ions fall into the space between the 11 beam-forming electrodes and are accelerated by the electrostatic potential. The accelerating potential is switched on 2 ms after the arc voltage, thus allowing the arc to stabilize first. This gives a beam of 10-ms duration. The accelerator and power supplies are capable of 40-kV operation. In the interest of reliability, data acquisition was restricted to 34 kV.

C. Neutralizer

The neutralizer for the beam is a 1-m long, 20-cm diameter, gas (usually hydrogen)-filled aluminum pipe. Vacuum (base pressure ~ few times 10^{-7} Torr) for the neutralizer, as well as the source, is provided by a diffusion pump. A 3000-liter vacuum vessel accommodates the 300 ms gas pulse that pre-fills the neutralizer (and source) before the beam is turned on. Diagnostic ports are available at z = 7.5, 30, 45, and 60 cm. There are four ports separated azimuthally by 90 deg. available at z = 30 cm, allowing simultaneous diagnostics at that axial position.

D. Diagnostics

1. Langmuir Probe

The plasma density and electron temperature at z=30 cm are determined from the current-voltage characteristic, an example of which is shown in Fig. 4-3a, of a swept Langmuir probe. The short duration and low duty cycle of our beam, coupled with a low plasma density, require an external method for cleaning the probe collection

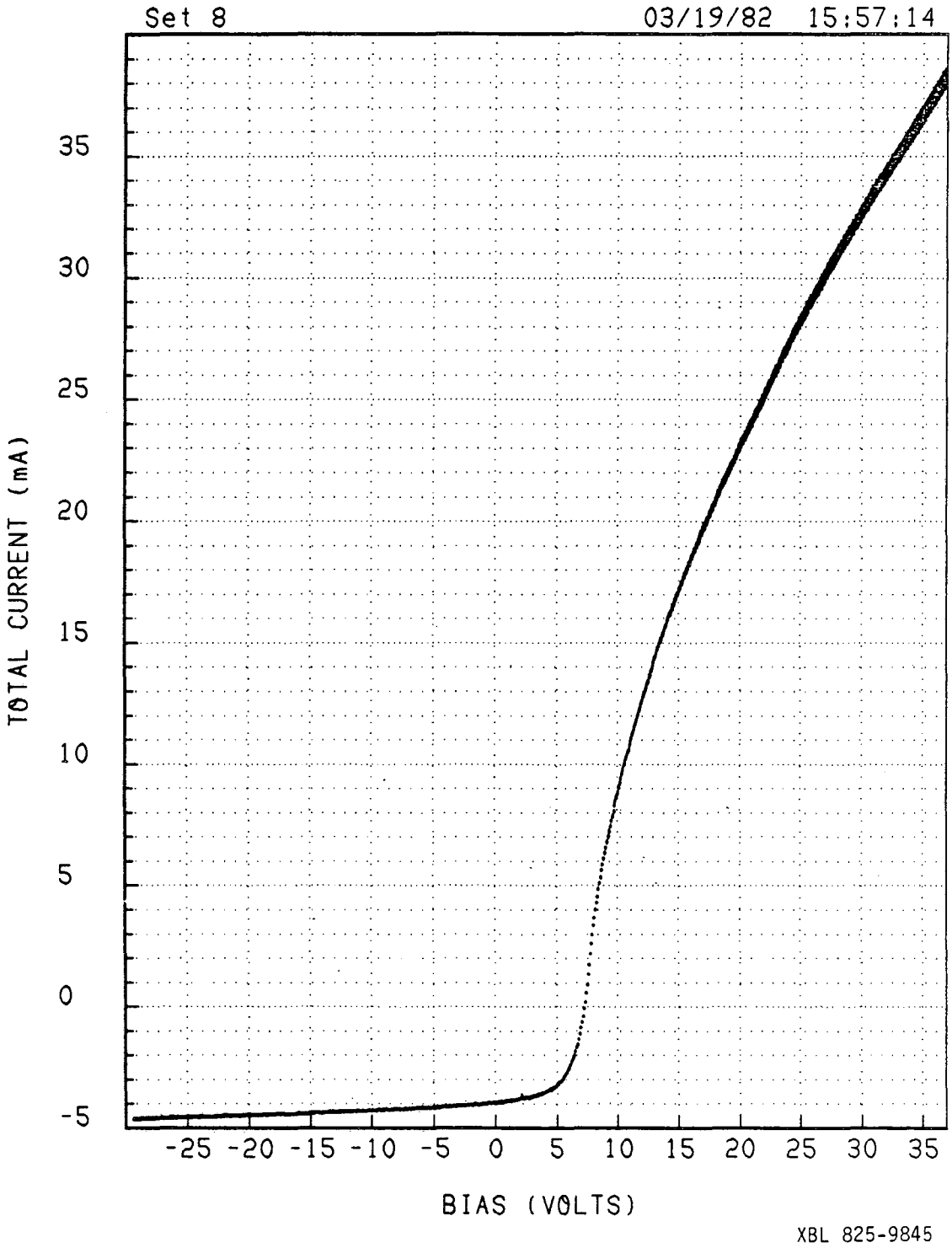

Fig. 4-3a Typical Langmuir Probe Current-Voltage Characteristic.

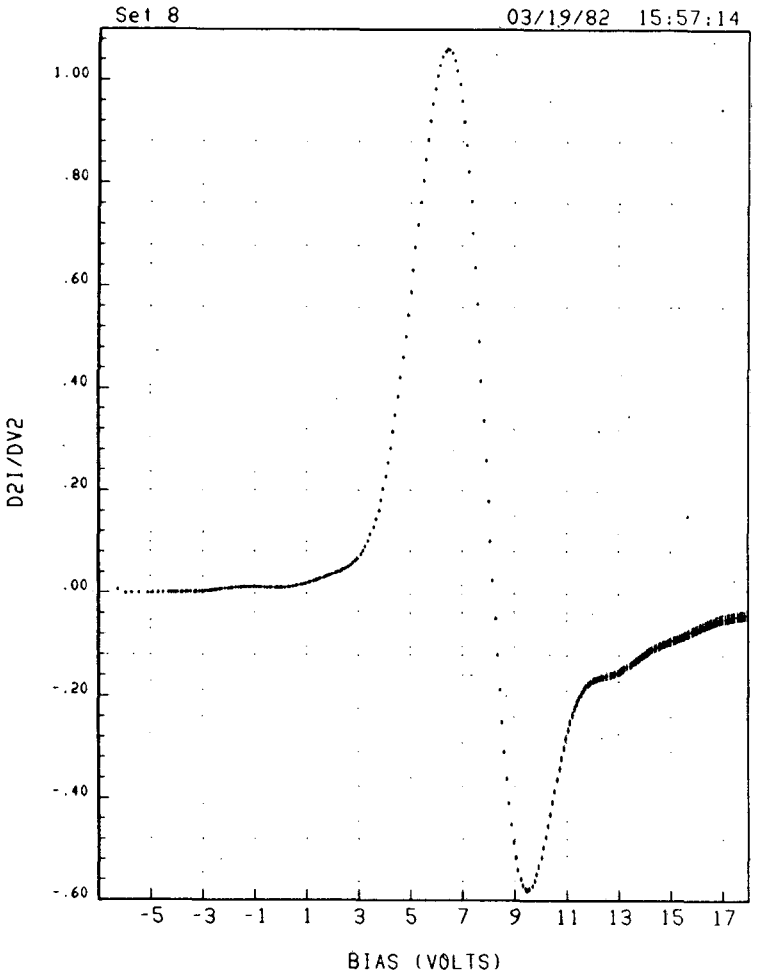

Fig. 4-3b Second Derivative of Current With Respect to Voltage. From Fig. 4-3a.

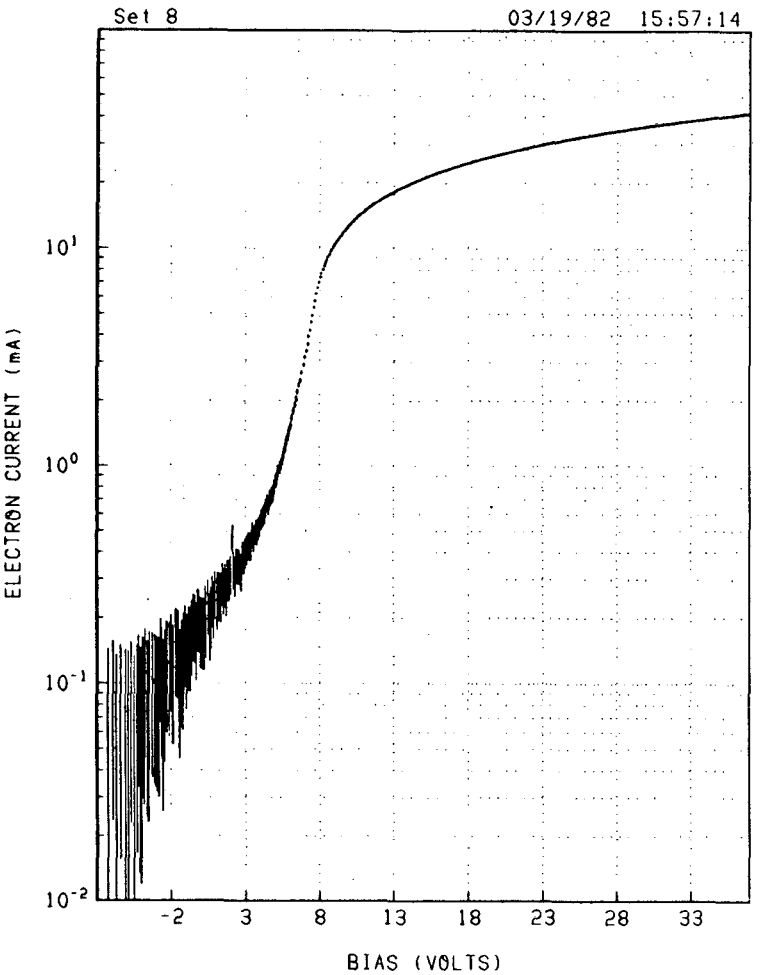

Fig. 4-3c Electron Current to the Probe. An extrapolation of the ion current has been subtracted from Fig. 4-3a.

surface. The latter was found to be essential for the acquisition of reliable and reproducible data. In systems with longer pulse duration or higher plasma density, it is possible to clean the probe surface by drawing large currents to the probe. The probe was formed by a 0.002-in. diameter (a_p = 0.0025 cm), 2.5-cm long loop of tungsten wire through which we could pass a current in order to clean by heating to incandescence. As long as the probe was cleaned this way within 1/2 second before the beam was initiated, no ill effects associated with dirty probe surfaces were observed. Conversely, the probe could not be heated within 100 msec of the beam turn-on, since, in this still warm state, it could be driven emissive by the beam. The Debye length in the plasma ranges from 30 to 70 μm, so we are operating near the orbital motion limit of current collection (thick sheath), where $\lambda_D > a_p$.[21]

The probe bias is swept by the triggered circuit shown in Fig. 4-4. The voltage and current are recorded on a Nicolet Explorer Digital Oscilliscope and transferred to a Modcomp mainframe computer. The electron current (I_e) is found by subtracting the plasma ion and beam ion currents from the total probe current. The electron temperature is determined from the transition region slope of such an electron current characteristic (see Fig. 4-3c). The plasma potential, V_p, is determined from the inflection point of the electron current characteristic. The second derivative (see Fig. 4-3b) is calculated by use of fast Fourier transforms, and the inflection point is then taken as the zero of this second derivative.

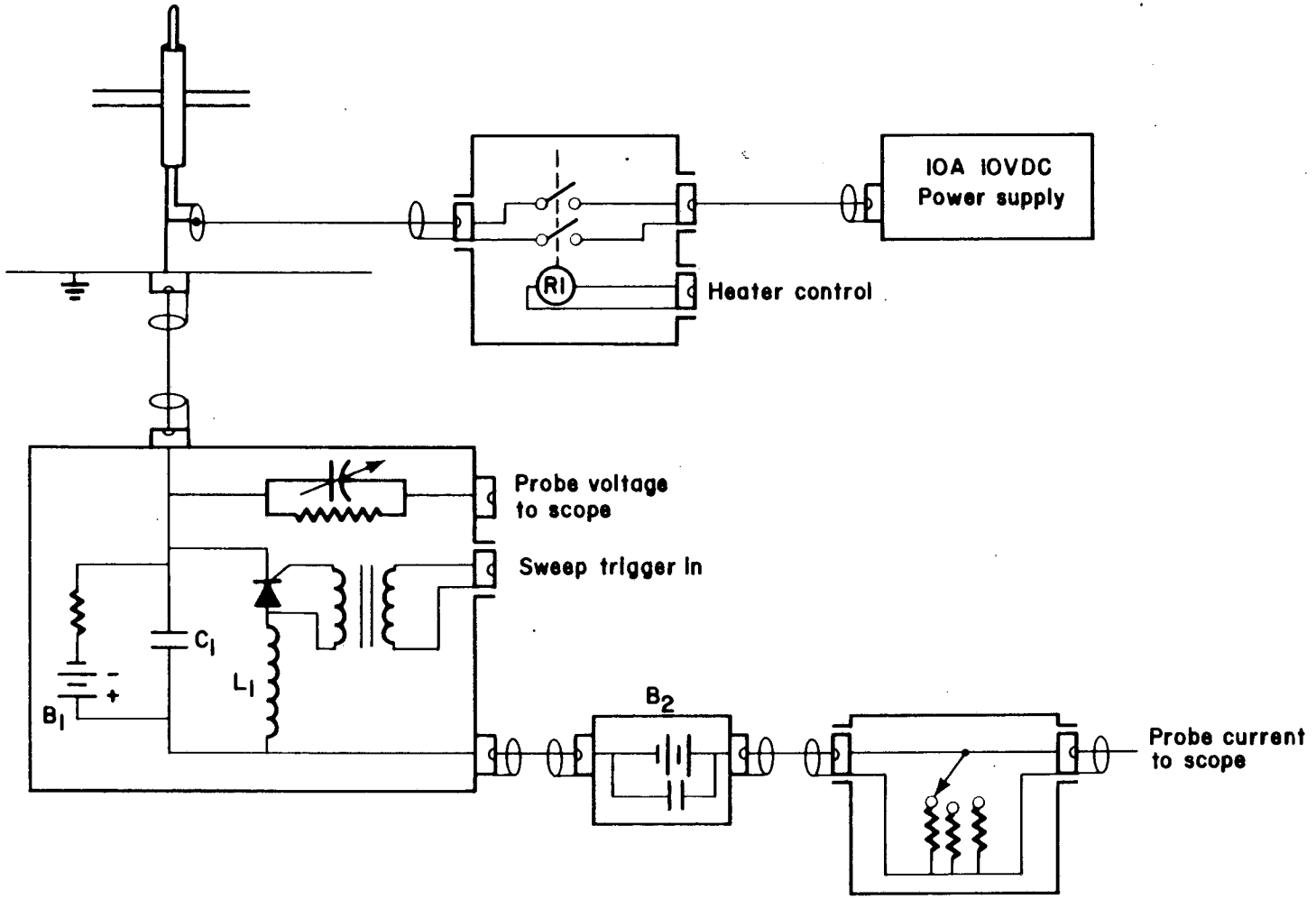

Fig. 4-4 Langmuir Probe Circuit Schematic.

XBL 823-300

The electron density in the orbital-motion-limited (thick sheath) case can be inferred from a fit to the current in the electron saturation region, which satisfies,

$$I_e = \sqrt{\frac{2}{m_e}} \quad \frac{A_{probe}\, n_e\, e}{\pi} \quad \sqrt{V - V_p + T_e} \qquad (V-V_p) >> T_e \quad ,$$

where A_{probe} is the probe surface area.[21] This has been done in previous work on this neutralizer,[1] but is not used here. We find that electron densities inferred from the electron current at V_p agree within 10-20% of those inferred from the saturation region fits to the same current characteristic. We find the electron density with

$$n_e = \sqrt{\frac{2\pi\, m_e}{T_e}} \quad \frac{I_p}{A_{probe}} \quad ,$$

where I_p is the electron current when the probe is biased at V_p.[21]

2. Beam Dump Calorimeter

The beam divergence was determined from Gaussian fits to the response of a 4 by 8 array of thermistors buried in the beam dump calorimeter at z = 3 m. The beam dump calorimeter is shown in Fig. 4-1. The size of the beam dump limits its useful range to beam divergence of less than 10 deg. Additionally, the neutralizer collimates parts of the beam to less than 6 deg. For divergence greater than this, the beam dump is only useful as a relative measure. Its advantage lies in its ability to determine beam divergence on a shot-by-shot basis.

3. Moveable Calorimeter for Beam Profiles

To determine the radial profile of the beam at z = 30 cm, we employed a simple thermocouple to measure beam power deposition. A pair of copper and constantin wires (the thermocouple) was sandwiched together by folding over one end of the 0.010-in. thick 0.25-cm^2 copper sheet (see Fig. 4-5). This calorimeter was then inserted at z = 30 cm to intercept the beam at the radial position of interest. The sensitivity is set by the sheet thickness, and time-integrated beam power deposition is recorded as the temperature rise of the thermocouple. The cooling time for the package depends upon the thermal mass of the sheet and the diameter and length of the copper wire that was mechanically attached to the 0.25-in. copper tube used to insert the thermocouple into the neutralizer.

This diagnostic is sensitive to the beam halo, which may miss the beam dump, and therefore gives more complete and accurate information about the beam divergence than the beam dump at large angles. However, data aquisition requires one beam pulse (shot) for each radial position.

4. Fast Ion Gauge

Neutral pressure is measured by use of an ionization gauge, driven with a fast feedback loop in the D.C. filament circuit that keeps electron emission constant. The time response of this gauge is slowed to ~10 ms by the right-angle tube and fine wire mesh hiding it from the plasma electrons. This presents no difficulty for us, since the gas pulse has reached steady state by 20 ms and the beam is turned on

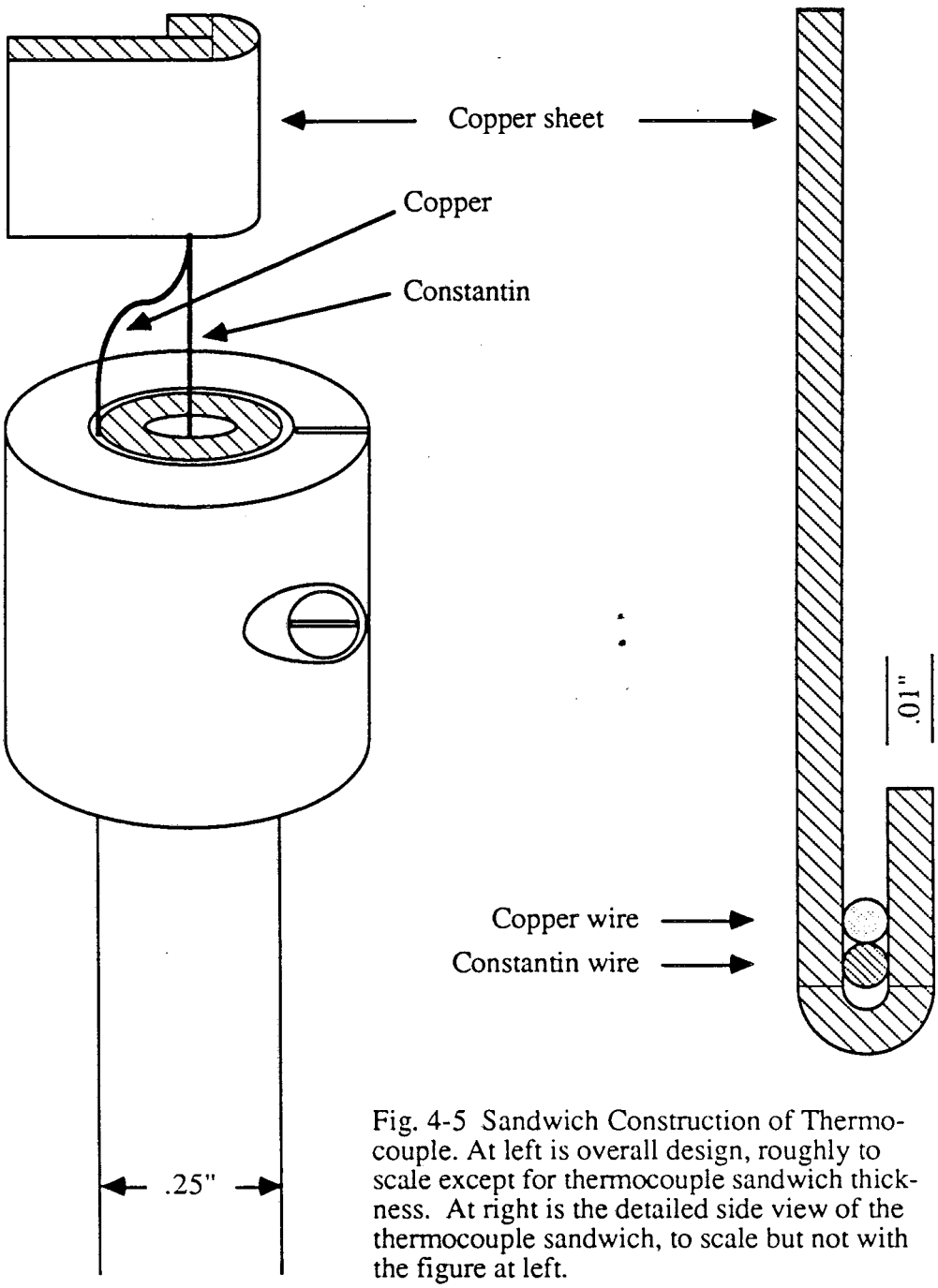

Fig. 4-5 Sandwich Construction of Thermocouple. At left is overall design, roughly to scale except for thermocouple sandwich thickness. At right is the detailed side view of the thermocouple sandwich, to scale but not with the figure at left.

200 ms later. We are not in a position to report evolution of the gas pressure during the beam pulse itself, as, despite our efforts, the ion collector current responded to the presence of the beam and the neutralizer plasma.

5. Electrostatic Fluctuation Probe

In Fig. 4-6 and Fig. 4-7 we show the probe employed to detect electrostatic plasma oscillations. As our plasma frequency is quite high (2-3 GHz), the 1 cm^2 area circular disk probe was mounted directly to the center conductor of a short piece (20 cm) of 0.141-in. o.d. copper clad, semi-rigid, 50 Ω co-ax. This was connected to double-shielded 50-Ω flexible co-ax. After passing through an impedance-matched D.C. block, the signal enters an H.P. 8441A Preselector (see Fig. 4-7). The preselector is a swept bandpass filter, driven by the spectrum analyzer, which only passes frequencies on the selected band of the spectrum analyzer. The signal is then terminated in the 50 Ω input of the H.P. 8551B Spectrum Analyzer. The spectrum analyzer is composed of a sweep oscillator, mixer, and detector. The input signal is mixed with the sweep oscillator and observed at the detector. Many harmonics of the sweep oscillator are present at the mixer, allowing a number of frequency bands to be detected with one sweep oscillator. This poses a problem for a broadband signal - it is impossible to determine which harmonic of the sweep oscillator has mixed with the input signal to arrive at the detector. Use of the preselector to predetermine the band of the input signal avoids this pitfall.

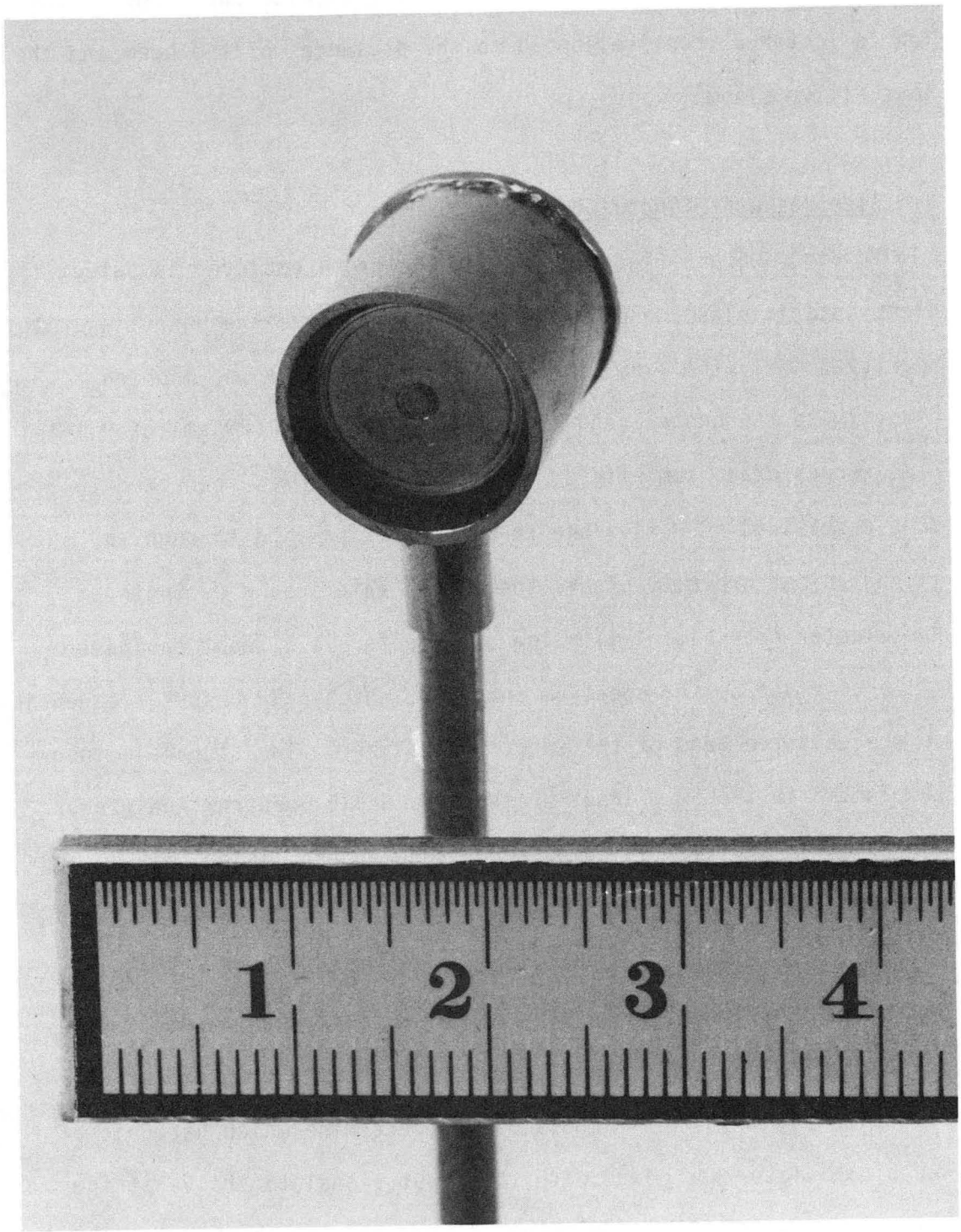

XBB 860-8600

Fig. 4-6 Electrostatic Fluctuation Probe. Ruler unit is cm.

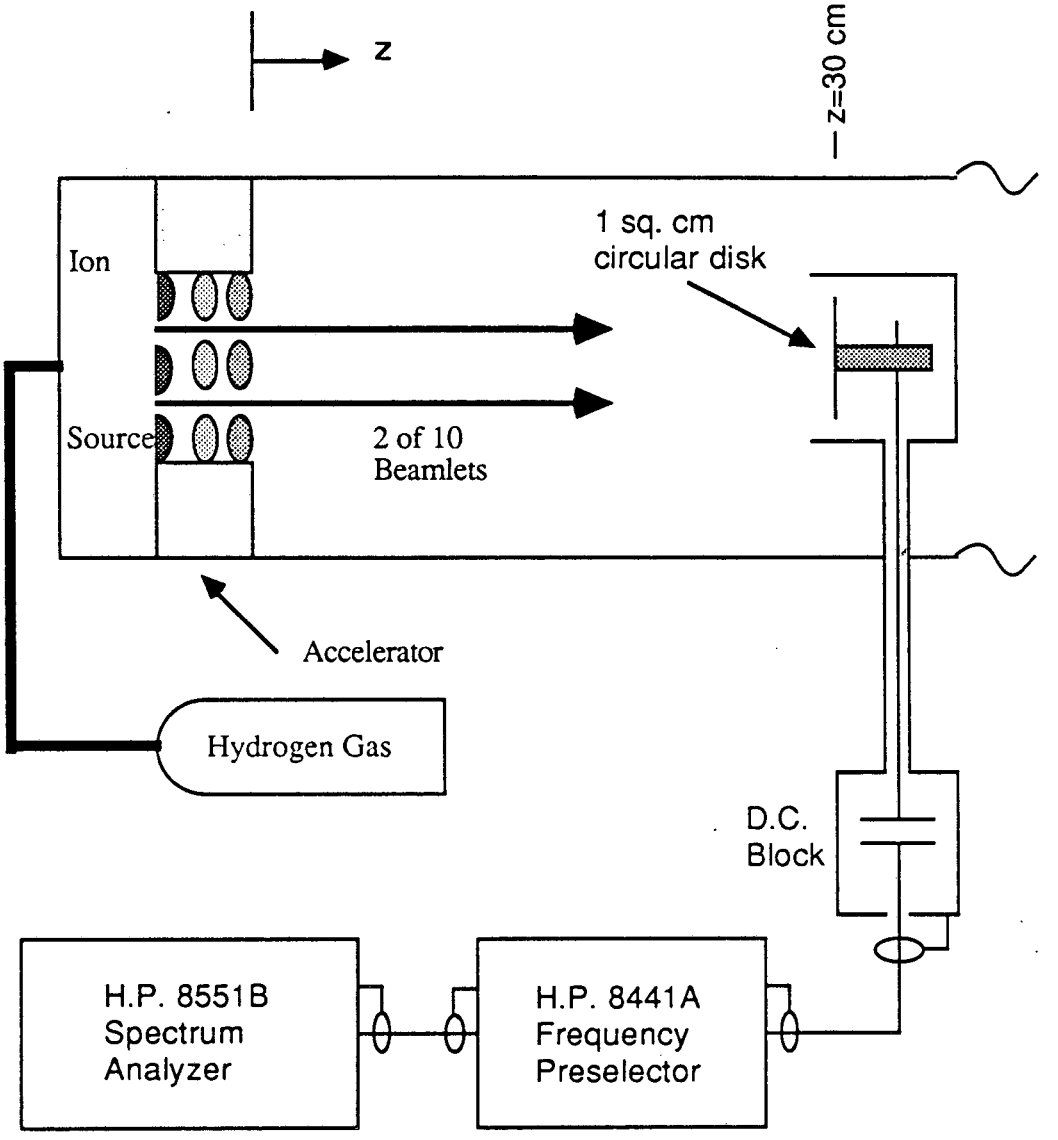

Fig. 4-7 Schematic of Electrons Used to Detect Electrostatic Oscillations. A photo of the circular probe itself is shown in Fig. 4-6. The probe is drawn nearly to scale within itself, but not to scale with the rest of the drawing.

E. Beam Manipulations

1. Beam Interceptor

To determine the effect of beam-induced secondary electron emission from the radial wall, we added a controllable extension of the wall (see Fig. 4-8). A rod inserted through the z = 60 cm port enabled a deflection of the 7.5 by 20 cm stainless steel beam interceptor into the beam path.

2. Beam Collimator

Also shown in Fig. 4-8 is a series of four round copper plates arranged in pairs, forming a beam collimator. Each of the plates has a 5 cm beam aperture in the center and an array of gas flow holes elsewhere. These latter were aligned azimuthally so that each pair of plates would allow gas transport outside the beam aperature, but would block the beam. The nominal axial positions of the two pair of plates were 11 and 24 cm.

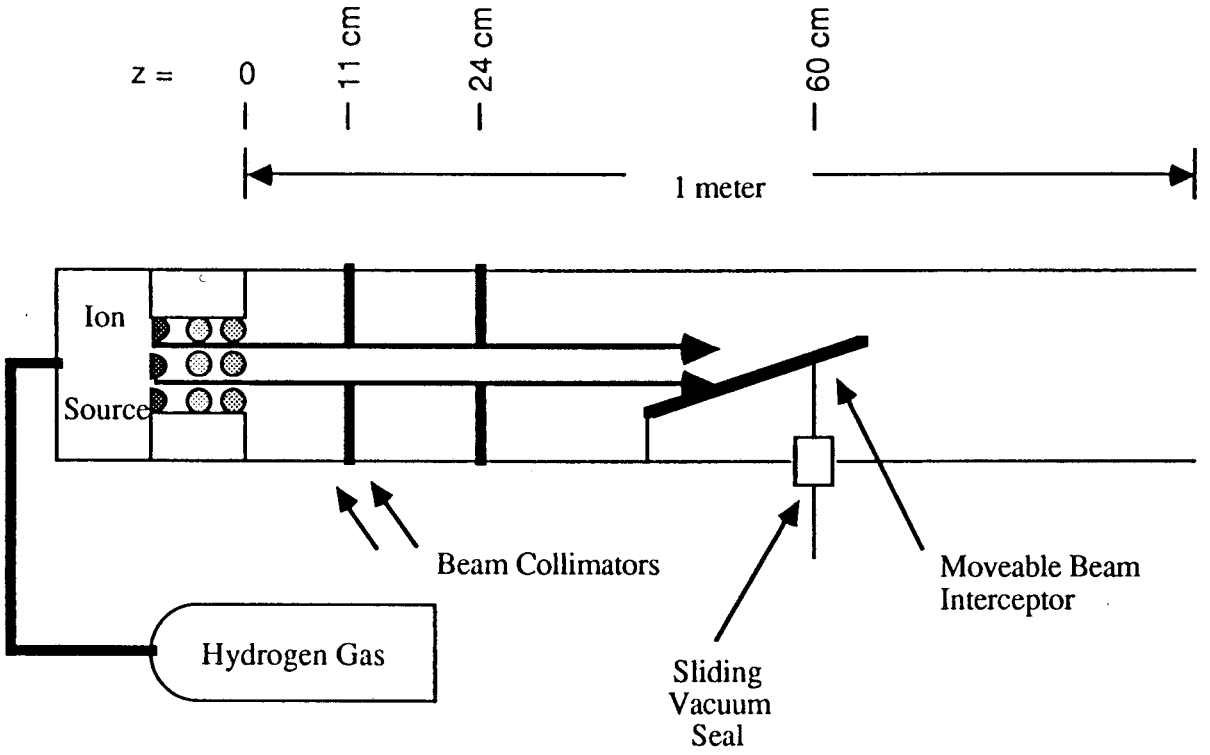

Fig. 4-8 Beamline Schematic Showing Locations of Beam Collimator and Beam Interceptor

Chapter 5

Experimental Results and Discussion

A. Collisional Balance

1. Numerical Integration

To evaluate the power terms, we numerically integrate eq.'s 2.3, 2.5, 2.6, and 2.9. This procedure is detailed further in Appendix C. Here we simply report the numerical results for the case of E_b = 25 kV, I_b = 5.1 A, species mix 60:25:15 of H^+: H_2^+: H_3^+, and for the following quantities measured at z=30 cm: p_{gas} = 2.7 mTorr, $n_e = 1.1 \cdot 10^{11}/cm^3$, ϕ_p = 15 V, and T_e = 1.8 V. We find

$$P_{Tr} = 6.0 \cdot 10^{20} \text{ V/sec} \tag{5.1}$$

$$P_{inel} = 2.6 \cdot 10^{20} \text{ V/sec} \tag{5.2}$$

$$P_{K.E.} = 1.3 \cdot 10^{20} \text{ V/sec} \tag{5.3}$$

$$P_{Coul} = 3.0 \cdot 10^{20} \text{ V/sec} \tag{5.4}$$

Remember our convention is that of energy expressed in units of potential, suppressing the electronic charge. If the collisional model were adequate to describe the power balance, P_{anom} of Eq. 2.11 would be zero. Instead we find

$$P_{anom} = (6.0 + 2.6 + 1.3 - 3.0) \cdot 10^{20} \text{ V/sec}$$
$$= 6.9 \cdot 10^{20} \text{ V/sec} \tag{5.5}$$

Since P_{anom} is of the same order as the terms that should be balancing, we conclude the collisional model is inadequate.

2. Gas Dependence of T_e

The inelastic loss term, Eq. 5.2, is comparable in size to the other terms. Thus we might expect to see some variation of T_e with n_g

in accordance with Eq. 2.22; $T_e^{3/2} = g_{15} + g_{16}\sqrt{T_e} - g_{17}\Gamma(T_e)n_g$, the last term representing the cooling by inelastic electron collisions with the neutral gas. In Fig. 5-1 we show T_e data taken at two gas pressures plotted against I_b. Also shown is a third set of points taken while using He gas in the neutralizer. Helium is a particularly interesting neutralizer target because of the high energy (19.8 V) of its first excitation level. For our conditions (T_e < 2 V) with a He target, the inelastic electron-energy loss rate, $\Gamma(T_e)$, would be vanishingly small. Therefore P_{inel} would not contribute to the energy balance; the last term in Eq. 2.22 would vanish. The data in Fig. 5-1 thus provide a test of the inelastic energy loss term in the energy balance.

As can be seen from Fig. 5-1, there is no significant dependence of the peak T_e (the low temperature data will be discussed in Sec. C.1 of this Chapter) on pressure or target species. For a quantitative assessment, consider T_e at I_b = 6.6 A for both H_2 pressures. If the 1.7 mT data were to satisfy the collisional balance of Eq. 2.10, then we could use the scaling (of T_e and n_g) relation (Eq. 2.22) to find T_e at I_b = 6.6 A for p_g = 2.8 mT. The third term on the RHS of Eq. 2.22 is the term most rapidly varying with T_e (see Fig. 2-2) and also the only term with n_g dependence. On Fig. 5-1 we see that T_e for the 1.7 mT case is 1.75 V, and T_e for 2.8 mT is very close at 1.68 V. To determine if this very slight change of T_e is consistent with Eq. 2.22, we take as constants the first two terms on the RHS as well as the LHS of Eq. 2.22. There is no treachery here - each of the terms in Eq. 2.22 is of the same order (unity), as evidenced by

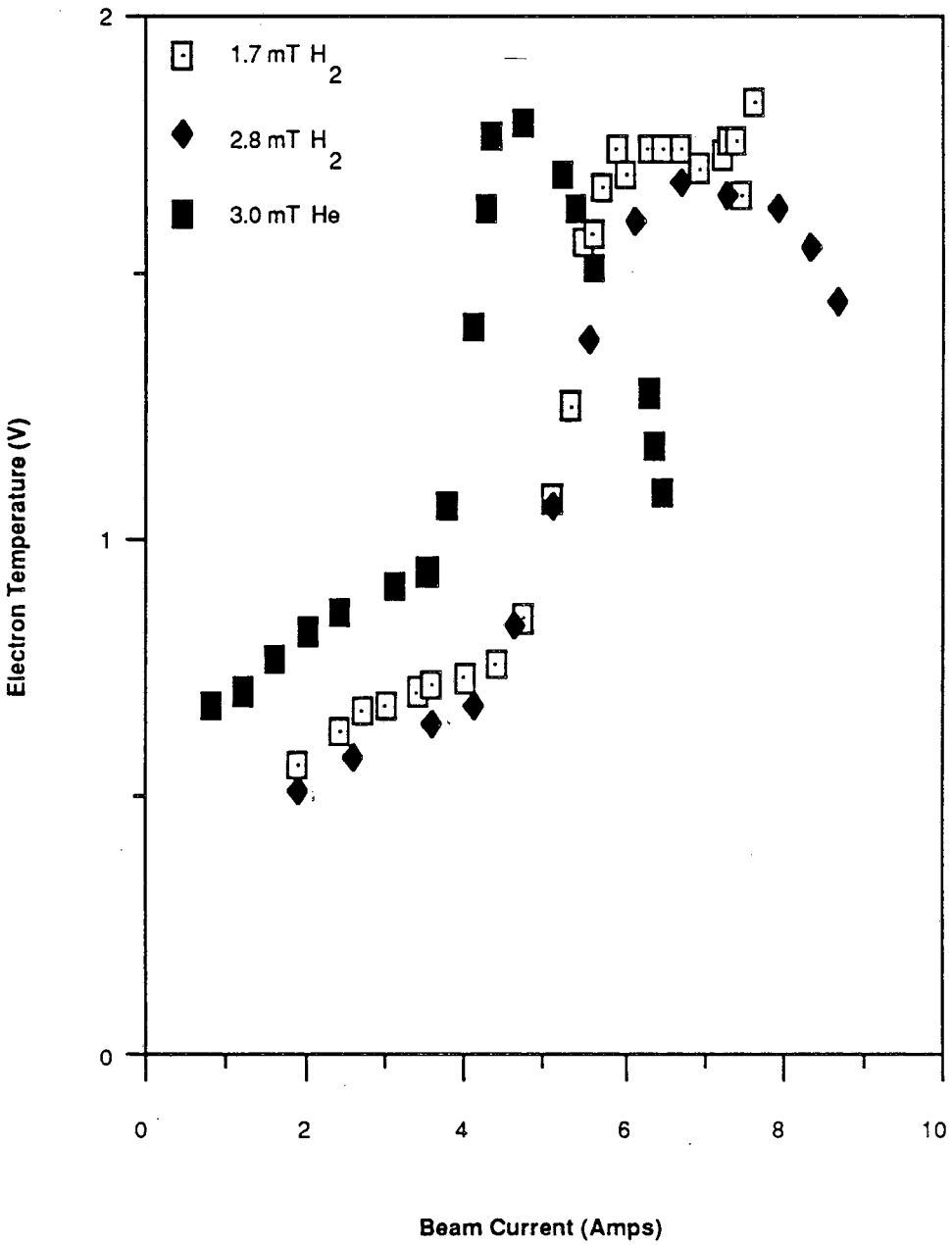

Fig. 5-1 Dependence of Electron Temperature Upon Gas Pressure and Gas Chemistry. The electron temperature is plotted versus current for a neutralizer comprised of Hydrogen gas of pressure 1.7 mTorr and 2.8 mTorr, and Helium gas of pressure 3.0 mTorr. Gas pressure and electron temperature are measured at the 30 cm axial position. Beam energy is 25 kV.

eq.'s 5.1 - 5.4. The order of the relative change in T_e according to Eq. 2.22 can therefore be taken as that of the LHS

$$\Delta = 3/2\ \Delta T_e/T_e = 6\% \quad .$$

Then if $T_e(2.8\ mT)$ is to follow the n_g dependence of Eq. 2.22, the third term on the RHS Eq. 2.22 must also be constant (to order 10%):

$$\Gamma(T_e(2.8\ mT)) \cdot n_g\ (2.8\ mT) = \Gamma(1.75\ V) \cdot n_g(1.7\ mT)$$

$$\text{or } \Gamma(T_e(2.8\ mT)) = \frac{1.7}{2.8} \cdot 1.8 \cdot 10^{-9}\ V\ cm^3/sec$$

$$= 1.1 \cdot 10^{-9}\ V\ cm^3/sec$$

We see from Table 2-1 that this requires $T_e(2.8\ mT) = 1.25$ V, not the 1.68 V observed. We have performed this evaluation for the data shown in Fig. 5-1. This behavior is very reproducible. For this accelerator configuration, with p_g = 1.7 amd 2.8 mT, we observed $T_e(I_b = 6.6\ A) = 1.74 \pm 0.06$ V and 1.68 ± 0.06 V, respectively. The error reported is the standard deviation of the data body for p_g = 1.7 mTorr and is not intended to include any systematic error, which is certainly larger. There were only two data sets for p_g = 2.8 mTorr, so the error for that body of data is presumed to be the same as the 1.7 mTorr body of data. The calculation above [that T_e(6.6 A, 2,8 mT) = 1.25 V] is well beyond the range of our experimental data. We are forced to conclude that the pressure dependence predicted by the collisional model is not obeyed by these peak electron temperatures.

There is one way in which the above arguments could be incorrect - if the inelastic cooling term was much smaller than calculated and therefore not a significant term in the energy balance. This would be the case if the tail of the electron distribution was depressed to a level significantly below that of a Maxwellian, as one might expect of

electrons trapped in a potential well.[22] The depression (or truncation) of the tail occurs only for electron energies > ϕ_p, which for the calculations of eqs. 5.1-5.4 was ≃ 15 V. For T_e < 2 V, only two terms contribute to $\Gamma(T_e)$ - excitation of the first vibrational level of H_2 and dissociation of H_2, for which the cross sections peak at 4 and 15 V, respectively. With a 2-V distribution truncated (the extreme case) at 15 V, we would not expect Γ to deviate much from that calculated for a Maxwellian.

In fact, looking at a typical electron current versus voltage characteristic (after subtraction of ion current) (Fig. 5-2) taken at z = 30 cm, one might think our calculation of P_{inel} would be significantly underestimated, since the electron distribution is apparently bi-Maxwellian. Bi-Maxwellian least square fits to the data typically have a hot "tail temperature" of 10-15 V. Recall from Eq. 2.2b that the nascent (newly created) electrons, with characteristic energy 11.4 V, do not thermalize with the trapped electrons. Certainly the electrons excite the neutralizer gas at a higher rate than that calculated for a Maxwellian electron distribution, but we are concerned here with the power balance - and the only inelastic energy loss that contributes to the power balance is that of the trapped electron distribution. The higher temperature electrons in the tail extract much less power from the beam by Coulomb collisions than do the trapped electrons - owing to their higher "thermal" velocity ($v_{hot\text{-}tail} \simeq v_b$) and lower density ($n_{tail}/n_e$ < 10%) - and the hot-tail electrons certainly do not cool the trapped electrons. The hot-tail electrons were <u>born</u> with any energy they lose to the

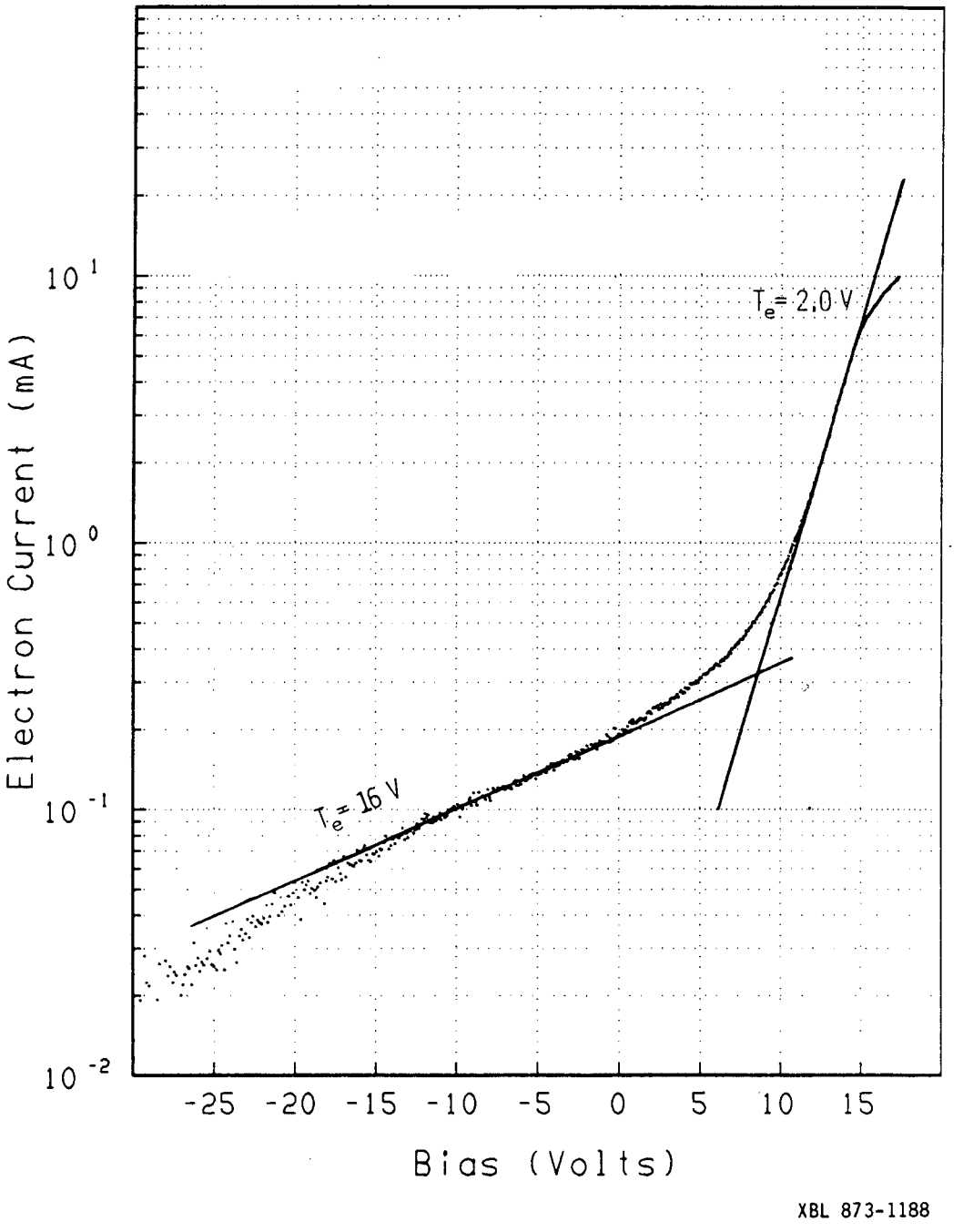

Fig. 5-2 Electron Current Characteristic. Ion current has been subtracted from the probe current. E_b = 34 kV and p_g = 1.7 mT at z=30 cm. Data inferred from this trace: T_e = 2.0 V, $n_e = 3.7 \cdot 10^{10}$ cm^{-3}, T_{tail} = 16 V, $n_{tail} = 1 \cdot 10^{9}$ cm^{-3}.

gas. Thus, in evaluation of $\Gamma(T_e)$, the use of the low temperature Maxwellian distribution is appropriate for the power balance.

3. Beam Energy Dependence of T_e

We found in Eq. 2.21 that for optimum I_b ($I_{opt} \propto E_b^{3/2}$) and n_g fixed, T_e varies no faster than with $\sqrt{E_b}$. This is in striking contrast to the dependence we observe, $T_e \propto E_b$, as seen in Fig. 5-3, where we have plotted T_e observed at optimum I_b versus E_b. The near linear relationship between T_e and E_b does not conform to the collisional power balance.

4. Beam Current Dependence of T_e

One could characterize the behavior of T_e with I_b in Fig. 5-1 as beginning with a linear relationship, followed by a rapid climb to a plateau (referred to as jump behavior). We shall consider these two regions separately.

a. Linear Behavior

For $I_b < 4.5$ A (25 kV, H_2 data), we see from Fig. 5-1 that T_e is approximately linear with I_b. From Eq. 2.19, we expect a slower variation:

$$T_e = (g_{10})^{2/3}(I_b + g_{12})^{2/3}. \qquad (2.19)$$

In fact the data for H_e and 1.7 mT H_2 in Fig. 5-1 can be fit acceptably to either power (2/3 or 1). This is because the T_e intercept at $I_b = 0$ is relatively large (0.4-0.6 V), making Eq. 2.19 fairly flat. In Appendix D, we evaluate both g_{10} and dT_e/dI_b for the

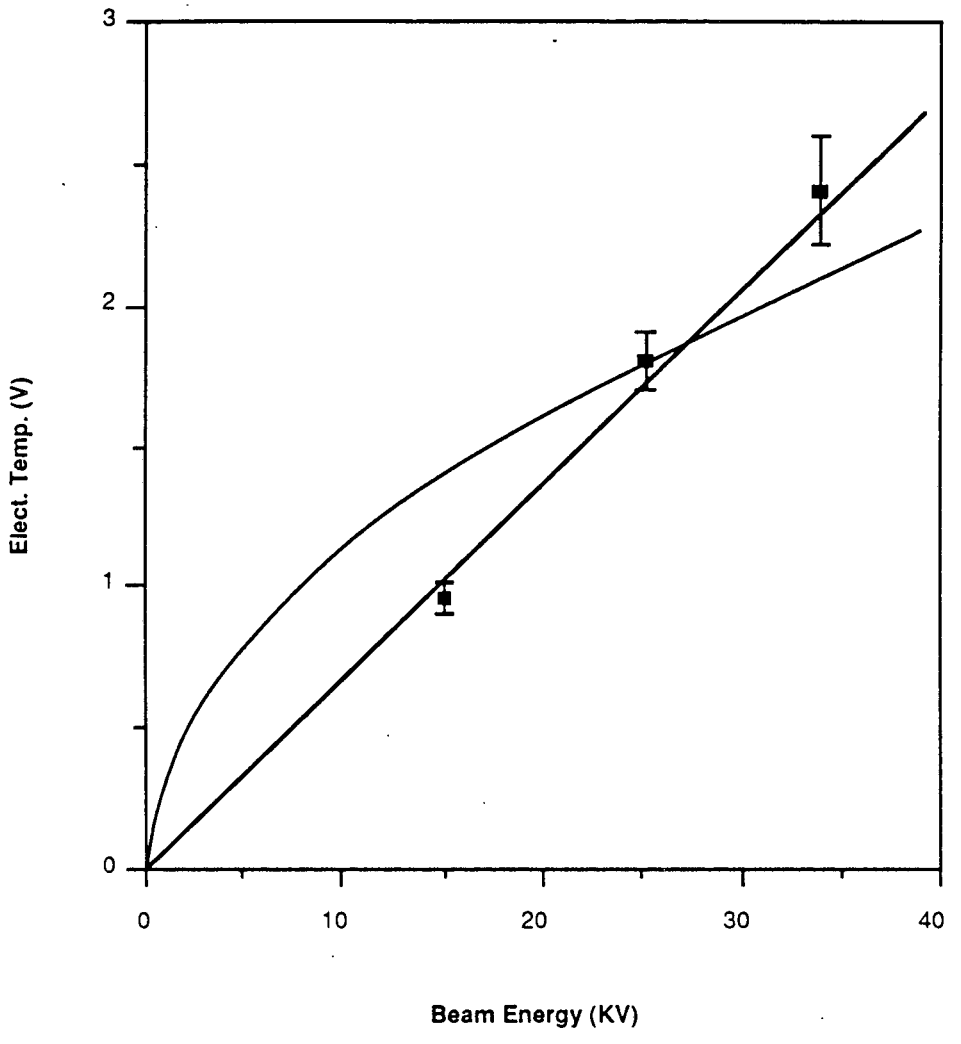

Fig. 5-3 Peak Electron Temperatures as a Function of Beam Energy. Error bars reflect the scatter of peak temperatures observed for a variety of operating conditions : various gas pressures and species and accelerator gap width (or accelerator perveance). The straight line represents 0.07 V / kV. The curve indicates the square root energy dependence that would match the electron temperature at a beam energy of 25 kV.

system parameters pertaining to the data in Fig. 5-4 (1.7 mT data of Fig. 5-1): $g_{10} = 0.08\ V^{3/2}/Amp$ and $dT_e/dI_b = 0.06$ V/Amp. A least squares fit of Eq. 2.19 to the data of Fig. 5-4a is

$$(T_e)^{3/2} = (0.09 \pm 0.01)\ V^{3/2}\ I_b/Amp + (0.28 \pm 0.03)\ V^{3/2} \qquad (5.6)$$

This is in excellent agreement with g_{10}. Similarly (but easier to visualize from Fig. 5-4a) the best linear fit to the data of Fig. 5-4a has a slope of 0.07 ± 0.01 V/Amp. This degree of agreement is fortuitous, as we assumed axial uniformity while performing the spatial integrals to derive the beam current dependence - and here we are comparing a measured beam current dependence of electron temperature to the dependence calculated from the data of a single z axis point (z = 30 cm) in a system which is not axially uniform. The good fortune comes about because the spatial average of the power balance terms is equal to that which would be given by local terms somewhere between z=20 and z=30 cm.

Although this section is devoted to the dependence of T_e upon I_b (not gas species), we note significant difference between the He and H_2 data of Fig. 5-1; specifically the T_e intercept is higher for He. This is consistent with the collisional model, as both g_{12} in Eq. 2.19 and g_7 in Eq. 2.18 include the ionization potential, ϕ_i, of the target molecules or atoms. If we ignore the $\Gamma(T_e)$ term in Eq. 2.18, just as we did to derive Eq. 2.19, we readily find the T_e intercept to be $T_e(I_b=0) = g_7 \sqrt{E_b}$. Also $g_7 \propto \sqrt{\phi_i}$, so that

$$T_e(I_b = 0) \propto \sqrt{\phi_i} \qquad (5.7)$$

a)

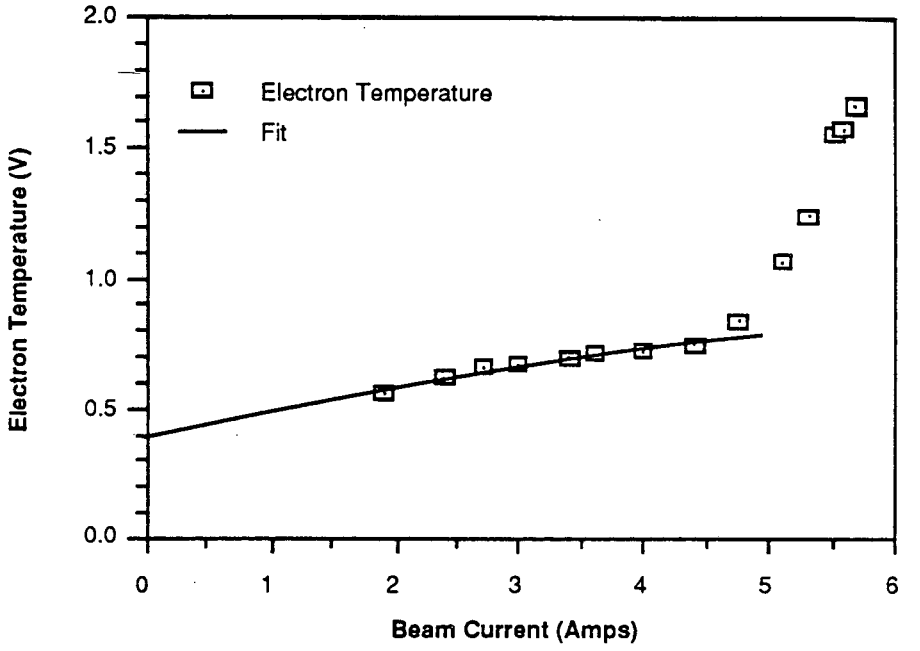

b)

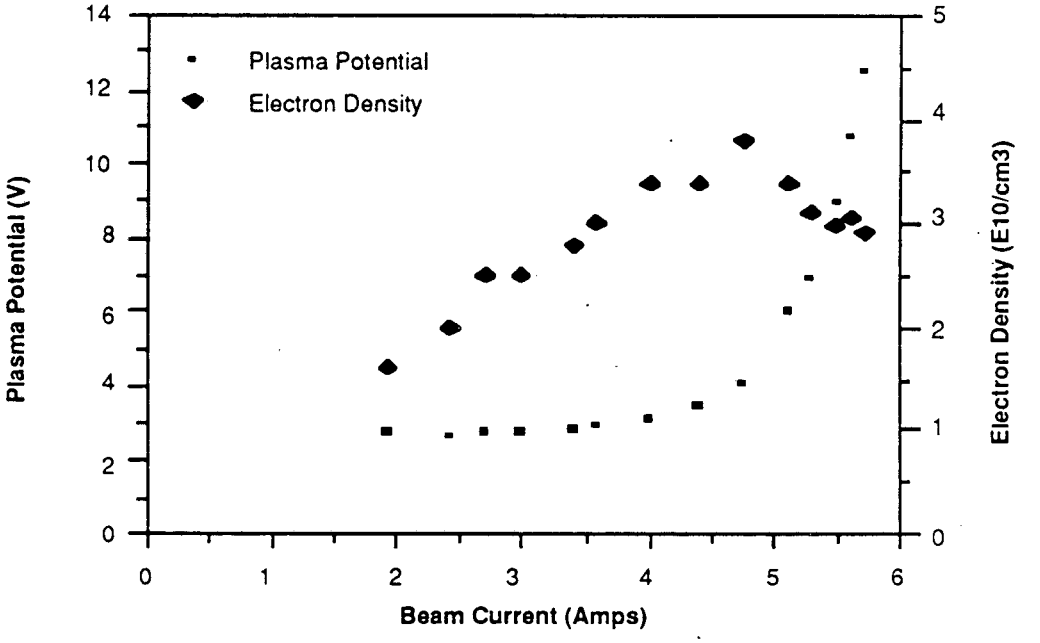

Fig. 5-4 a) Electron Temperature Plotted Versus Beam Current. Data is for beam energy = 25kV, hydrogen gas pressure = 1.7 mTorr. Line drawn is a least squares fit of Eq. 2.19 to the data. b) Plasma Potential and Electron Density Versus Beam Current.

The best fits of the He and 1.7 mT H_2 data of Fig. 5-1 to Eq. 2.19 have T_e intercepts of 0.60 $\pm$ 0.03 V and 0.43 $\pm$ 0.03 V, respectively. These are just within a standard deviation of one another, when the latter is scaled by $\sqrt{\frac{\phi_i(He)}{\phi_i(H_2)}} = 1.25$.

Note that there is a slight difference in T_e between the two pressures of H_2, with the lower pressure having a higher T_e intercept. This would suggest that the $\Gamma(T_e)$ term neglected in Eq. 2.19 is not completely negligible, even at these low temperatures. In fact we can make a simple estimate of the $\Gamma(T_e)$ term in Eq. 2.18 by comparing the T_e intercepts of the 2.8 mT and 1.7 mT data, as the 2.8 mT data has an $\Gamma(T_e)$ contribution to Eq. 2.18 that is 2.8/1.7 times larger than that for the 1.7 mT data. From Fig. 5-1, we see a change in T_e of .08 V between the two H_2 pressures. This means that for the 1.7 mT data, the Γ term in Eq. 2.18 is $\frac{1.7 \cdot .08\ V}{2.8 - 1.7} = 0.12$ V. This is comparable to, but smaller than the effect of ϕ_i on T_e discussed above.

Clearly, since the He data would have no such loss term, we must expect an increase of order 0.1 V over the 1.7 mT H_2 data. When we add 0.1 V to the T_e intercept of the 1.7 mT data and then scale that number by 1.25 for the ionization potentials, we are still in agreement with the He data by barely a standard deviation, although at the opposite extreme of the limits.

We see that for I_b below the "threshold", the collisional model provides the correct T_e dependence upon beam current and predicts the effect of gas pressure and type on T_e as well. A numerical evaluation such as that of Eq. 5.5 is meaningless in this case - to make the

power balance numerically integrable, we assumed axial uniformity of the radial beam profile. This is not the case for I_b below "threshold", which we shall show corresponds to the optimum beam current (I_{opt}) for the accelerator. We shall discuss the optimum beam current in more detail later; for now we assert that for I_b below this optimum current, the beam is diverging. In other words, the radial beam profile is spreading as the beam travels down the neutralizer and our numerical integration is not valid for I_b below I_{opt}. Below optimum, the observed dependence of T_e upon I_b, gas pressure, and gas species provide the best clue that the energy balance is described by the collisional model of Chapter 2.

b. Jump Behavior

i. Beam Divergence Below I_{opt}

In positive ion accelerators such as we use, as I_b is varied while holding E_b fixed, the edge of the source plasma moves to accommodate the current density required, according to the Child-Langmuir Law[23]

$$J_b = \frac{4}{9}\sqrt{\frac{2e}{m_b}}\ \frac{E_b^{3/2}}{d^2}\ , \qquad (5.8)$$

where d is the distance from the accelerating electrode to the source plasma sheath.

In the Berkeley 10-Amp, 40-kV accelerator, sheath position has a strong effect on the beam divergence.[24] This is because sheath position affects sheath curvature. In Fig. 5-5 we sketch the sheath location at optimum j_b and at j_b below optimum (heavy line). In the first few millimeters of flight, ions in the case of j_b below optimum can achieve a substantial velocity perpendicular to the beam

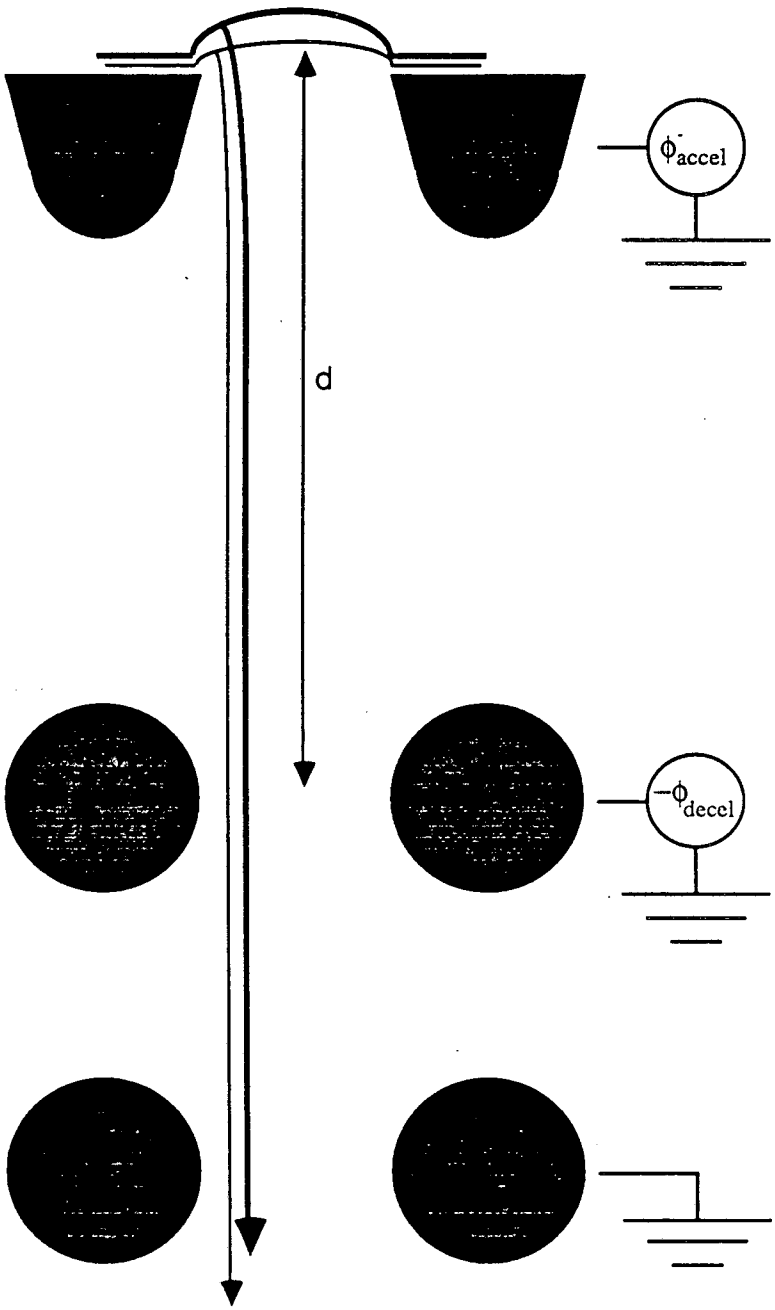

Fig. 5-5 Ion Trajectories in the Accelerator. Solid objects are the accelerator electrodes viewed end-on. The heavy line sketches the plasma sheath position and one particular ion path for the case of beam current below optimum - the thin line is same, but for optimum beam current density. Notice that ion emission perpendicular to the plasma surface gives the ion a larger component of perpendicular velocity for beam current density below optimum than for optimum beam current density. The middle electrode repels electrons from the neutralizer plasma. The total potential drop across the sheath (of thickness d) is $\phi_{accel} + \phi_{decel}$.

direction. This causes a significant beam divergence (> 10 deg) unless I_b is within an Amp of I_{opt}.

ii. Effect of Beam Divergence Upon the Collisional Model

The divergent beam at I_b below optimum does provide two possible explanations within the framework of the collisional model for the jump-like behavior of T_e with T_b. A diverging beam will strike the wall of the neutralizer, producing secondary electrons. Such an electron is born with just enough energy to make it back to the wall. If, however, it suffers any deflection, as a result of a collision or a collective fluctuation, it will be trapped in the potential well, and then requires an energy input (of at least T_e) to escape. The power loss of these secondary electrons would be a term similar to Eq. 2.6,

$$P_{sec} = \gamma_{sec} T_e I_b(wall) \qquad (5.9)$$

where γ_{sec} is the secondary emission coefficient and $I_b(wall)$ is the total beam current striking the neutralizer wall. Secondary electrons from the wall are a cooling mechanism. One could argue that by operating below optimum current for the accelerator, we depress the electron temperature by adding these wall electrons and that a jump in T_e occurs when the source of wall electrons is eliminated, which happens when I_b reaches optimum. To determine if this effect was responsible for the jump in T_e near optimum I_b, we installed in the neutralizer a large area (100 cm^2) plate that could be moved into or out of the path of the beam. When the plate intercepts the beam, there will always be a source of secondary electrons (comparable to

that from the wall below optimum I_b) for any beam current. The jump behavior was unchanged by this interception. We conclude that cool wall electrons do not cause the jump behavior.

The second possible explanation is that when the beam is divergent, ions are produced nearer to the walls than when I_b is at optimum, reducing the ion lifetime and flattening the density profile in such a way as to reduce the power transfer from beam ions to electrons by Coulomb collisions. Again, this would be a tuning effect, depressing the electron temperature when operating below optimum I_b. Two collimator plates were installed at z = 11 and z = 24 cm to ensure that ion production would be restricted to a cylindrical area smaller (5 cm diameter) than the original beam size. Jump behavior of T_e was also observed when the beam was so collimated. Apparently there are no spatial effects that act to produce this jump. The jump behavior of T_e with I_b cannot be explained within the framework of the collisional model.

This jump behavior is associated with the approach of I_b to optimum current for the accelerator, as opposed to a threshold in beam current density. The accelerator electrode spacing was changed twice, so that we were able to operate at three optimum currents for any given E_b, encompassing a variation of 50% I_b. In every case, the jump begins when the beam angular divergence drops below $\theta \simeq 8$-10 deg. (1/e width), as measured by the calorimeter 3 meters from the accelerator, and typically flattens out when the beam divergence reaches a minimum (see Fig. 5-6). Examples of T_e dependence upon I_b, for two different accelerator gaps are shown in Fig. 5-7. Note

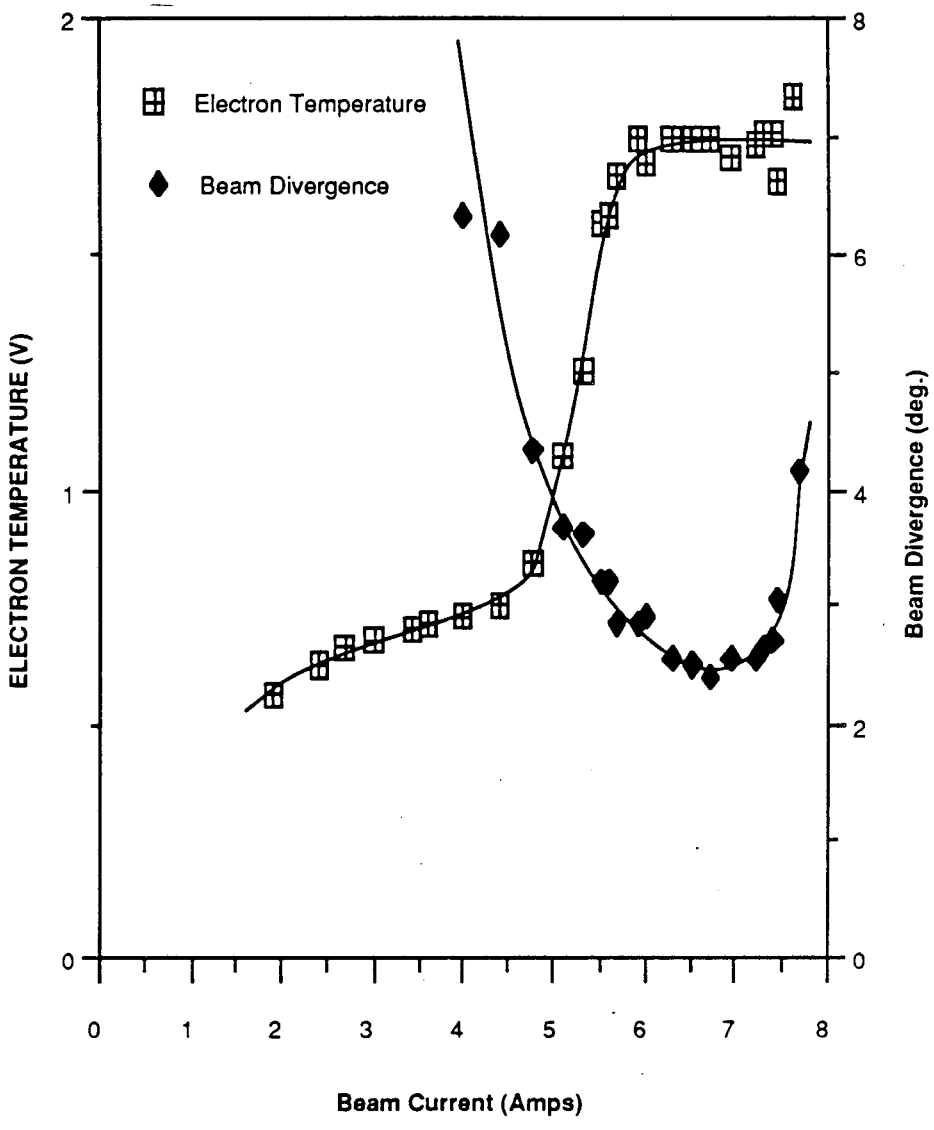

Fig. 5-6 Electron Temperature and Beam Divergence Versus Beam Current. Electron temperature data is the 1.7 mTorr data from Fig. 5-1. Beam energy is 25 kV. The curves are drawn to guide the reader and to indicate that the beam divergence continues to increase as I_b is decreased beyond the beginning of plotted data.

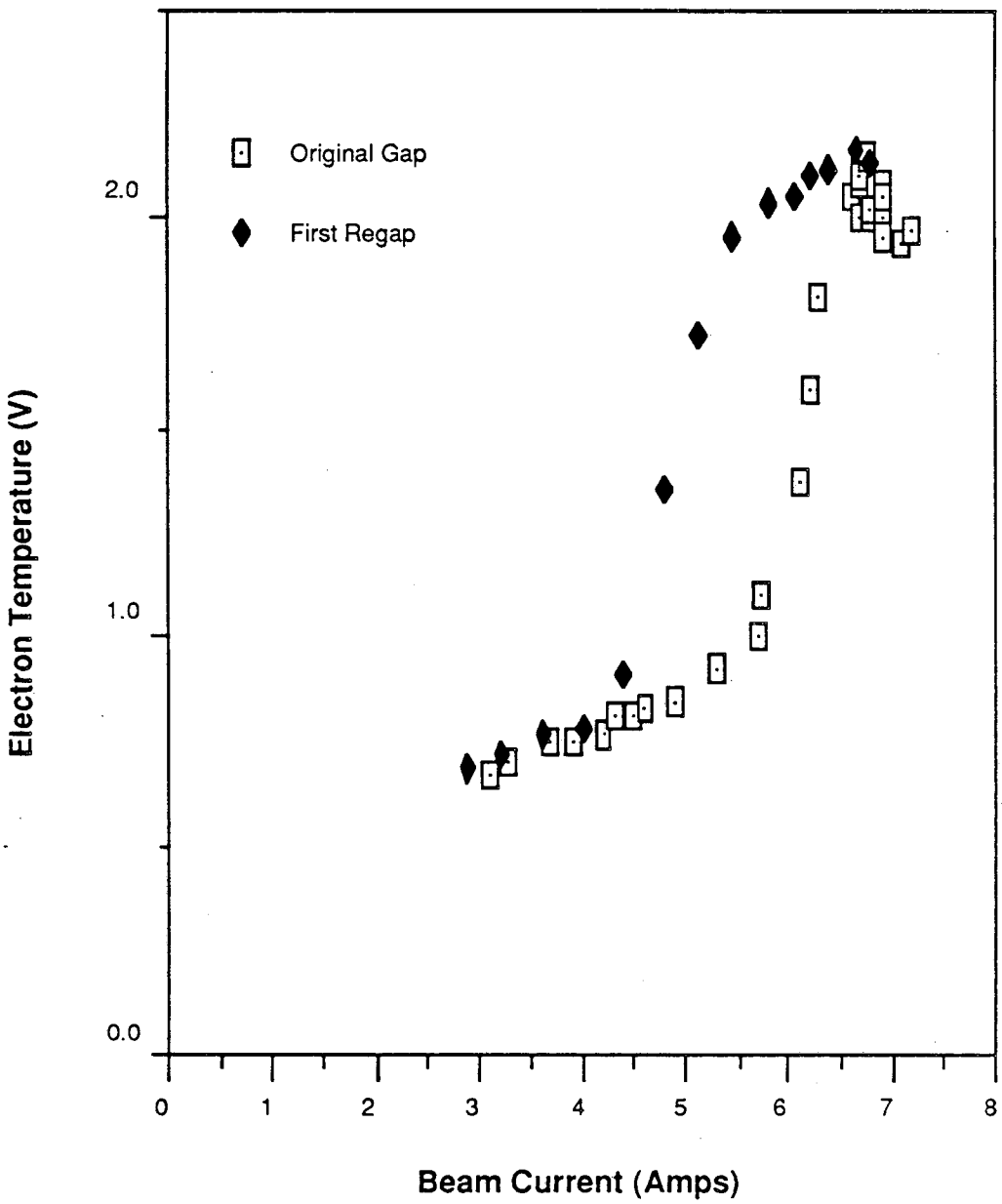

Fig. 5-7 Effect of Operating the Accelerator at Different Electrode Separations. Electron temperature in both cases is plotted for the same conditions with the exception of accelerator electrode separation. The beam energy is 34 kV. At z = 30 cm the gas pressure is 1.7 mTorr.

that two sets of data are very similar for $I_b < I_{opt}$ (the lower of the two values), differ as I_b approaches I_{opt} (the lower of the two values), and have similar maximum values of T_e. Therefore we see that the jump behavior of T_e is associated with the approach of I_b to I_{opt}, as opposed to a threshold in beam current density.

5. Anomalous Power

Let us reflect momentarily on the performance of the collisional model for I_b below I_{opt}; the collisional model produces remarkable agreement with our data. The significance of this agreement is that the terms included in the power balance are apparently correct. The input power is from Coulomb collisions, as evidenced by correctly predicting dT_e/dI_b. The power losses are from electrons born trapped by the potential well and from inelastic collisions, as evidenced by the behavior of the T_e intercept with $\sqrt{\phi_i}$ and n_g.

Given this agreement, there is no way to produce a jump in T_e without an additional power input, an input that is available only for I_b near I_{opt}. Bolstered by the agreement of the data with the collisional model for I_b below I_{opt} (where we cannot perform the numerical integration), we have confidence that the numerically integrated terms correctly represent the collisional terms in the power balance at I_{opt}. Then P_{anom} given by Eq. 2.11 and calculated for our sample data in Eq. 5.5 is an anomalous power input we must find in order to account for the jump behavior of I_b.

As anticipated in Chapter 3, we shall show in Sec. B that the source of this anomalous power is a beam-plasma instability. Only the

full energy proton component of the beam will contribute, so each proton loses some energy by an "anomalous" process:

$$\Delta E_{anom} = \frac{P_{anom}}{I_1}$$

$$= \frac{6.9 \cdot 10^{20} \text{V/sec } 1.6 \cdot 10^{-19} \text{C}}{.6 \cdot 5.1 \text{ C/sec}} = 36 \text{ V} \qquad (5.10)$$

where we have used Eq. 5.5 and converted the real current unit of proton current (60% of I_b), I_1(Amp), to a particle current.

This ΔE_{anom} will be used in evaluating the beam-plasma interaction. It has been calculated for the highest gas pressure operated at and highest electron temperature observed at E_b = 25 kV. It thus is an upper bound.

B. Beam-Driven Wave Heating of Electrons

The single most glaring failure of the collisional model was its inability to predict the jump behavior of T_e with I_b. We begin by showing that this jump behavior is a result of increased beam divergence when operating below the optimum beam current (I_{opt}). We then show a striking correspondence between the jump in T_e and the jump in observed fluctuation signal levels. The power spectrum agrees quantitatively with expectations for our beam-plasma system. Finally we show that the observed slope of T_e versus E_b is less than that of Eq. 2.21, which one would expect in the face of nonlinear fluctuation levels and nonuniform densities.

1. Current Threshold

Ion temperatures in the source for the accelerator are typically <10 V.[24] The spread of beam energies, ΔE_b, after acceleration is therefore $\Delta E_b < 10$ V. The initial spread in beam velocities is $\Delta v_b = \Delta E_b / m_b v_b$. Thus, at the entrance to the neutralizer,

$$T_b = 1/2\ m(\Delta v_b)^2$$

$$\leq \frac{1}{4} \frac{(10\ V)^2}{E_b} \quad .$$

$$= .001\ V \quad @\ E_b = 25\ kV,$$

whereas Eq. 2.25 indicates the cold-beam growth rate valid for $T_b < 7.6$ eV. Were our accelerator an ideal one, with source-limited divergence at all current densities, there would be no instability threshold with I_b for fixed E_b.

However, the dislocation and distortion of the source sheath when $I_b < I_{opt}$ (described in Section A.4.b.i.) causes substantial beam ion velocity ($v_\perp$) perpendicular to the nominal beam direction. This $v_\perp$ will affect the instability by increasing $\Delta v_\parallel$, the spread in parallel velocities. Ironically, the excessive divergence observed below $I_b = I_{opt}$, once viewed as an obstacle to observing the true dependence of T_e upon I_b, provides a vital clue to the source of electron energy, by providing an independent means of turning off the instability.

When the spread of parallel (to the wave) velocities ($\Delta v_\parallel$) exceeds $v_{slip} = 0.02\ v_b$ (evaluation of Eq. 3.23 for our standard parameters), wave growth will diminish. Since $\Delta E_b < 10$ V, all beam ions have essentially the same energy ($v_\perp^2 + v_\parallel^2$). Think of the divergence then

as a spread in angles ($\Delta\theta$), giving rise to a spread in parallel velocities:

$$\Delta v_{\parallel} = (1 - \cos \Delta\theta)\, v_b \simeq \frac{\Delta\theta^2}{2}\, v_b .$$

Stability returns when $\Delta v_{\parallel} > 0.02\, v_b$ or,

$$\Delta\theta = \cos^{-1}(1 - 0.02)$$
$$= 11 \text{ deg.}$$

When $\Delta\theta$ exceeds 11 deg., we expect stability, or at least diminished growth resulting from the spread in $v_{\parallel}$.

By looking at the intercept of the beam edge at 30 cm downstream (see Fig. 5-8) we see that the spread in beam angle at $I_b = 4.5$ A (I_b at which the which jump begins) is approximately,

$$\Delta\theta = \sin^{-1} (\Delta x/30 \text{ cm})$$
$$= \sin^{-1}(4/30)$$
$$= 8 \text{ deg.} ,$$

where $\Delta x = 4$ cm and is interpreted from Fig. 5-8 as the change in intercept between $I_b = 4.5$ and 5.5 A. We see from Fig. 5-1 (the H_2 data) that $I_b = 4.5$ A is the beginning of the T_e jump. We further note that the temperature has reached a plateau by $I_b = 5.5$ A. Not only does considering the effect of beam divergence on the instability predict a "threshold" in I_b, but we see fair agreement with the current range at which the jump occurs.

It should be pointed out that the data for He shown in Fig. 5-1 exhibits its jump at a lower I_b than does the H_2 data. This results from a significant fraction of He^+ in the beam, increasing the

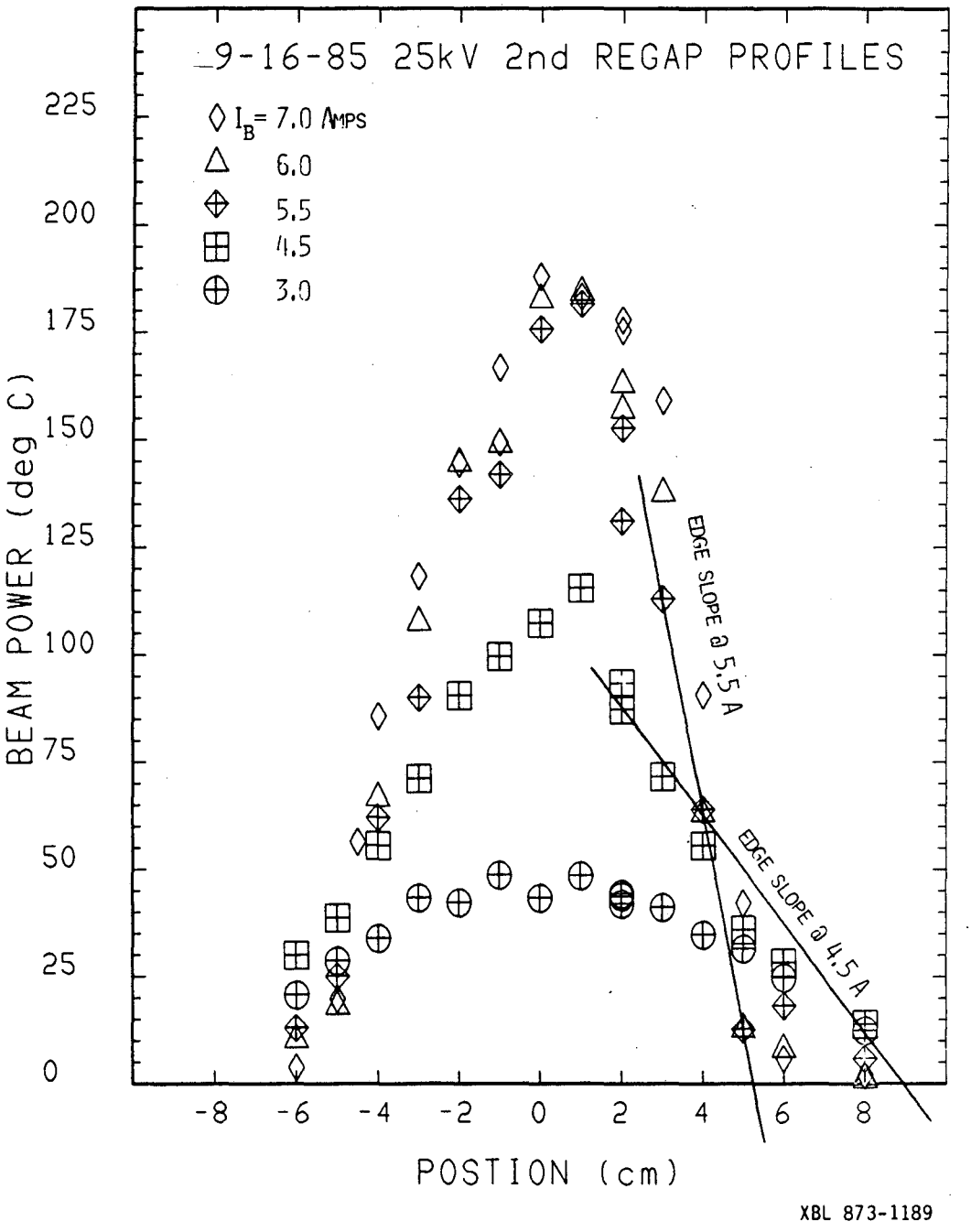

Fig. 5-8 Radial Beam Profiles at Z = 30 cm. Beam energy is 25 kV. The beam power is recorded and shown as the temperature rise of a small, moveable calorimeter. Notice that the intercepts of the I_b=5.5 A and the I_b=4.5 A edge slopes are located at approximately 5 cm and 9 cm, respectively.

effective beam mass in Eq. 5.8. This causes a reduction in the optimum beam current from that of the H_2 data. This is confirmed by beam dump calorimetry; in Fig. 5-9 the observed beam divergence is plotted along with T_e for the He data of Fig. 5-1.

In fig.'s 5-6 and 5-9 notice a lack of any beam divergence data for I_b significantly below I_b at which the T_e jump begins. There are three reasons: 1) the beam dump calorimeter loses sensitivity for larger divergences; 2) there is some beam collimation for $\Delta\theta > 6$ deg.; and 3) the beam divergence increases rapidly as I_b is decreased in this region. This latter effect is apparent in fig.'s 5-6 and 5-9 and confirmed by Fig. 5-8; the peak beam power density decreases much more rapidly than I_b for $I_b < 5$ A. For these reasons we; 1) use the relatively crude measurement of the "edge slope" to compare with the stability criterion ($\Delta\theta > 11$ deg); and 2) concede a greater uncertainty in the actual beam divergence (at these large $\Delta\theta$'s) than the reproducibility would suggest. Nonetheless, the correlation of the T_e jump to the drop in $\Delta\theta$ cannot be denied.

2. Plasma Fluctuation Measurements

a. Spectrum

The fluctuation spectrum observed at z = 30 cm on our probe inside the beam is shown in Fig. 5-10 for $E_b = 25$ kV and $I_b = 4.95$ A. The large error bars reflect both the noise level of the spectrum analyzer and the difficulty of making spectral measurements upon a slowly time varying amplitude with a sweep oscillator and mixer. The slow time dependence (~ 10 ms) results from unavoidable current drift in the ion

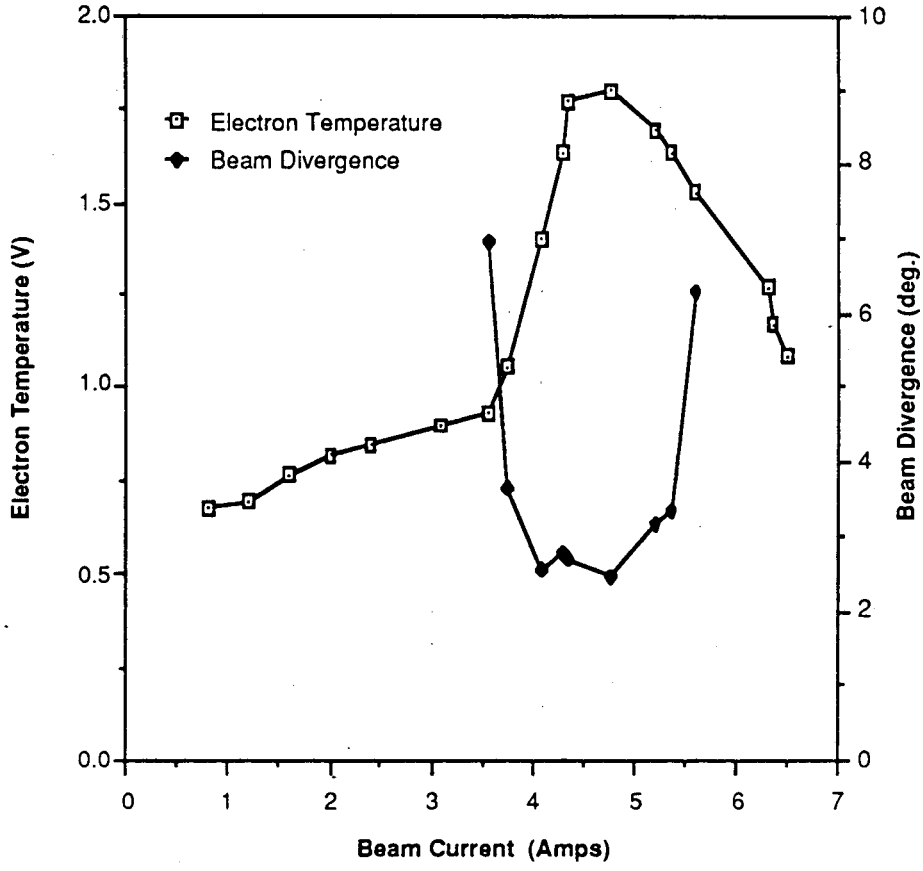

Fig. 5-9 Electron Temperature and Beam Divergence as a Function of Beam Current. The angular divergence (1/e) of the beam is measured on a beam dump calorimeter 3 m from the accelerator. The electron temperatures plotted are the He data from Fig. 5-1.

a)

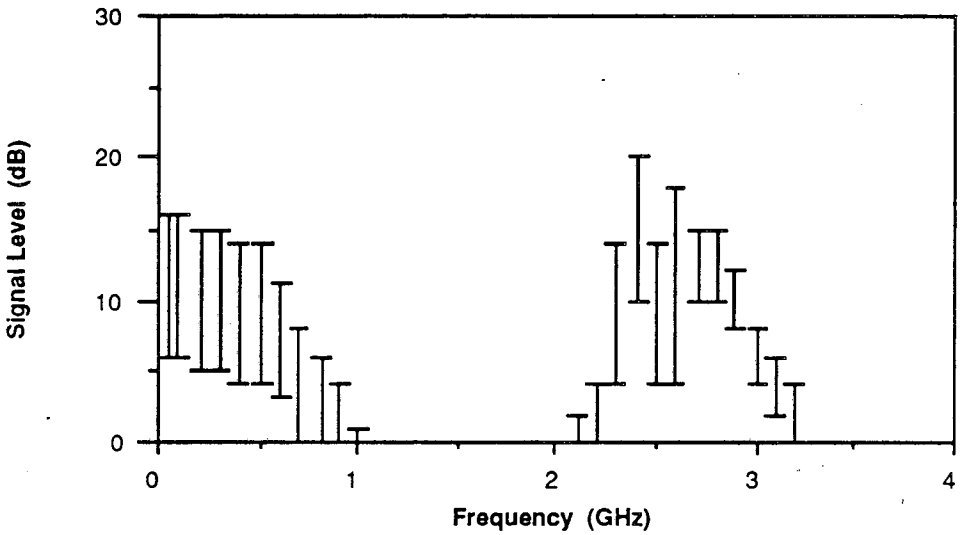

b)

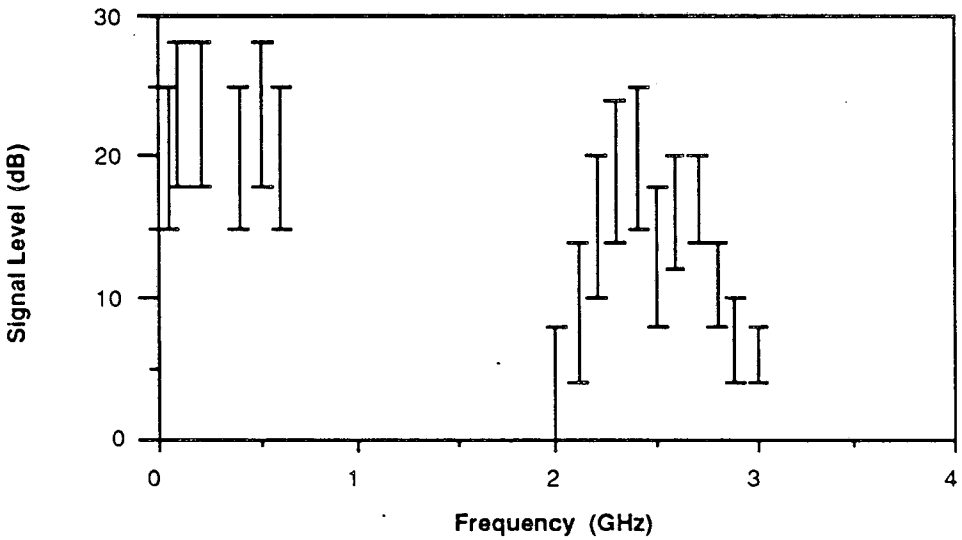

Fig. 5-10 Frequency Spectra. a) Beam current = 4.95 A
b) Beam current = 5.45 A.

source, at I_b (4.95 A) where the beam optics and (as we showed in the last section) fluctuation level will vary the most. It is not certain how the plasma fluctuations are coupled to the probe. Large coupling losses of the electrostatic wave across the sheath make it very likely that we are measuring modulated beam current. Also note from Table 3-1 that (the most unstable wavelength) $\lambda \leq 1$ mm, which makes orientation of our 1.1 cm diameter probe very critical. The high voltage hazard posed by the accelerator made fine tuning of the probe orientation impractical, which increases any already existing uncertainties in the probe coupling. For these reasons, we make only relative amplitude comparisons, precluding also an amplitude comparison between the upper and lower bands. Our interpretation of the spectrum is as follows.

Locally, n_e is measured as $n_e = 6 \cdot 10^{10}/cm^3$, which corresponds to a local plasma frequency of $f_p = 2.2$ GHz. This explains the "cutoff" of the upper band below 2.3 GHz. In Appendix F we show that the bandwidth of the instability is only 0.05 ω_e (~100 MHz). The bandwidth (~ 1 GHz) of the upper band is much larger and could reflect either of two effects, though both have to do with f_p at the origination point of the waves that are being detected at z = 30 cm. The first possibility is that the upper frequency roll off represents f_p at the highest density point upstream from z = 30 cm, namely that at z = 0. Based on the change (50%) of ion production between z = 0 and z = 30 (See Fig. C-1a) we would expect the upper f_p roll off to be at $\sqrt{2} \cdot f_p$ (cutoff). This is essentially the case. The second possible explanation for the spectral width lies in the radial density

profile in the vicinity of the probe (or at a fixed z upstream from probe). This again would be a frequency ratio of nearly $\sqrt{2}$.

The lower band is in a frequency range ($f_i < f < f_p$) that, save for the presence of the beam, would be evanescent. However, this spectrum was observed inside the beam, where a propagating beam mode exists down to f = 0 (see Fig. 3-2). This beam mode is nearly stable and one would not expect to see what appears to be a strong signal. In Chapter 3, Section C we calculated from Eq. 3.13 that (the required wave energy density) $W_{req} = 6 \cdot 10^{10}$ V/cm^3. Compare this with the average thermal energy density,

$$\bar{n}_e T_e = 5 \cdot 10^{10}/\text{cm}^3 \cdot 1.8 \text{ V} = 9 \cdot 10^{10} \text{ V/cm}^3. \quad \text{Since}$$

$$W_{req} \simeq 0.6\, \bar{n}_e T_e \,, \tag{5.11}$$

we expect significant nonlinear effects. One of these will surely be wave-wave interactions, specifically resonant mode coupling of two unstable waves. If we consider two parent waves (described by ω_1, k_1 and ω_2, k_2) we find that the daughter wave (described by ω_3, k_3), automatically satisfies the phase matching conditions,

$$\omega_1 - \omega_2 = \omega_3 \qquad \text{and}$$
$$k_1 - k_2 = k_3.$$

This is because all three waves satisfy $\omega/k = v_b$ [the parents because they were presumed resonant and the daughter because it is a beam mode; see Fig. 3-2, where it is graphically apparent (the dispersion relation is plotted for $v_b = 3.9\ V_e$) that any propagating mode below ω_e has $\omega/k = v_b$]. This wave-wave interaction also explains why the lower frequency band has the same spectral width as the upper band.

Since we do not know the wave-to-probe coupling, we cannot make any meaningful observations regarding the relative level of these two bands within the spectrum. Since the lower band results from the product of two waves in the upper band, we would expect, however, that the lower band should grow at twice the rate of the upper band, specifically when comparing spectra of two different I_b. Let W_1, W_2, and W_3 be the wave energy density of the two parent waves and the daughter wave respectively. The steady-state amplitude of the daughter wave is then described by the vanishing of its time derivative; pumping from the two parents and linear Landau damping act upon the daughter. Then

$$\frac{dW_3}{dt} = c_{12} W_1 W_2 - 2 \gamma_L W_3 = 0 ;$$

where c_{12} is the coupling coefficient between the parent waves and γ_L is the Landau damping rate for the daughter; implies that

$$W_3 \propto W_1 W_2, \text{ or } P_{low} \propto P_{high}^2 ,$$

where P_{low} and P_{high} are the fluctuation power levels for the lower and upper frequency bands, respectively. Thus we would expect to observe, for an incremental power increase of 10 dB in the upper band, an incremental increase of 20 dB in the lower band.

Fig. 5-10b shows, for I_b = 5.45 A, a spectrum similar to that for I_b = 4.95 A. We see that the incremental increase of power in the lower frequency band is indeed approximately twice the incremental increase of power in the upper band. This supports the argument that the low frequency band results from wave-wave interactions within the upper frequency band.

b. Correlation of Fluctuation Level with T_e

Fig. 5-11 illustrates the remarkable correlation of T_e measurements with the fluctuation level at 400 MHz observed on the probe. Below I_b = 4.5 A, the signal is below the noise level of the spectrum analyzer, but rises 30dB in the span of 1 A. This rapid rise in fluctuation level begins at exactly the same I_b as does the jump in T_e. This strongly suggests that the instability is providing the power that drives T_e upward.

3. Temperature Dependence upon E_b

Recall that we already demonstrated in Chapter 3, Section D, that sufficient coupling of power from the beam to the plasma electrons exists to support the electron temperatures we observe. Hence we expect to observe the dependence $T_e \propto E_b$. Our measurements of T_e are plotted versus E_b in Fig. 5-12. Since this data is presented to compare with the anomalous prediction of Eq. 3.21 ($T_e = 0.18\, m_e E_b/m_b$), we have plotted peak T_e observed at each E_b. The first three data points are from the neutralizer described in this thesis, and the error bars reflect the scatter in peak T_e over a wide variety of operating conditions - different neutral pressures and all of the three accelerator gaps used. These three gaps provided a range of I_b (while maintaining optimum j_b as per Eq. 5.8, the Child-Langmuir law) spanning almost a factor of 2. The line drawn is deliberately constrained to pass through the origin in order to be representive of Eq. 3.21 and has a slope of 0.07 V/kV, which is 30% lower than the slope of Eq. 3.21. Recall that Eq. 3.21 was derived by equating

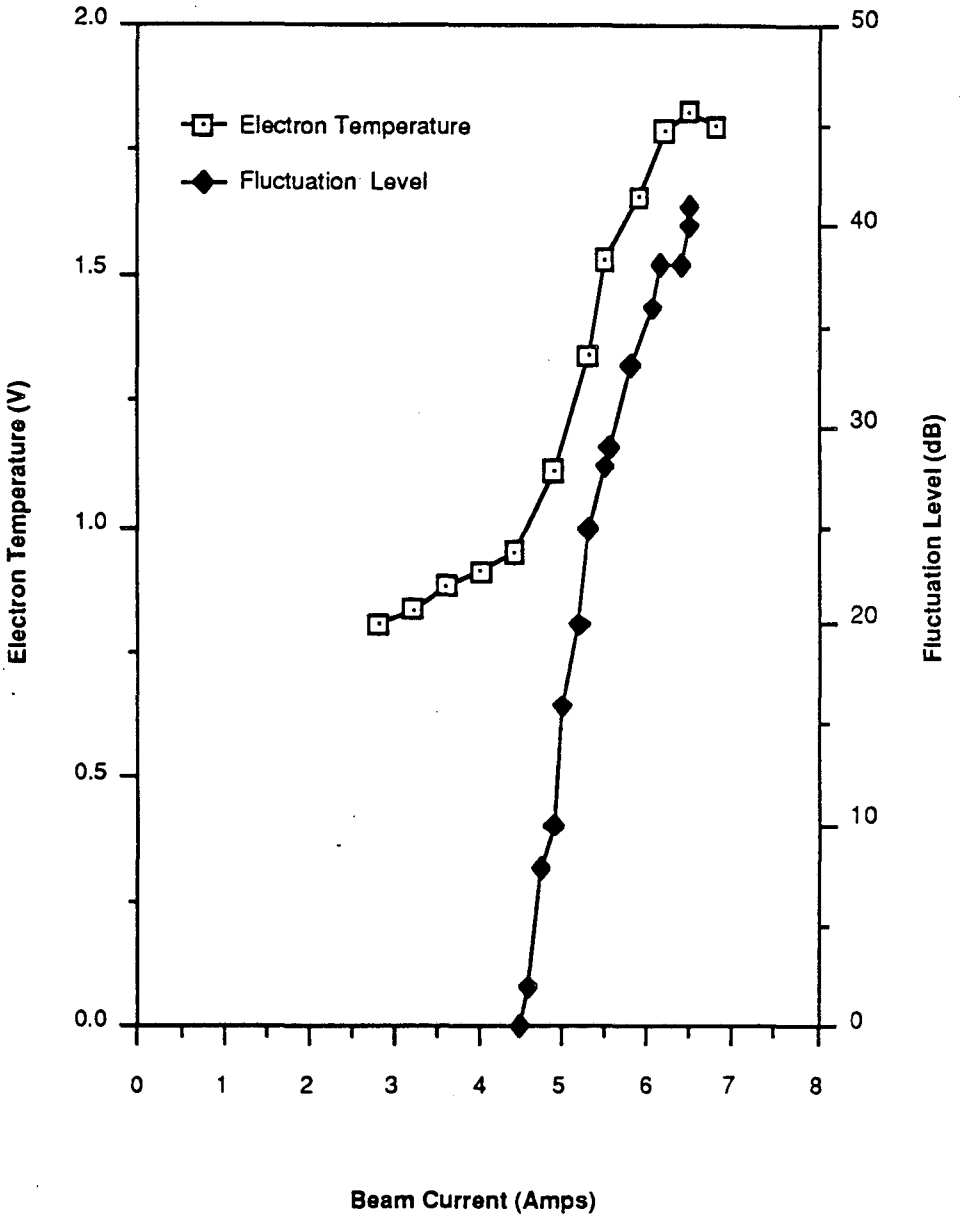

Fig. 5-11 Electron Temperature and Fluctuation Signal Level as a Function of Beam Current. The fluctuation signal is observed on a 1 sq. cm. planar probe.

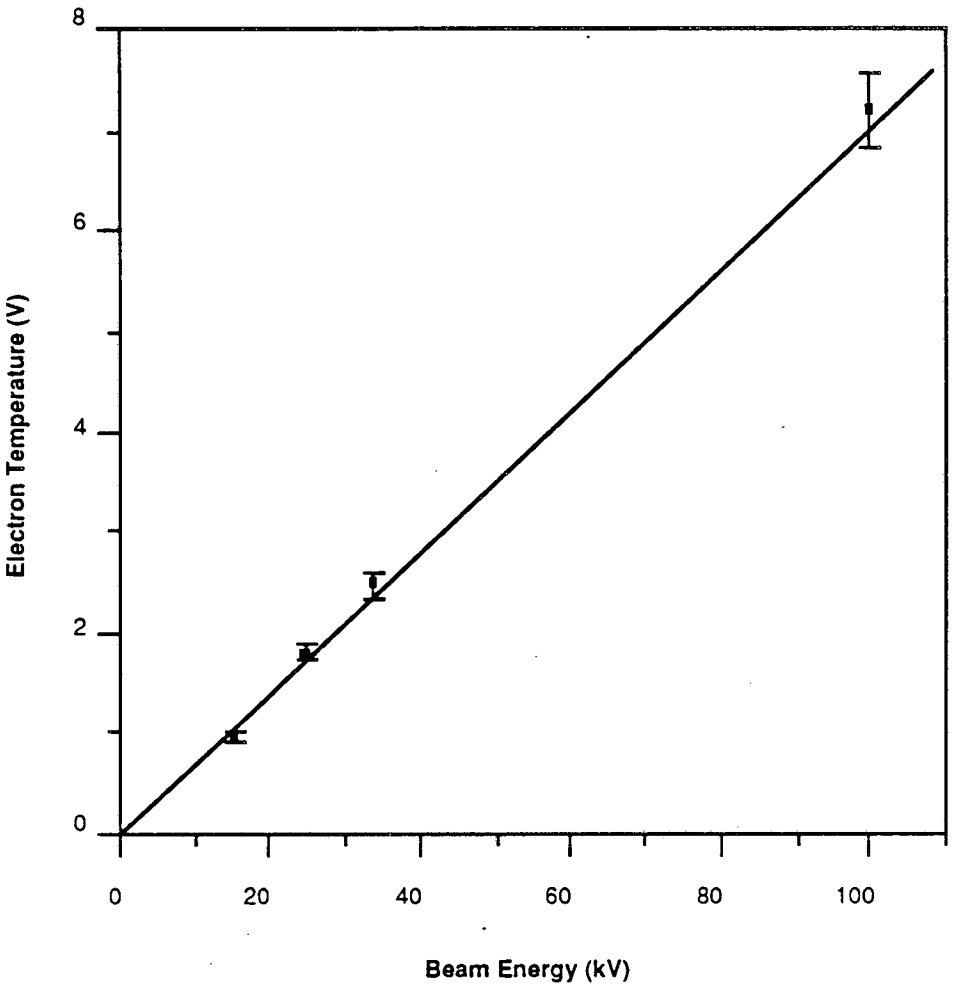

Fig. 5-12 Peak Electron Temperature Versus Beam Energy. The first three data points are our own data. The data at 100 kV is a private communication from another facility.

Landau damping with the linear resonant-beam growth rate, which implied $k_o\lambda_D = v_e/v_b = 0.3$. Due to the nonlinear character of the oscillations revealed by Eq. 5.11 ($W_{req} = 0.6\ \bar{n}_e\ T_e$), we would certainly expect the resonant growth rate to be below that of the linear solution; the corresponding reduction in Landau damping required then implies $k_o\lambda_D < 0.3$. The slope from Fig. 5-12 is equivalent to $k_o\lambda_D = 0.26$. This seems to be adequate agreement in view of the necessity for a vastly more complicated nonlinear analysis to determine the exact T_e at saturation.

The lone data point at $E_b = 100$ kV was taken by Kurt Schoenberg[25] on a different neutralizer (of larger cross section and length 3m length) and with $I_b = 11$ A. We assume error bars comparable to our data.

4. Gas Pressure Independence of T_e

Note the indepence of Eq. 3.21 ($T_e = 0.18\ m_e E_b/m_b$) to gas pressure or gas species. Look back at Fig. 5-1 and observe that the peak value of T_e is essentially independent of gas pressure or species. This observation certainly fits within the framework of our model for anomalous heating by beam-driven electron plasma oscillations.

C. Summary

For I_b below I_{opt} our data is adequately described by the collisional model. The I_b dependence of T_e agrees very well. The T_e intercept at $I_b = 0$ exhibits the proper dependence upon gas pressure

and species (H_2 or He). The collisional model fails only to explain the jump in T_e as I_b approaches I_{opt}; the high value of T_e after this jump; and the insensitivity of this value to gas pressure and species.

We have seen that the linear wave model correctly predicts the jump behavior of T_e with I_b, correlating the jump with the reduction in beam divergence and presumed subsequent onset of instability. A strong correlation of T_e with electrostatic fluctuation level and with beam divergence is observed. We also find the saturation (peak) T_e's (and hence dependence upon E_b) to be 30% below those of Eq. 3.21, consistent with the notion of reduced wave growth in the presence of nonlinear wave amplitudes. The linear wave model correctly predicts the insensitivity of the saturation T_e's to gas pressure and gas species.

Thus we see that the two models, each in its own regime, agree with our observations of T_e in this plasma.25

Chapter 6

Conclusions

We have measured the electron temperature in a neutralizer plasma. To understand the behavior of T_e, we have presented a collisional model for the power balance (described in Ch. 2), in which we compare the power drains on the system with the input power available from Coulomb collisions of beam ions with plasma electrons. The power drains considered are: (1) the power necessary to remove from the potential well electrons that are born with less kinetic energy than the potential well depth; (2) inelastic collisions of plasma electrons with H_2 molecules; and (3) the kinetic energy ($\sim T_e$) that each electron still has when it is collected on the wall. With the data presented in Ch. 5 we have shown that this model correctly predicts the dependence of the electron temperature upon beam current and gas pressure only for beam currents below I_{opt} (accelerated current that minimizes the beam's angular divergence); i.e., when the beam-plasma instability is suppressed by the large angular divergence of the beam. At I_{opt}, the collisional model predicts an upper bound for T_e dependence of $\sqrt{E_b}$, inconsistent with the linear dependence we observe. In addition we found numerical values for the anomalous power required to support the observed peak T_e's. With these values as inputs, we described theoretically in Ch. 3 an electrostatic ion-beam-driven electron plasma instability that provides this required beam power to the electrons, but at a possibly nonlinear fluctuating potential level. Sec. B of Ch. 5 presented our data

showing the strong correlation of beam angular divergence, electrostatic noise amplitude, and T_e. Resonant wave growth is possible only when the beam parallel velocity spread is less than the slip velocity between the beam and the resonant phase velocity of the wave. This requirement nearly predicted the beam angular divergence and, hence, I_b at which the observed T_e jump occurs. The observed oscillation spectrum agrees very well with that which one would expect from a nonlinear fluctuation level. Our observed scaling of (peak) $T_e = 0.07\ E_b$ V/kV is ~ 30% below the linear relation between T_e and E_b predicted by equating the linear growth rate with the Landau damping rate. This 30% decrease could be consistant with a reduction in the growth rate expected in light of the nonlinear wave amplitudes predicted. We feel that a fairly complete understanding of the electron energy balance is in hand.

The latter part of Ch. 3 was devoted to generalizing our results to other systems. Eq. 3.24 gave the upper limit on resonant energy loss from the beam, typically a few percent. The parameter ζ (the ratio of plasma production by heated electrons to that by the beam) was employed as a measure of the plasma's effect on the neutralizer gas. This seems a reasonable indicator since the beam's effect on the gas can be simply calculated. We found that, after initially increasing, ζ decreased with E_b (for E_b > 90 kV). This apparent paradox was resolved by realizing that the power available for electronic ionization is independent of the target gas density, while beam production of plasma by ionization is proportional to n_g. The need for increasing target thickness ($n_g L$) to compensate for the

decline of σ_{cx} with E_b allows beam production of plasma to again exceed that of electronic ionization. This occurs at around E_b = 140 kV in our example. This seemingly fortuitous turn of physics is rendered moot, however, by the very same decline of σ_{cx}. The neutralization efficiency is so poor (σ_{cx}/σ(stripping of beam H^o) < 0.1) as to make positive ion based 140 kV H^o beams unattractive.

The power available from the instability does provide for $\zeta \sim 3$ at 80 kV. Can anything change this? Yes - by increasing the neutralizer cross section (A_p) and thereby decreasing A_b/A_p (see Eq.3.54), one can spread this power over a larger volume and effect a lower percent ionization of the gas. This lower percent ionization comes, however, at the expense of increasing the total gas flux. Or, by shortening the neutralizer one might hope to employ stabilization of the instability by a steep electron density gradient. We have shown in Eq. 3.28 that the wave reaches saturation amplitude in traversing 9 cm axially. For gradient stabilization, one would need to restrict the spatial extent of wave growth to less than 9 cm. We have shown (Appendix F) that propagating through a 10% decline in plasma density shifts the wave frequency out of resonance, thus quenching wave growth. The above conditions then imply

$$\frac{1}{n_e}\frac{dn_e}{dx} > 10\%/9 \text{ cm} \sim 1\%/\text{cm} \qquad (6.1)$$

everywhere within the beam for stabilization by density gradient. The actual requirement is considerably stricter. By considering only a single mode contributing to the beam energy loss, Eq. 6.1 represents

an upper bound. Since waves growing in all axial regions of the beam contribute to the power coupling, each wave does not have to saturate by beam velocity spreading. One could reasonably expect a density gradient an order of magnitude larger than Eq. 6.1 to be necessary for stabilization of the resonant instability. This would imply a neutralizer of length 10 cm, significantly affecting the ability to maintain proper target thickness.

Ultimately, the solution employed in the past will likely prevail; when confronted with a neutralizer target thickness lower than expected from the cold gas fill, most operators of neutral beamlines have simply increased the gas flow. We hope, however, that this thesis - specifically, the possibility of neutralizer burn-out discussed in Chapter 3, Section G - will enlighten those who have found that to be necessary and provide insight for those hoping to optimize the gas loading of such systems. The next step will be to determine the implications that this work holds for negative-ion-based neutral beams.

APPENDIX A

Energy Loss of Beam Atoms Colliding with Electrons

We seek the energy delivered to the plasma electrons by the fast beam atoms. Cross sections for energetic atoms impinging upon electrons are difficult to find in the literature. Hence we present two simple approximations that both represent upper bounds:

1. We consider the electron and atom to be hard spheres. Taking advantage of the frame invariance of total cross sections, we assume an atomic "size" corresponding to observed elastic cross sections (σ_{el}) of electrons on H^0, taken at the speed of the approaching atom.

The kinematics of hard sphere scattering are rather well described in other literature.[26] In the lab frame, the average energy change of the beam atoms

$$\Delta E_b = \frac{2m_e m_b}{(m_e + m_b)^2} E_b \simeq \frac{2m_e}{m_b} E_b \qquad (A1)$$

where m_e, m_b, and E_b are the electron mass, atomic mass of hydrogen, and the beam kinetic energy, respectively. Thus the atomic beam energy loss per unit length is

$$\frac{dE_b}{dz} = \Delta E_b \; n_e \; \sigma_{el}$$

$$= 2 \frac{m_e}{m_b} E_b \; n_e \; \sigma_{el} \qquad (A2)$$

$$\simeq 8 \cdot 10^{-15} n_e \quad (V/cm) \qquad \text{with } n_e \text{ in } cm^{-3},$$

where n_e is the electron density, σ_{el} is the elastic cross section of electrons on H^0 at the speed of the 25 kV beam atom (an electron

energy of 13.6 V), which we take to be $3 \cdot 10^{-16}$ cm^2,[27] and with E_b = 25 kV. This is approximately 25 times smaller than the spatial energy loss rate calculated for Coulomb collisions via Eq. 2.8.

2. As a second estimate for the energy loss rate of atoms on electrons, we calculate the energy loss as if the atom were a proton incident upon the electron, but we reduce the upper bound on the impact parameter. While integrating over impact parameter, the usual choice for the upper limit of integration is the Debye length (λ_D). For the upper limit of integration over impact parameter, we use R_{el}, an imagined radius such that $\pi R_{el}^2 = \sigma_{el}$, where we again use $\sigma_{el} \approx 3 \cdot 10^{-16}$ cm^2. Thus most of this calculation can be found in existing literature.

In the center-of-mass frame of reference, an incident particle with an impact parameter b is scattered by an angle $\theta = \pi - 2\psi$ (see Fig. A-1), where[28]

$$\tan \psi = b \cdot (\mu v^2 e^{-2}) \equiv b / b_o \qquad \text{(A3)}$$

where e is the electronic charge, $\mu = m_e m_b/(m_e + m_b)$, and v is the beam velocity. After the collision, the target electron has kinetic energy[29]

$$E_e = \beta E_b (1 + \tan^2 \psi)^{-1} \qquad \text{where} \qquad \text{(A4)}$$

$$\beta = 4 m_e m_b / (m_e + m_b)^2 \approx 4 m_e / m_b \ .$$

The energy lost by the atomic beam per unit length is then

$$\frac{dE_b}{dz} = \beta n_e E_b \int_0^{b_m} (1 + \tan^2\psi)^{-1} 2\pi b \, db \qquad \text{(A6)}$$

where b_m is the maximum impact parameter considered (to be discussed

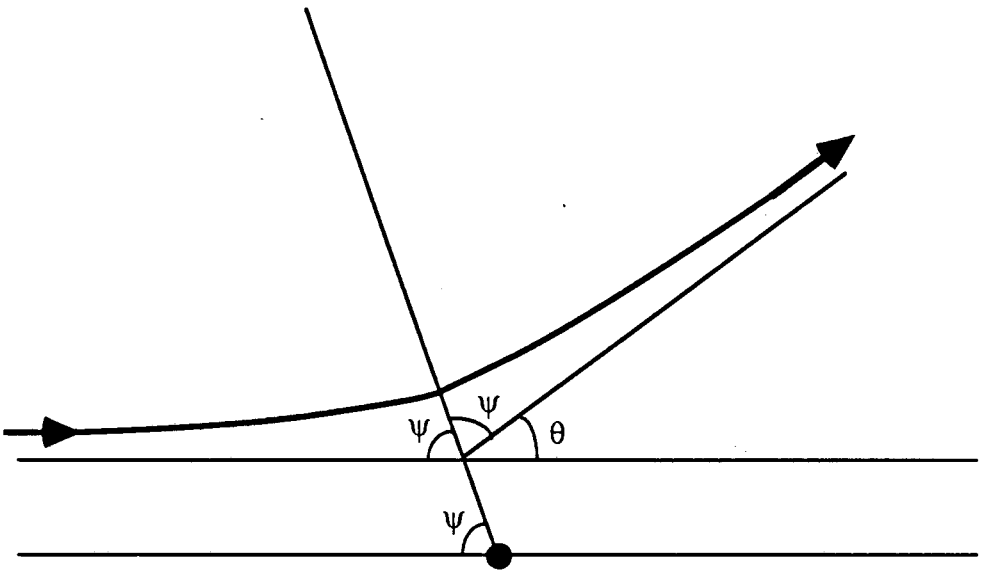

Fig. A-1 Scattering Angles in the Center of Mass Frame.

shortly). After integration,

$$\frac{dE_b}{dz} = \frac{2\pi_e n\ e^4}{m_e v_b^2}\ \ln\left(1 + \frac{b_m^2}{b_o^2}\right) \qquad (A7)$$

If we take $b_m = R_{el}$, then $b_m \approx b_o$ and

$$\frac{dE_b}{dz} = \frac{2\pi\ n_e\ e^4}{m_e\ v_b^2}\ \ln(2). \qquad (A8)$$

We wish to compare this rate with that for ions colliding with electrons. In that case the common choice for b_m is the Debye length (λ_D). Since $\lambda_D \gg b_o$, we regain the familiar $\ln(\Lambda = \lambda_D/b_o)$ dependence usually seen for the Coulomb reaction. The ratio of energy loss rates for ions versus atoms is then $\frac{2\ln(\Lambda)}{\ln(2)} \approx 60$ for our plasma.

For simplicity we have shown this calculation for the case of the "field" particle (the electron) at rest. The well-known solution by Chandrasekhar[30] for an ensemble of field particles not at rest differs by < 10 % from our calculation for ion impact. The smallness of the thermal field correction is a result of $v_b > 3$ times the electron thermal speed. Therefore we feel this simplification does not affect our conclusion.

The first approximation very likely overestimates the energy loss by beam atoms, by treating atoms scattered at large impact parameter as though they lost the average energy. The second approximation probably underestimates the energy loss by abruptly cutting off the integral at R_{el}. For the purpose of comparison, though, even the overestimate of the first approximation tells us that the energy loss rate for beam atoms is smaller than that for protons by a factor of 25. Thus electron heating by beam atoms is negligible.

Appendix B

Beam Species

The beam begins its path through the neutralizer as three components: H^+, H_2^+ and H_3^+. The fate of the H^+ ions was described in Chaper 2, Section A. In this appendix we shall address the molecular interactions. For H_3^+ striking an H_2 molecule, the possible fast (beam) products are $H_2^+ + H^o$, $H_2^+ + H^+$, $H_2^o + H^+$, $H_2^o + H^o$, $2\,H^+ + H^o$, $2H^o + H^+$, $3\,H^o$, and $3\,H^+$. The first is the most common reaction. Note in that case that the H_2^+ has 2/3 of the original energy, the H^o has 1/3, so all have 1/3 original energy/nucleon. In subsequent interactions, the 2/3 energy $H_2^{+,o}$ can dissociate, and the products become 1/3 energy. For initial H_2^+, the products are similar to those from H_3^+, but simpler by one nucleon.

The resultant beam components are:

Full Energy/nucleon: H^+, H^o, H^-

1/2 Energy/nucleon: H^+, H^o, H^-, H_2^+, H_2^o

1/3 Energy/nucleon: H^+, H^o, H^-, H_2^+, H_2^o, H_3^+

These are plotted in Fig. B-1 as they evolve axially, assuming a neutral pressure of 2.8 mTorr measured at z = 30 cm. (We have employed a computer program written by Warren Stearns[31] to follow the spatial evolution of the beam.)

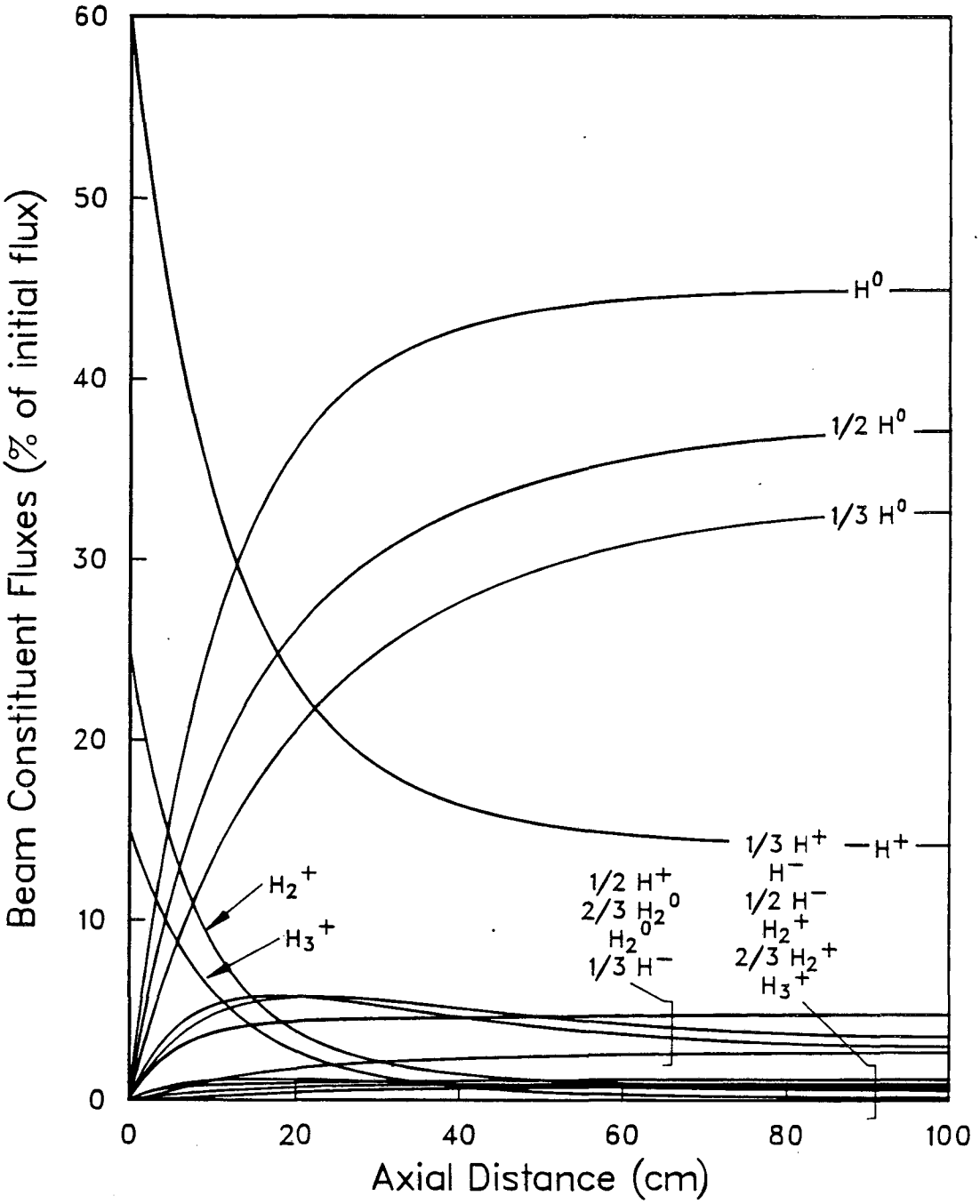

Fig. B-1 Evolution of the Beam Particle Fluxes as the Beam Travels Axially. These have been calculated for an initial beam species mix of 60% H^+, 25% H_2^+, and 15% H_3^+ ; E_b = 25 kV; and a gas pressure of 2.8 mTorr at z=30 cm. The fractions in the curve labels refer to the energy of that species relative to E_b.

Appendix C

Numerical Integration of Collisional Terms

In this appendix we manipulate the general expressions of Chapter 2 into a form easily integrated by computer. All of the four power equations involve an integral with $n_g dz$. This can also be represented by a differential of target thickness

$$d\Pi = n_g dz, \tag{C1}$$

so we make the natural transformation from dz to dΠ. Warren Stearns[31] has written a program to follow the evolution of the beam species as they traverse a target, incrementing each beam flux by

$$\Delta I_s = \sum_{s'} I_{s'} \sigma_{ss'} \Delta\Pi , \tag{C2}$$

where ΔΠ is the incremental target thickness and $\sigma_{ss'}$ is the cross section for the interaction of species s' with H_2 producing species s. Some of $\sigma_{ss'}$ will be zero, for example when $v_s \neq v_{s'}$. We have extended this program to perform the integrals required in the power balance. At each step, Π is incremental by ΔΠ and the beam fluxes are incremented according to Eq. C2. The appropriate functions will be summed over these steps to represent the four power terms of Chapter 2.

1. Power Required to Expel Electrons Trapped in the Well

We begin by evaluating the integral over energy occurring in Eq. 2.3,

$$G(\phi) \equiv \int_0^{\phi_p(x,y,z)} f(\varepsilon)(\phi_p(x,y,z)-\varepsilon)d\varepsilon \quad .$$

With Eq. 2.1 for $f(\varepsilon)$,

$$G(\phi_p) = \phi_p + E_n(e^{-\phi_p/E_n} - 1) \quad .$$

For simplicity, we ignore the variation of ϕ_p across the beam ($\delta\phi_b \simeq T_e$) compared with ϕ_p at the center of the beam [$\phi_p(r=0)$ is often $8 \cdot T_e$]. Then the only radial variation in Eq. 2.3 is that of n_s. But $\int_o^{A_b} n_s v_s dA = I_s$ (I_s is a particle flux = current/e), so Eq. 2.3 becomes

$$P_{Tr} = \sum_s \sigma_s^e \int_0^L G(\phi_p(r=0,z))\ I_s n_g dz \quad .$$

If we denote the total target thickness by $\Pi_L \equiv \int_o^L n_g dz$, then

$$P_{Tr} = \sum_s \sigma_s \int^{\Pi_L} G(\phi_p(\Pi))\ I_s\ d\Pi \quad . \qquad \text{(C3)}$$

Relating ϕ_p to Π is the next step. We assume the electrons follow the Boltzmann relation $n_e \propto e^{-\phi/T}$. We also assume $n_e \simeq n_i$ and relate n_i to the local production rate;

$$n_i v_i S_b = n_g(z) \sum_s n_s(z)\ \sigma_s^{ion}\ v_s\ A_b$$

$$n_i v_i \propto n_g(z) \sum_s I_s(z)\ \sigma_s^{ion} \qquad \text{(C4)}$$

where σ_s^{ion} is the cross section for ion production by beam species s, and S_b amd A_b are the beam circumference and cross sectional area, respectively. $\sum_s I_s(z)\ \sigma_s^{ion}$ is plotted in Fig. C-1a. To arrive at the proportionality we neglect beam divergence and assume the perpendicular (radial) beam profile to be axially uniform. Remember, the axial dependence is what we seek here. Since the electrons are thermalized, T_e, and hence v_i, is independent of z.

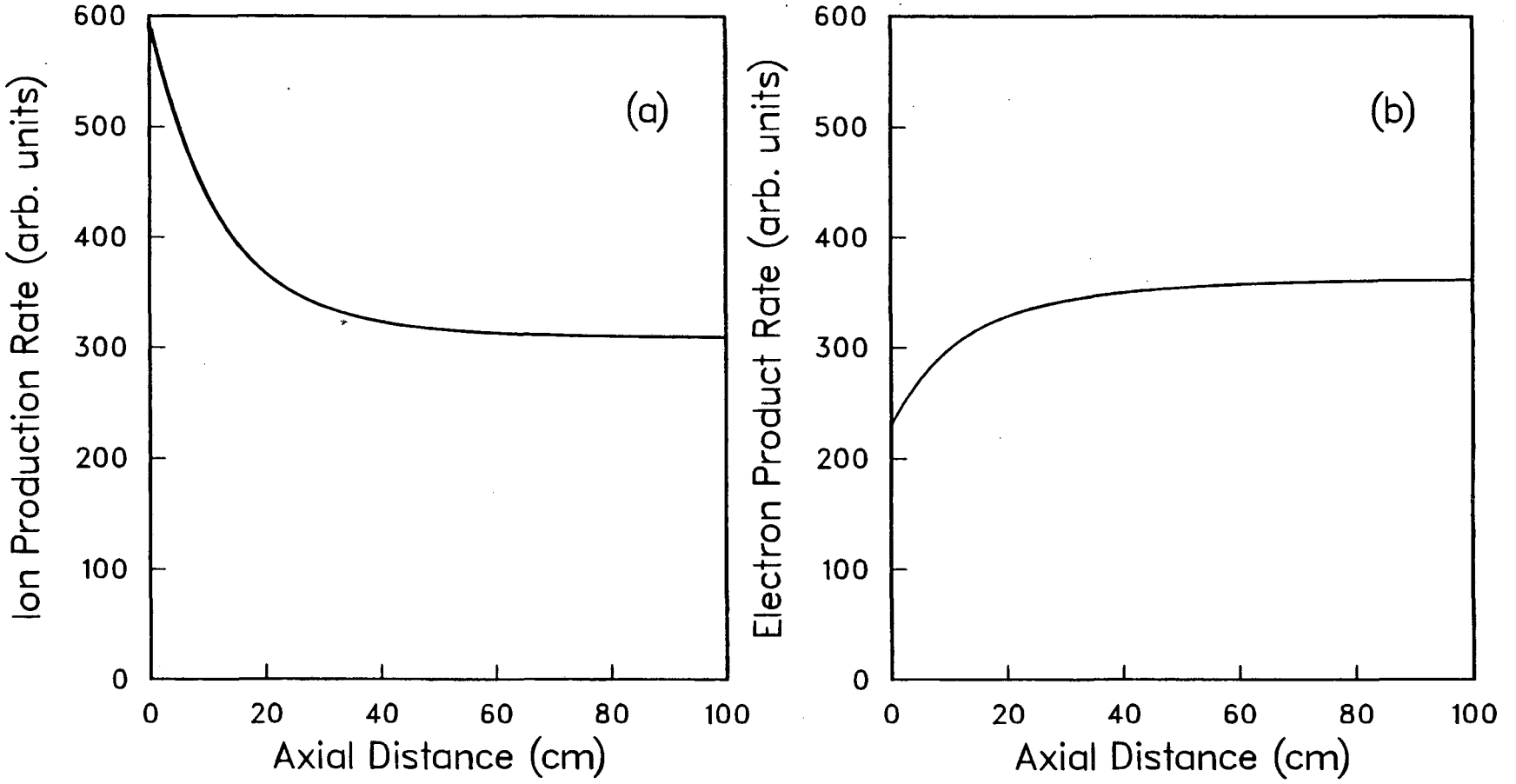

Fig. C-1 a) Axial Dependence of the Ion Production Rate. b) Axial Dependence of the Electron Production Rate. These have been calculated for an inital beam species mix of 60% H , 25% H , and 15% H ; a beam energy of 25 kV; and a gas pressure of 2.8 mTorr at Z = 30 cm.

With quasineutrality and Eq. C4,

$$\frac{n_e(z)}{n_e(z_o)} = \frac{n_g(z) \sum_s I_s(z)\, \sigma_s^{ion}}{n_g(z_o) \sum_s I_s(z_o)\, \sigma_\sigma^{ion}} \tag{C5}$$

Employing the Boltzmann relation for n_e, we find

$$\phi(z) = \phi(z_o) + T_e \cdot \ln \left\{ \frac{n_g(z) \sum_s I_s(z)\, \sigma_s^{ion}}{n_g(z_o) \sum_s I_s(z_o)\, \sigma_s^{ion}} \right\} \tag{C6}$$

A convenient choice is $z_o = 0$. We actually make measurements at z=30 cm, but we can use Eq. C6 to relate those to z=0. The I_s's in Eq. C6 are automatically functions of Π, but $n_g(z)$ needs to be related to Π. We assume

$$n_g(z) = n_g(z=0) \cdot (1 - \frac{z}{L}). \tag{C7}$$

Then, where $n_{go} = n_g(z=0)$

$$\Pi = \int_0^z n_g dz' = n_{go}(z - \frac{z^2}{2L}) .$$

Or $(z-L)^2 = L^2 - 2\Pi L/n_{go}$. (C8)

Then, with Eq. C7,

$$n_g(\Pi) = n_{go} \sqrt{1 - \frac{2\Pi}{n_{go} L}} \tag{C9}$$

Thus Eq. C6 can be expressed as

$$\phi(\Pi) = \phi(\Pi=0) + T_e \ln \left\{ \sqrt{1 - \frac{2\Pi}{L n_{go}}} \cdot \frac{\sum_s I_s(\Pi)\, \sigma_s^{ion}}{\sum_s I_s(0)\, \sigma_s^{ion}} \right\} \tag{C10}$$

We use this in Eq. C3. The integration begins after the input of $\phi(0) = \phi(z_o)$, T_e and n_{go}. The axial evolution of each of the 14 integrals in the sum of Eq. C3 is shown in Fig. C-2. Eq. C8 has been

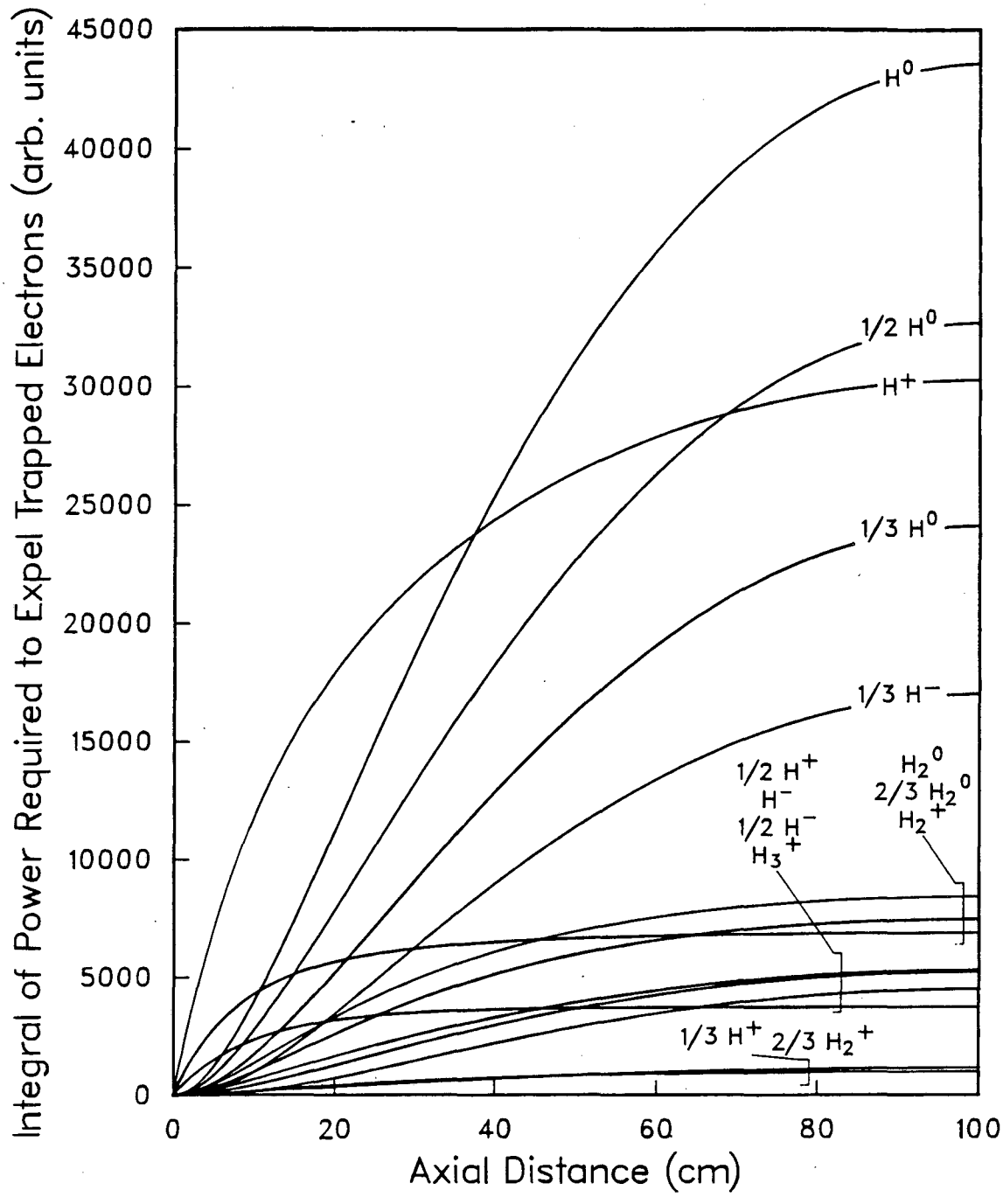

Fig. C-2 Integral For the Power Required to Expel Electrons Trapped in the Potential Well. The axial evolution of the fourteen integral terms is shown. These have been calculated for an initial beam species mix of 60% H^+, 25% H_2^+, and 15% H_3^+ ; E_b = 25 kV; and a gas pressure of 2.8 mTorr at z=30 cm. The fractions in the curve labels refer to the energy of that species relative to E_b.

used to transform back to z. Note that the 3 terms that initially grow the fastest are the original beam components, while the terms of the resultant species (H^0, H^-, etc.) grow at a higher rate farther down the neutralizer, where their densities are higher.

2. Inelastic Losses

Again, we assume axial uniformity of the beam shape, and thus in the variation of n_e in a plane perpendicular to the beam direction. In other words, the x-y (or radial, depending on geometry) profile of n_e is independent of z. Therefore, $n_e(x,y,z)$ is factorable into $X(x,y) \cdot n_e(z)$, where $n_e(z)$ is understood to mean $n_e(r=0,z)$. Note that X is a quantity we have to measure and that it can be measured at any z. In our case, we have approximate cylindrical symmetry and use

$$X(r) = \frac{n_e(r,z_1)}{n_e(r=0,z_1)} \qquad (C11)$$

Then the integral over dx and dy in Eq. 2.5 becomes a radial integral, which we define as SHAPE,

$$\text{SHAPE} = \frac{1}{A_p} \int_0^{a_w} 2\pi r \, \frac{n_e(r,z_1)}{n_e(r=0,z_1)} \qquad (C12)$$

where a_w is the wall radius. For our radial profiles SHAPE is usually 0.5. So Eq. 2.5 becomes

$$P_{inel} = \Gamma(T_e) \cdot \text{SHAPE} \cdot A_p \cdot \int_0^L n_e(r=0,z) n_g(z) dz \, .$$

With Eq. C5 and C1, the integral over z is transformed into an integral over Π;

$$I_z = \frac{n_e(z_o)}{n_g(z_o)\ \Sigma_s\ I_s(z_o)\ \sigma_s^{ion}} \int_0^{\Pi_L} n_g(\Pi)\ \Sigma_s\ I_s(\Pi)\ \sigma_s^{ion}\ d\Pi \ .$$

Using Eq. C9,

$$P_{inel} = \frac{\Gamma(T_e) \cdot SHAPE \cdot A_p \cdot n_{go}}{n_g(z_o)\ \Sigma_s\ I_s(z_o)\sigma_s^{ion}}\ n_e \cdot$$

$$\int_0^{\Pi_L} \sqrt{1 - \frac{2\Pi}{n_{go}L}}\ \Sigma_s\ I_s(\Pi)\ \sigma_s^{ion}\ d\Pi \ . \qquad (C13)$$

P_{inel} is shown in Fig. C-3, plotted as the integral accumulates versus z.

3. Kinetic Energy That Electrons Transport Out

The integral over ε in Eq. 2.6 is

$$\int_0^{\Phi_p} f(\varepsilon)d\varepsilon = 1 - e^{-\Phi_p/E_n} \ .$$

The x-y integration of Eq. 2.6,

$$I_{x-y} = \int_{A_b} \Sigma_s\ n_s\ v_s\ dxdy,$$

is just the particle currents

$$I_{x-y} = \Sigma_s\ I_s \ .$$

Then

$$P_{K.E.} = T_e \int_0^L \Sigma_s\ I_s\ \sigma_s^e\ n_g(1 - e^{-\Phi_p/E_n})\ dz$$

$$= T_e \int_0^{\Pi_L} \Sigma_s\ I_s(\Pi)\ \sigma_s^e\ (1 - e^{-\phi(\Pi)/E_n})\ d\Pi \qquad (C14)$$

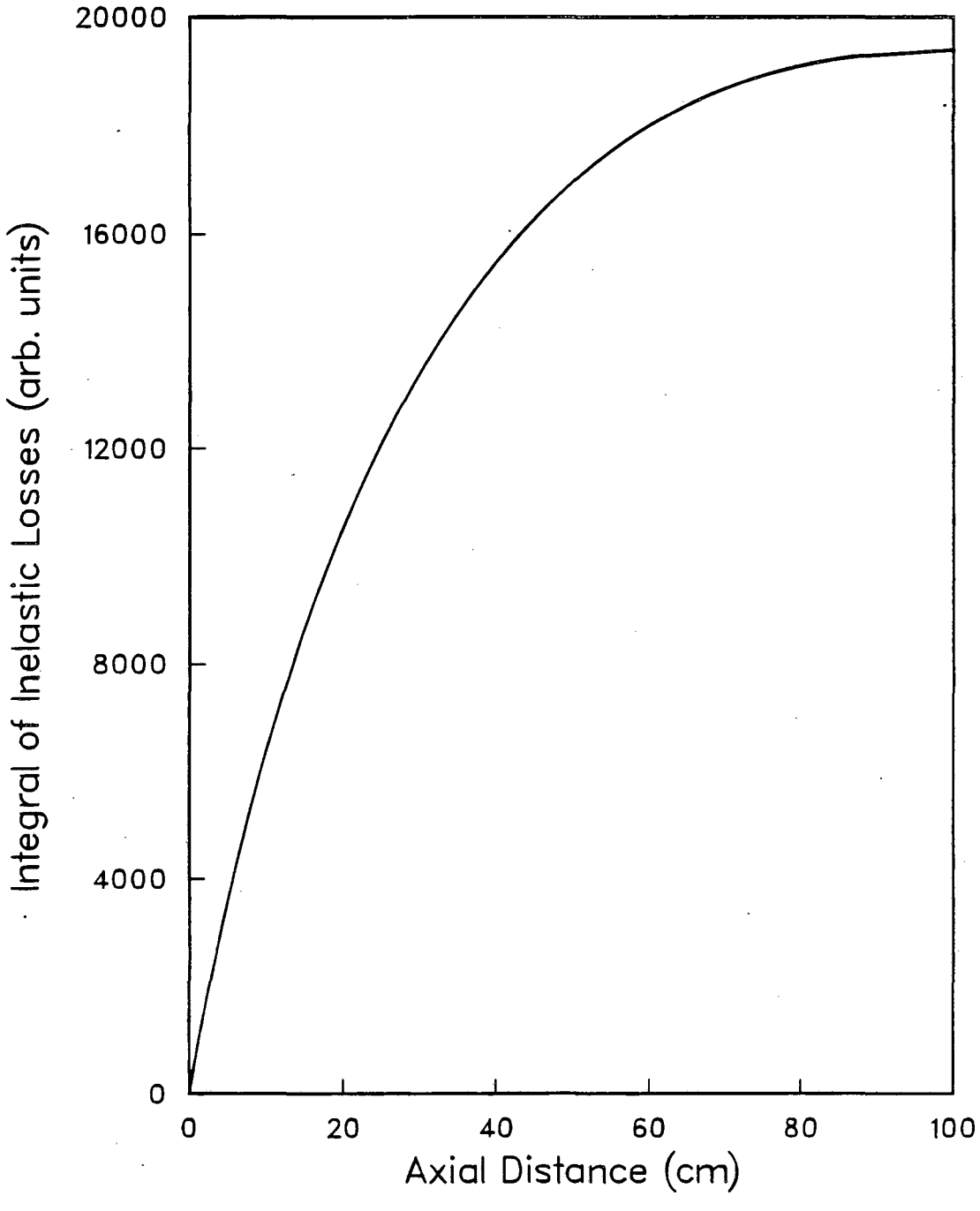

Fig. C-3 Axial Evolution of the Integral of Electron Power Loss to the Neutral Gas by Inelastic Collisions. Calculated for an initial beam species mix of 60% H^+, 25% H_2^+, and 15% H_3^+ ; E_b = 25 kV; and a gas pressure of 2.8 mTorr at z=30 cm.

$P_{K.E.}$ is shown as it accumulates versus z in Fig. C-4, and $\sum_s I_s(z)\ \sigma_s^e$ is plotted in Fig. C-1b.

4. Coulomb Collisions

Again, we factor $n_e(x,y,z) = X(x,y) \cdot n_e$. We also factor $n_s(x,y,z) = B(x,y)\ n_s(z)$, where $n_s(z)$ is understood to be $n_s(r=0,z)$. Then the x-y integral in Eq. 2.9 becomes

$$I_{shape} = \int_{A_b} X(x,y)\ B(c,y)\ dxdy \quad .$$

In our cylindrical geometry,

$$I_{shape} = 2\pi \int_0^{a_b} B(r)\ X(r)\ rdr \quad ,$$

where $B(r) = j_b(r)/\bar{j}_b$, X(r) is defined in Eq. C11, j_b is the beam current density, and $\bar{j}_b$ is its average. Remember, the latter are measured quantities. Let us define $SHAPE_b = I_{shape}/A_b$. For our profiles $SHAPE_b$ is usually .8. Do not be alarmed that $SHAPE_b > 0.5$; this is a result of normalizing the beam flux to the average in B(r), rather than to the peak. Then Eq. 2.9 can be expressed as

$$P_{Coul} = \frac{4\pi e^4 \ell n\ \lambda}{m_e}\ SHAPE_b \sum_s \frac{q_s^2}{v_s^2} \int_0^L n_s\ v_s A_b\ n_e(z)\ dz \qquad (C14)$$

The first three factors in the integral over dz are recognizable as I_s. Using Eq. C5 for $n_e(z)$ and converting to dΠ,

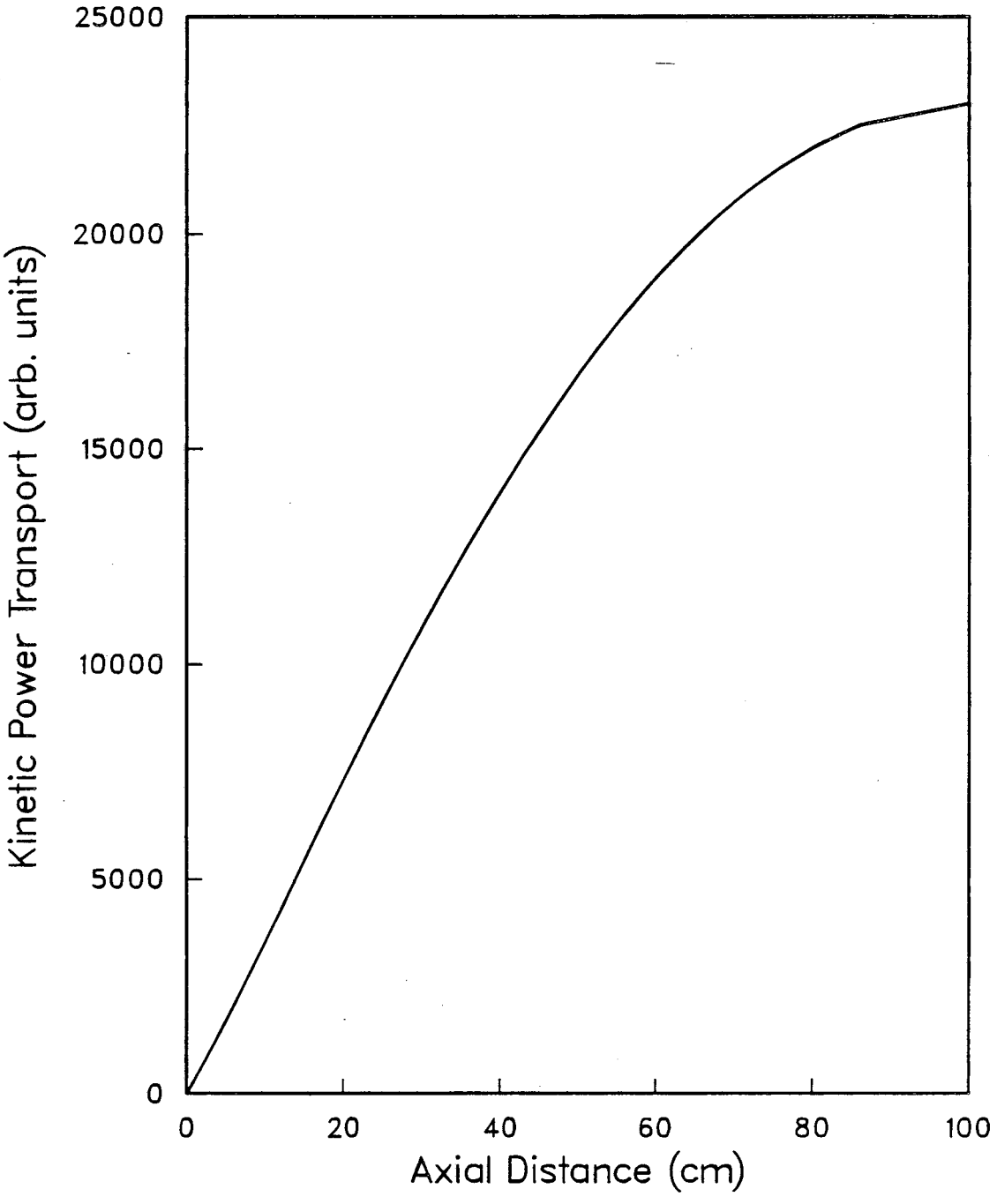

Fig. C-4 Axial Evolution of the Kinetic Power Transported to the Wall by Electrons Escaping From the Potential Well. Calculated for an initial beam species mix of 60% H^+, 25% H_2^+, and 15% H_3^+ ; E_b = 25 kV; and a gas pressure of 2.8 mTorr at z=30 cm.

$$P_{Coul} = \frac{4\pi e^4 \ell n \lambda \, n_e(z_o)}{m_e \, n_g(z_o) \sum_{s''} I_{s''}(z_o)\sigma_{s''}^{ion}} \; SHAPE_b$$

$$\cdot \sum_s \frac{q_s^s}{v_s^2} \int_0^{\Pi_L} I_s(\Pi) \sum_{s'} I_{s'}(\Pi) \, \sigma_{s'}^{ion} \, d\Pi \qquad (C16)$$

Each of the 14 integrals in the s summation is shown in Fig. C-5, plotted as they accumulate versus z. Notice that the neutral terms do not contribute to the power balance, as we have shown in Appendix A.

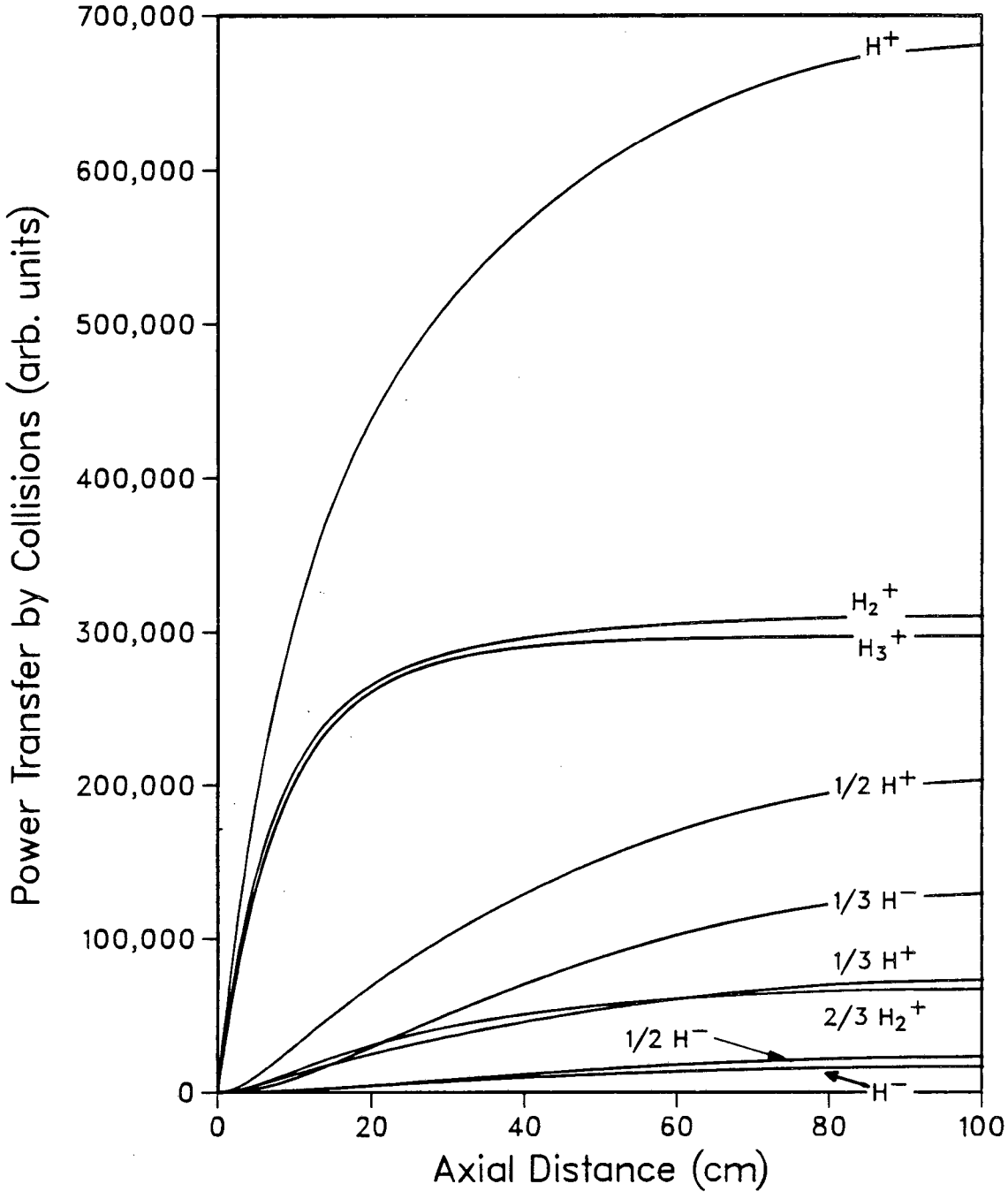

Fig. C-5 Axial Evolution of the Integral of Power Transfer to Electrons From Beam Ions via Coulomb Collisions. These terms are calculated for an initial beam species mix of 60% H^+, 25% H_2^+, and 15% H_3^+ ; E_b = 25 kV; and a gas pressure of 2.8 mTorr at z=30 cm. The fractions in the curve labels refer to the energy of that species relative to E_b.

Appendix D:

The Slope of T_e (I_b)

Differentiating Eq. 2.19 we find

$$\frac{dT_e}{dI_b} = \frac{2}{3}\, g_{11}/(I_b + g_{12})^{1/3} \quad .$$

Using Eq. 2.19 this can be expressed as

$$\frac{dT_e}{dI_b} = \frac{2}{3}\sqrt{\frac{g_{11}^{\,3}}{T_e}} \quad . \tag{D1}$$

The constant g_{11} is defined in Eq. 2.19a as

$$g_{11} = (g_{10})^{2/3} \tag{2.19a}$$

Also

$$g_{10} = \frac{g_6 \sigma^{ion}}{E_b \sigma^{e}} \tag{D2}$$

and

$$g_6 = g_5/(g_1 + g_4) \quad . \tag{D3}$$

Consider Eq. 2.13 and Eq. 2.13a. For the data we are describing now, $\phi_p \approx E_n/4$, so Eq. 2.13a is no longer valid. A crude approximation would be

$$I_\varepsilon = \phi_p/4 - E_n \quad . \tag{D4}$$

We take $\phi_p \simeq 4\ T_e$ (Fig. 5-4 supports this), then

$$I_\varepsilon \simeq T_e - E_n \quad . \tag{D5}$$

Treating the spatial variables in Eq. 2.3 as uniform and using Eq.'s D5 and 2.13, when we compare Eq.'s 2.14 and 2.3 we find

$$g_1 = L \quad . \tag{D6}$$

A similar comparison of Eq. 2.16 and Eq.2.6 requires

$$g_4 = L \quad . \tag{D7}$$

Now we seek g_5. In Eq. 2.9 we treat all species as protons and use

$$v_s^2 = 2\, E_b(V) \cdot 10^{12}\ cm^2/sec \qquad (D8)$$

and convert from ergs to (e)V. Then upon comparing Eq. 2.9 with Eq. 2.17, we find

$$g_5 = \frac{4\pi\, e^4\, \ell n\lambda\ \ n_e\, \sqrt{T_e}\, L}{1.6\cdot 10^{-12}\, m_e\ \ 2\cdot 10^{12}\ \ I_b(\#/sec)\, n_g \sigma^{ion}} \qquad (D9)$$

The data in Fig. 5-4 (the same as 1.7 mT data in Fig. 5-1) is measured at r = 3 cm, z = 30 cm. The density at r=0, which is what we want in Eq. D9, is typically 2-3 times n_e(r = 3 cm). For the data in Fig. 5-4 at I_b = 4 Amps, and using $n_g = 5.6 \cdot 10^{13}/cm^3$ and $\sigma^{ion} \simeq 6\cdot 10^{-16}\ cm^2$, we find

$$g_5 = 1.6 \cdot 10^{-16}(V)^{3/2}\ sec \cdot L \qquad (D10)$$

Combining eq.'s D3, D6, D7, and D10 we find

$$g_6 = 8 \cdot 10^{-17}(V)^{3/2}\ sec\ .$$

From Fig. 2.3 we see that at E_b = 25 kV, $\sigma^{ion}/\sigma^{e} \simeq 4$.

Then (at 25 kV)

$$g_{10} = 1.3 \cdot 10^{-20}\ (V)^{3/2}\ sec\ .$$

Notice that E_b in Eq. D2 is actually unitless, assumed to be in V by the use of Eq. D8, so g_6 and g_{10} have the same units.

Using Eq. 2.19a in Eq. D1, we find

$$\frac{dT_e}{dI_b} = \frac{2}{3}\ \frac{g_{10}}{\sqrt{T_e}} \qquad (D11)$$

If we wish Eq. D11 to be of units V/Amp, we need to divide Eq. D11 by the electronic charge. With T_e = 0.7 V, we find

$$\frac{dT_e}{dI_b} = 0.06 \text{ V/Amp} . \qquad (D12)$$

We can also express g_{10} in current units:

$$g_{10} = 0.08 \text{ (V)}^{3/2}/\text{Amp}. \qquad (D13)$$

These compare favorably with the data in Fig. 5-4.

Appendix E

Plasma Ion Species

The plasma ion species have been investigated at z=30 cm with a small moveable magnetic mass spectrometer, which has been described elsewhere.[32] The electronic circuitry is shown in Fig. E-1. For a fixed beam current, we measure the plasma ion species mix at a specific radial position and three neutral pressures (.95, 1.7, 2.8 mTorr). Such a pressure scan is shown in Fig. E-2. The mass analyzer is then moved to another radial position and the experiment repeated. The results of this radial scan are shown in Fig. E-3.

We assume the neutral gas to be molecular. This is expected because dissociation by the beam is so slight. For example, we might expect this dissociation to proceed at a rate comparable to ionization. Atomic loss rates would be similar to ion loss rates as the H^o are mildly energetic (few V). We would then expect

$$n_{H^o} \sim n_i \ll n_{H_2^o} \simeq n_g \ .$$

With this in mind, the ions produced are H_2^+ and H^+ in the ratio 6:1 given by the relative production rates from beam particles incident on H_2. For $r > a_b$, no ion production occurs and H_2^+ plasma ions collide with H_2, resulting in H_3^+. Note that the total number of ions is constant. These H_3^+ can be dissociated by the thermal electrons. For our low plasma density, the mean free path is very long:

$$\lambda_{mfp}\ (H_3^+) = \frac{v_i}{n_e \langle \sigma v \rangle_{dis}} = \frac{10^6 \sqrt{\frac{2T_e}{3}}}{1.1 \cdot 10^{11}\ 5 \cdot 10^{-8}} = 200 \text{ cm} \ ,$$

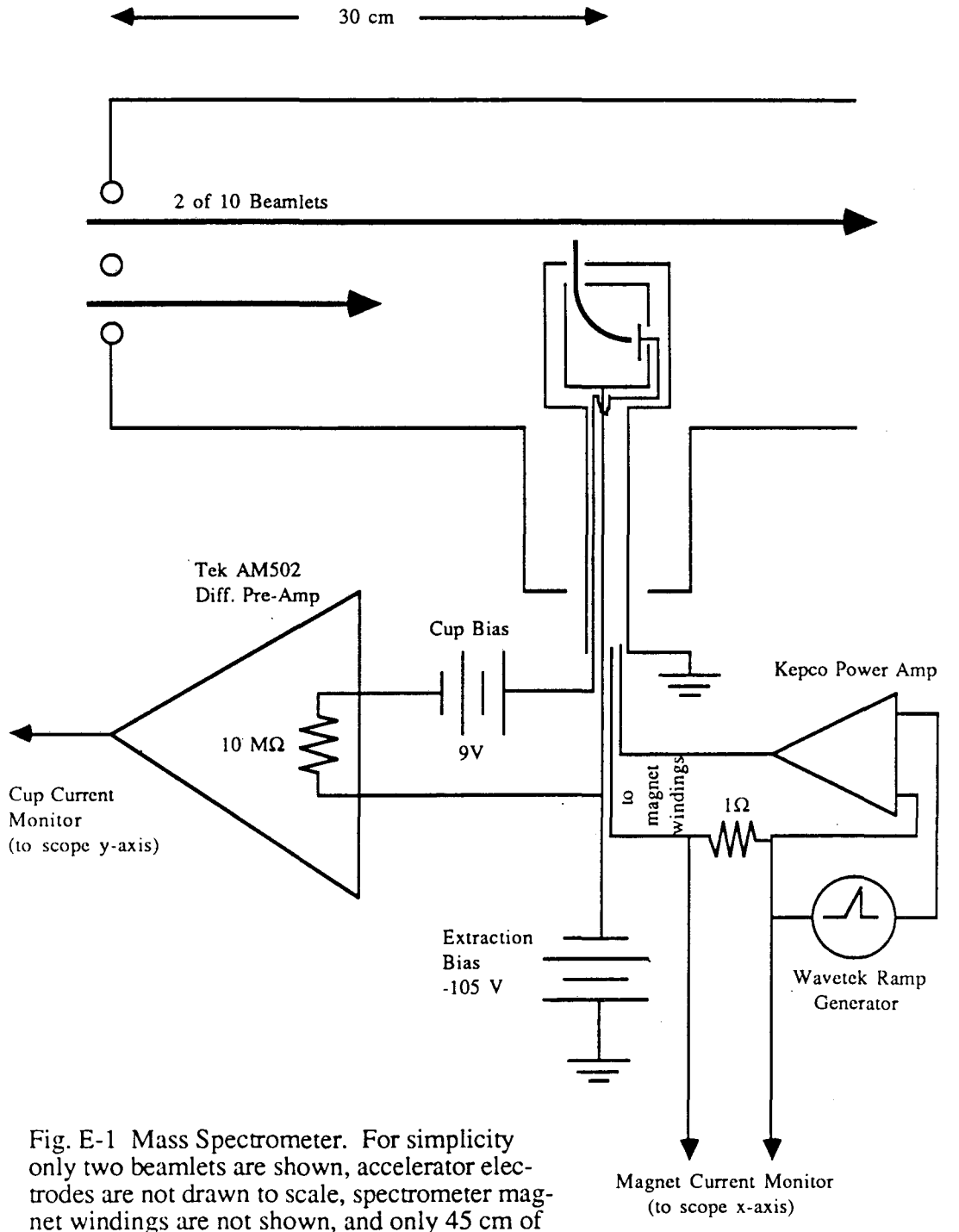

Fig. E-1 Mass Spectrometer. For simplicity only two beamlets are shown, accelerator electrodes are not drawn to scale, spectrometer magnet windings are not shown, and only 45 cm of the neutralizer are shown, beginning with the last of the three accelerator electrode assemblies.

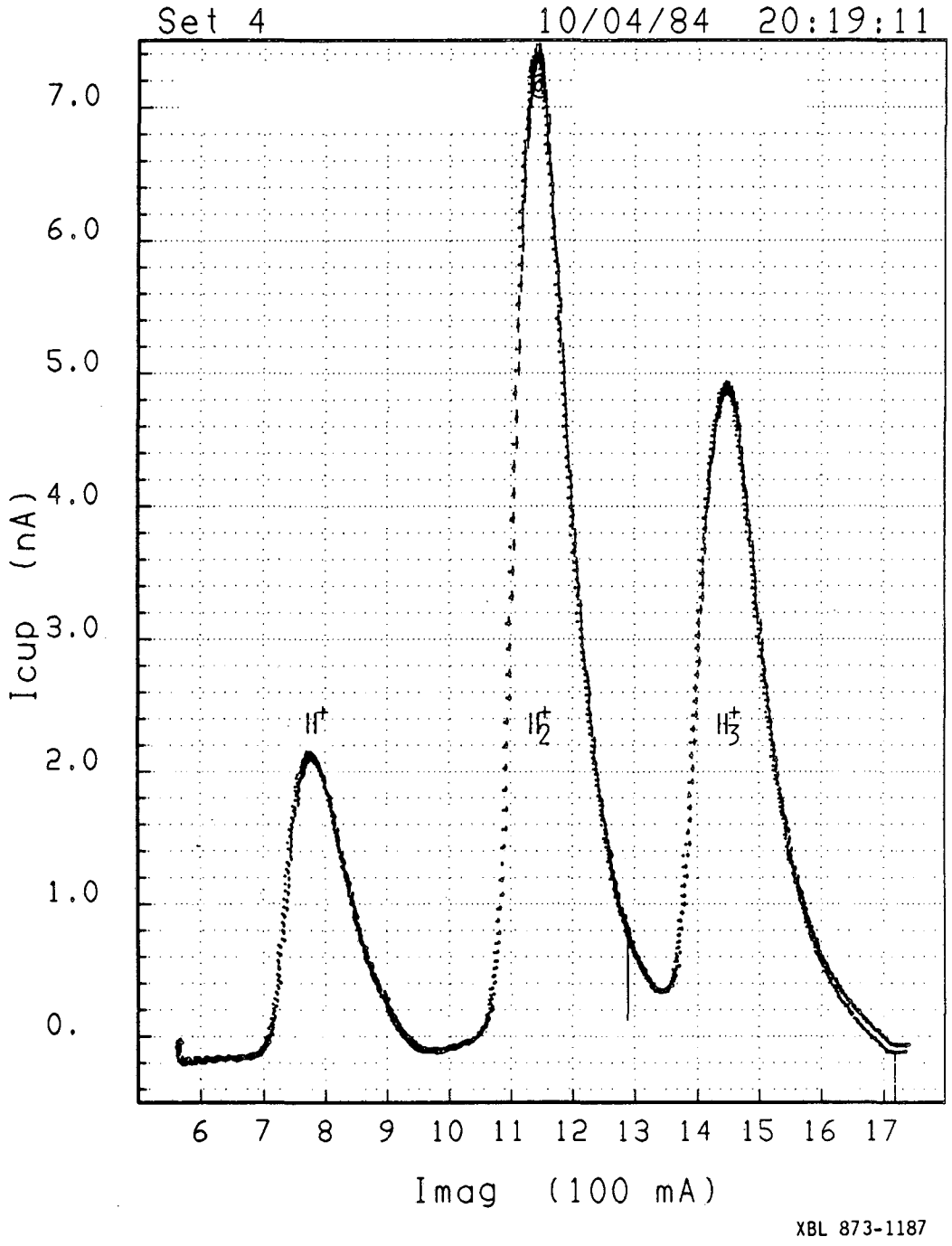

Fig. E-2 Magnetic Mass Spectrometer Data - Pressure Dependence. a) p_g = 0.95 mTorr. These three figures (a,b,and c) are the collector cup signal observed while the beam has been operated at a fixed current with the mass spectrometer fixed at one radial position.

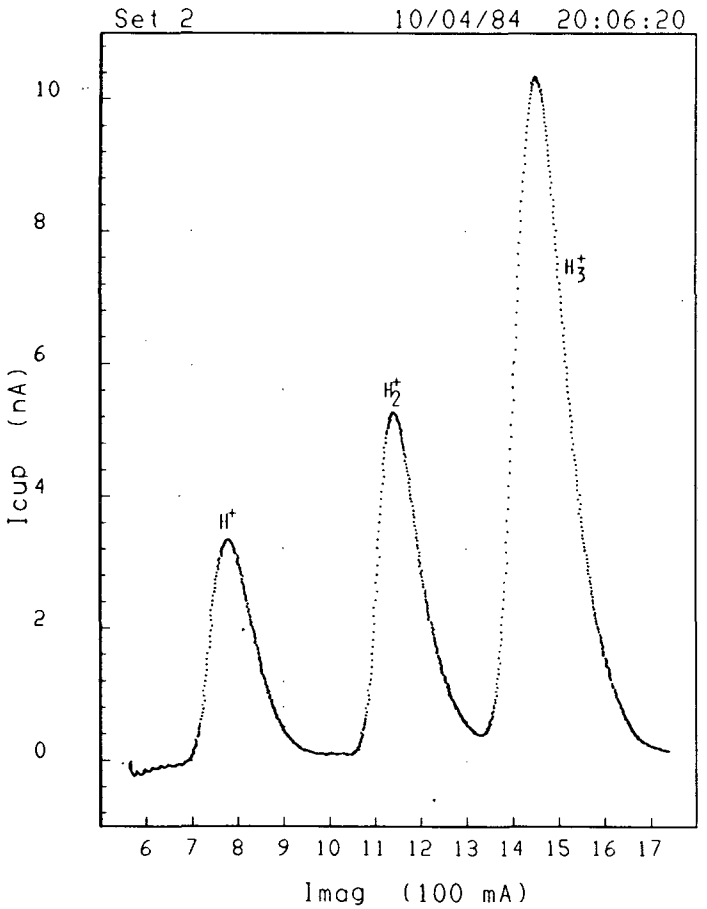

Fig. E-2 b) p_g = 1.7 mTorr.

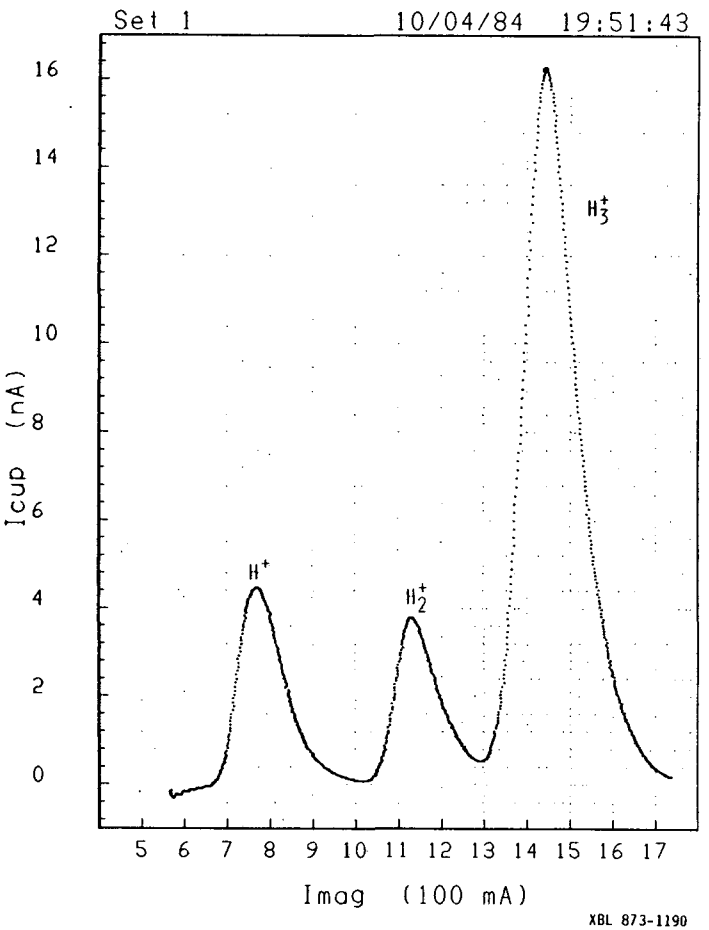

Fig. E-2 c) p_g = 2.8 mTorr.

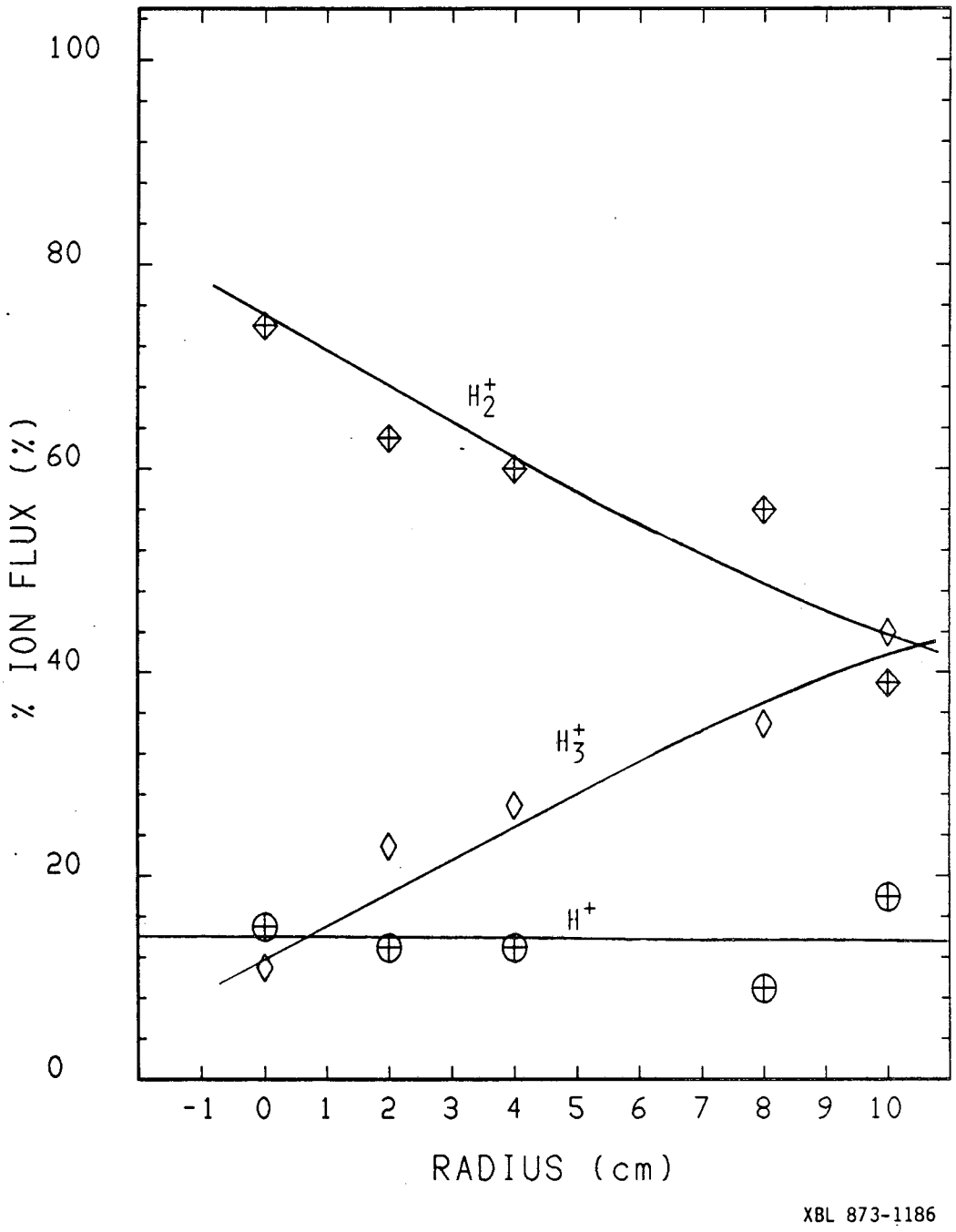

Fig. E-3 Radial Evolution of the Plasma Ion Species - Pressure Dependence. a) p_g = 0.95 mTorr. The percent contribution to the total ion flux (as determined from the collector cup current) of each of the three ion species is plotted versus the mass spectrometer's radial position. The lines drawn are least square fits of the data to the model given in the text.

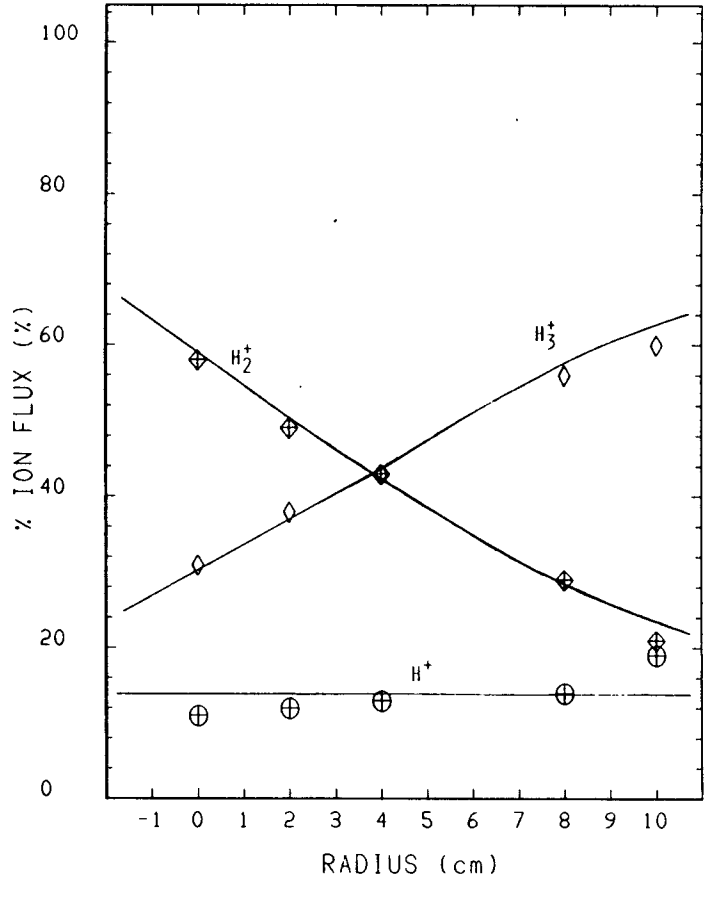

Fig. E- 3 b) p_g = 1.7 mTorr.

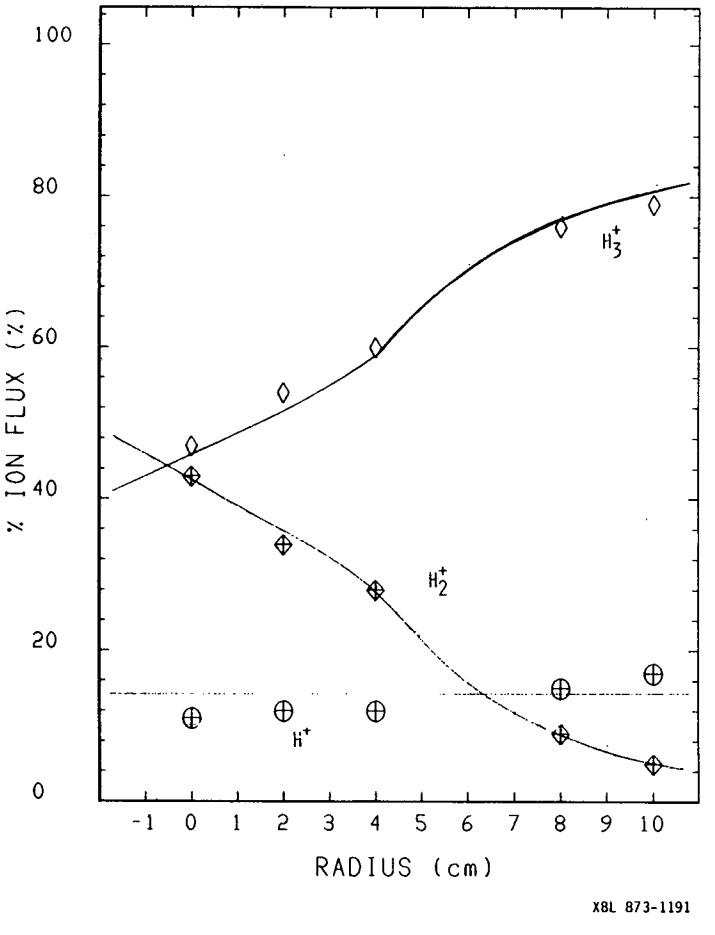

Fig. E- 3 c) p_g = 2.8 mTorr.

where we have utilized our standard parameters and have used a rate from C.F. Chan[4]. As $\lambda_{mFp}(H_3^+) >> a_w$, we find the conversion of H_2^+ to H_3^+ to be unimpeded. For $r > a_b$, then, the fraction of unconverted H_2^+ ions is,

$$F \equiv \frac{I(H_2^+)}{I(H_2^+) + I(H_3^+)}$$

$$= F(a_b)\, e^{-n_g \sigma_{3+} r} \qquad (E1)$$

where σ_{3+} is the cross section for the reaction $H_2^+ + H_2 \rightarrow H_3^+ + H^o$.

H_2^+ and H_3^+ ion fluxes inferred from least-square fits to the above are drawn for $r \geq 4$ cm in Fig. E-3. One of the fit parameters is $n_g \sigma_{3+}$. For energies of 0.5 to 2 V, reported σ_3's[33,34] show a decreasing exponential dependence with H_2^+ energy, $\sigma_{3+}(E) \simeq \sigma_{3+}(o) \cdot e^{-E/\varepsilon_{ch}}$. Plasma ions outside the beam have fallen across a potential drop of order T_e, so we take T_e as the ion energy, which is different for each pressure, at I_b used for this experiment. Our data are best represented by the characteristic energy exhibited by the data of Barnett,[33] $\varepsilon_{ch} = 1.18$V, for which, $\sigma_{3+}(o) = 3 \cdot 10^{-15}$ cm^2. The exponential fit parameters (apparent target thickness) have been divided by $e^{-T_e/1.18\ V}$ and plotted in Fig. E-4a. If our data demonstrated this same energy dependence, this rescaling would place all the points on a line, the slope then being $\sigma_{3+}(o)$. The slope of this line when mTorr are converted to particles/cm^3 is found to be $5.5 \pm .1 \cdot 10^{-15}$cm^2. This is almost twice

a)

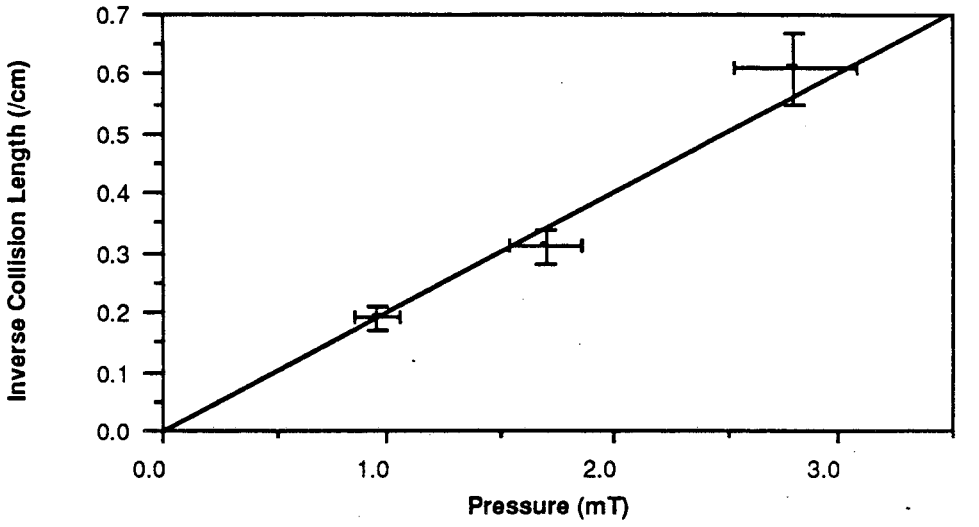

b)

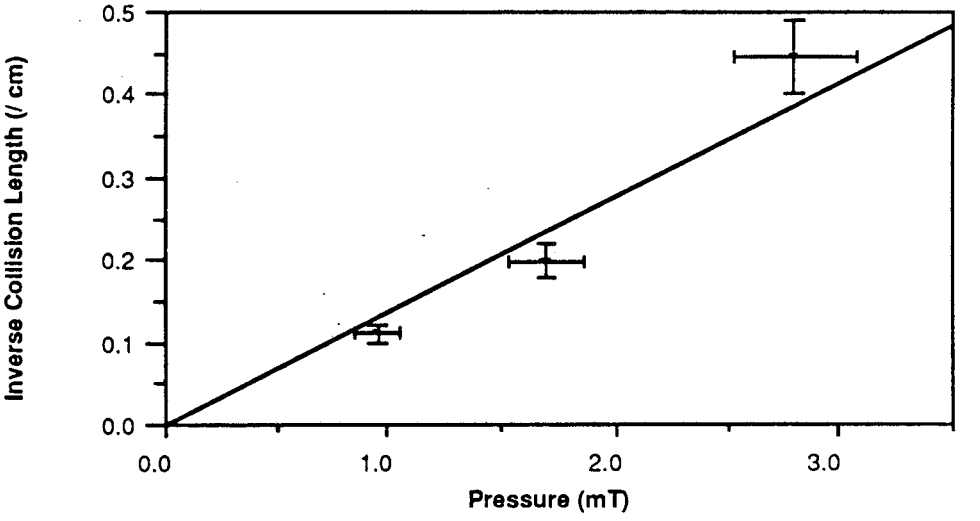

Fig. E-4 Inverse Mean Free Path for Molecular Rearrangement Collisions. Fit parameters from the data in Fig. E-3 are plotted after being rescaled for the appropriate electron temperatures in order to be representative of the ion speed.
a) Rescaled to the characteristic energy of the Barnett data.
b) Rescaled to the characteristic energy of the Giese data.

the value of the cross sections reported by Barnett,[33] though this rescaling choice gives the best linearity. We have also rescaled our data to the energy dependence of the cross sectional data of Giese and Maier,[34] represented by $\varepsilon_{ch} = 2$ V and $\sigma_{3+}(o) = 3.4 \cdot 10^{-15}$ cm^2. This rescaled data (plotted in Fig. E-4b) deviates more from linearity, but $\sigma_{3+}(o)$ determined from the slope, ($\sigma_{3+}(0)$ = slope = $3.9 \pm 1 \cdot 10^{-15}$ cm^2) agrees well with the value of $\sigma_{3+}(0)$ representative of the cross sections reported by Giese and Maier. Our data would then be consistent with the energy dependence ($\varepsilon_{ch} = 1.18$ V) representative of of Barnett's data[33] and the magnitude of the cross sections reported by Giese and Maier.[34] Within the uncertainties of the reported σ_3's, we feel Eq. E1 adequately describes the evolution of H_2^+ as it travels to the wall.

Notice from Fig. E-3, where I_{H^+} represents the plasma H^+ flux, that

$$\frac{I_{H^+}}{I_{H^+} + I_{H_2^+} + I_{H_3^+}} \simeq 14 \pm 3\%$$

which compares favorably with the ratio of production rates already quoted (14%). If there were any significant percentage of H^o in the neutralizer, this rate would be higher by that amount.

We conclude then that the neutralizer is predominately H_2, with atomic density < 3% of molecular density, where this latter percentage is the difference between the upper limit of H^+ percentage measured and that predicted by production rates for an H_2 target. This confirms our original expectation,

$$n_{H^o} \ll n_{H_2^o} .$$

Appendix F

Spectral Width of the Beam-Plasma Resonance

We derive here the spectral width of the temporal growth rate. The dielectric function is given by Eq. 3.1. The wave dispersion is given by Eq. 3.4, satisfying $\epsilon_p = 0$. The temporal growth rate is then found from

$$\delta\omega \cdot \left.\frac{\partial \epsilon_p}{\partial \omega}\right|_{\omega_o + \Delta\omega} + \epsilon_b(\omega_o + \Delta\omega + \delta\omega) = 0 \qquad (F1)$$

where $\Delta\omega$ is the shift away from the resonant frequency $\omega_o = \underset{\sim}{k} \cdot \underset{\sim}{v}_b$.

For

$$\epsilon_p = 1 - \frac{\omega_e^2}{\omega^2 - 3k^2 v_e^2} ,$$

We find

$$\left.\frac{\partial \epsilon_p}{\partial \omega}\right|_{\omega_o + \Delta\omega} \simeq -\frac{2}{\omega_e}$$

and Eq. 3.3 gives

$$\epsilon_p\,(\omega_o + \Delta\omega + \delta\omega) = \frac{\omega_b^2}{(\delta\omega + \Delta\omega)^2}$$

Then Eq. F1 becomes

$$\delta\omega^3 + 2\Delta\omega \cdot \delta\omega^2 + \Delta\omega^2 \cdot \delta\omega + \frac{R}{2}\,\omega_e^3 = 0.$$

The imaginary part of the growing root of this cubic equation is plotted versus $\Delta\omega/\omega_e$ in Fig. F-1. We see that when the frequency has shifted 5% above ω_o ($\omega_o \simeq \omega_e$), growth stops. This would be the situation that occurs when a wave, resonant at one z position, propogates to a region of 10% lower density, where the resonant frequency is now 5% lower.

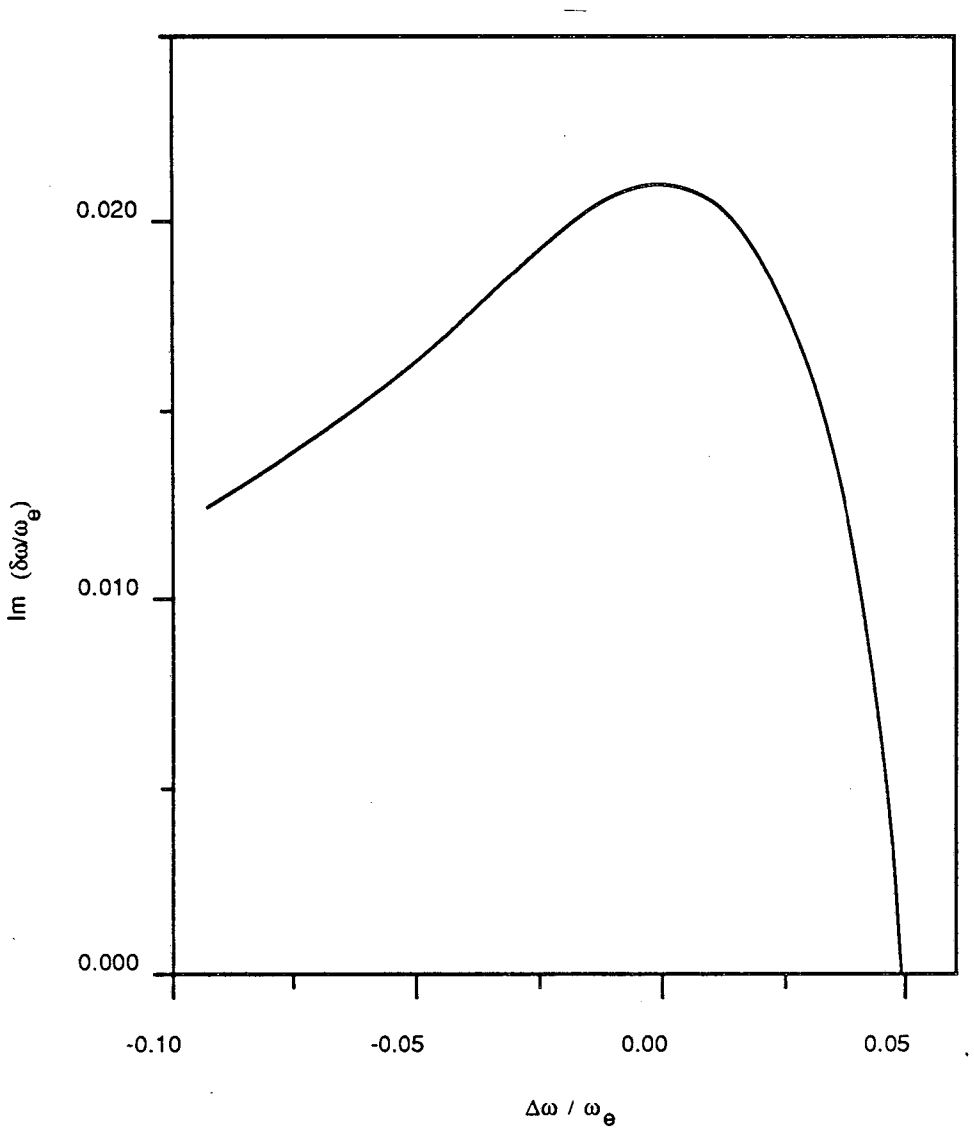

Fig. F-1 Width of the Resonant Instability. The resonant growth rate is shown plotted as a function of the shift away from the resonant frequency. Note that for a wave frequncy 5% above the resonant frequency (very nearly the plasma frequency) , resonant wave growth stops.

References

1. Abt. N. E., University of Calif., Ph.D. Thesis, LBL-13935 (1982).
2. Gabovich, M. D., Katsubo, L. P., and Soloshenko, I. A., Sov. J. Pl. Phys. 1, #2, 162 (1975).
3. Holmes, A. J. T., Phys. Rev. A 19, 387 (1979).
4. Chan, C. F., Lawrence Berkeley Lab. report, LBID 632 (1983).
5. Barnett, C. F., et al., Atomic Data for Controlled Fusion Research, Vol. I, Oak Ridge National Laboratory, ORNL-5206, pg. A.5.9.
6. Rudd, M. E., Phys. Rev. A 20 #3, 787 (1979).
7. Barnet, Op. Cit., Vol. II, pg. C.1.4. and McDaniel, E. W., Collision Phenomenon in Ionized Gases, Wiley New York (1964), pg. 122, using twice σ for H^0.
8. Chen, F. E., Introduction to Plasma Physics, Plenum, New York (1984), pg. 322.
9. Book, D. L., NRL Plasma Formulary, Naval Research Laboratory, Wash. D.C. (1983), pg. 32.
10. Pastukhov, V. P., Nuclear Fusion, 14, #3 (1974).
11. Hasegawa, A., Plasma Instabilities and Nonlinear Effects, Springer-Verlag, New York (1975), pg. 163.
12. Schmidt, G., Physics of High Temperature Plasmas, Academic Press, New York (1979), pg. 209.
13. Mikhailovshi, A. B., Theory of Plasma Instabilities, Vol. 1, Consultants Bureau, New York (1974), Chapter 3.

14. Cooper, W. S., Lawrence Berkeley Laboratory, Private Communication and Wekhof, A., Smith, R. R., and Medley, S. S., Nucl. Technol./ Fus. (USA), 3, #3, 462 (1983).

15. Dunn, D. A., and Self, S. A., J. of Appl. Phys. 35, 113 (1964).

16. Kino, G. S., and Shaw, E. K., Physics of Fluids, 9, 587 (1966).

17. Berkner, K. H., Pyle, R. V., and Stearns, J. W., Nuclear Fusion 15, 249 (1975).

18. Gilev, E. A., Davydenko, V. I., Rosliakov, G. V., Sokolov, V. G., and Timoshin, I., Nuclear Physics Institute of Siberian Division of Academy of Science of USSR, Novosibirsk, Preprint 85-62 (1985), Russian.

19. Schoenberg, K. F., University of Calif., Ph.D. Thesis, LBL-8940 (1979).

20. Ehlers, K. W., et al., J. Vac. Sci. Tech. 10, #6, 922 (1973).

21. Langmuir, I. and Mott-Smith, H. M., Gen. Elec. Rev. 27, 449 (1924). Goodall, C. V. and Polychronopulos, B., Planet. Space Sci. 22, 1585 (1974).

22. Pastukhov, loc. cit.

23. Chen, Op. cit., pg. 248.

24. Cooper, W. S., Halbach, K., and Magyary, S. B., Proceedings of the Second Symposium on Ion Sources and Formation of Ion Beams, Berkeley, Calif., Oct. 1974, II-1-1, LBL-3399, (1974).

25. Schoenberg, K. F., Los Alamos National Laboratory, Private Communication.

26. McDaniel, Op. Cit., Chapter 1.

27. Ibid., pg. 132.

28. Marion, J. B., Classical Dynamics of Particles and Systems, Academic Press, New York (1970), pg. 308.

29. Ibid., pg. 300.

30. Chandrasekhar, S., Principles of Stellar Dynamics, Univ. of Chicago Press, Chicago (1942), Chapter 2, sec. 5.6.; Chandrasekhar, S., Astrophys. J., 97, 255 (1943).

31. Stearns, J. W., Berkner, K. H., and Pyle, R. V., Proc. of the 2nd Topical Meeting on The Technology of Controlled Nuclear Fusion, Vol. IV, Sept. 1976, Richland, Washington, pg. 1221, CONF-760935-P4 (1976).

32. Leung, K. N., Guethlein, G., and Walther, S., Rev. Sci. Inst., 56, #7, 1480 (1985).

33. Barnett, Op. Cit., A.9.2.

34. Giese and Maier, J. Chem. Phys. 39, 739 (1963).

This report was done with support from the Department of Energy. Any conclusions or opinions expressed in this report represent solely those of the author(s) and not necessarily those of The Regents of the University of California, the Lawrence Berkeley Laboratory or the Department of Energy.

Reference to a company or product name does not imply approval or recommendation of the product by the University of California or the U.S. Department of Energy to the exclusion of others that may be suitable.

LAWRENCE BERKELEY LABORATORY
TECHNICAL INFORMATION DEPARTMENT
UNIVERSITY OF CALIFORNIA
BERKELEY, CALIFORNIA 94720

AAW445
LBL Libraries